



**UiT** The Arctic University of Norway

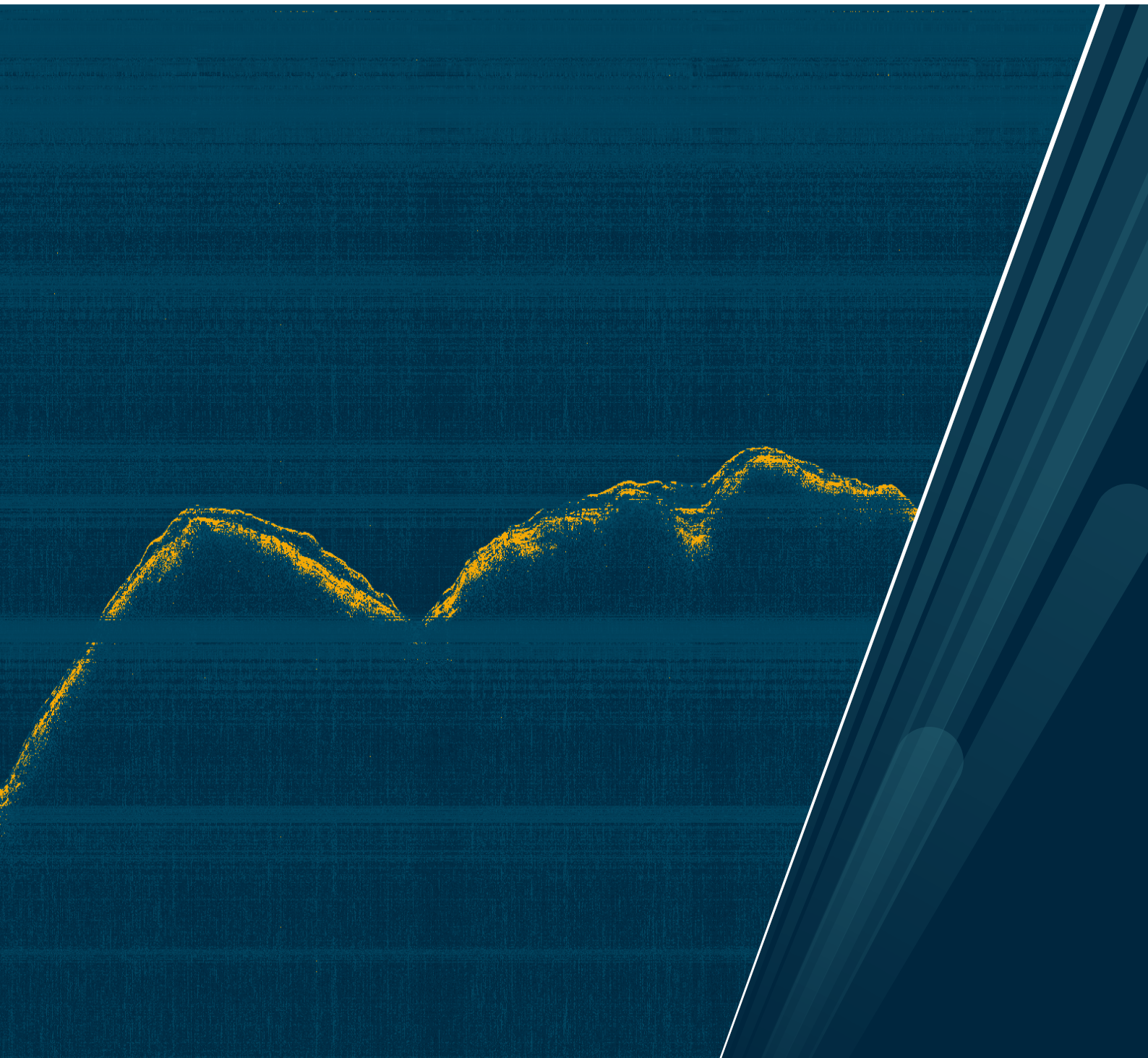
Faculty of Science and Technology  
Department of Physics and Technology

## **Radar System Development for Drone Borne Applications with Focus on Snowpack Parameters**

Rolf Ole Rydeng Jensen

A dissertation of the degree of Philosophiae Doctor

January 2021





Front-page image: Fourier domain filtered radar image showing cross-talk and ringing (horizontal lines), and narrow-band radio-frequency clutter (vertical lines). The detected snowpack is coloured orange showing snow depth and the varying altitude of the drone combined with topography.



# Abstract

A complete representation of the Arctic cryosphere has historically been restricted by its remoteness, large extent, and restrictions in measurement methods and equipment. Here, remote sensing of snow-cover is a central method to improve the current knowledge of the Earth's ecosystem, and hence a critical component in cryospheric models.

The use of drone-borne radar systems has seen considerable advances over recent years, allowing for the application of drone-mounted remote sensing of snow properties.

This thesis describes the development of an ultra-wideband radar system for drone-mounted snow measurements. From the initial testing and technical implementation to field trials and method development for more advanced radar data analysis.

This involves the development of lightweight and high-bandwidth radar systems intending to understand the limitations of design parameters for drone-borne radar systems and how these parameters influence the ability to measure snow conditions. Such understanding includes antenna theory and ultra wide-band radar theory, where most choices involve compromises. Snow as an electromagnetic propagation medium is presented with a focus on the previous design solutions. In that respect, various methods to measure snow parameters are discussed. Furthermore, this thesis aims to describe the iterative process of a drone-borne radar system development and how experiences from field trials are central to further improvements.



# Acknowledgments

First and foremost, I would like to express my sincere gratitude to my supervisor, *Prof. Svein K. Jacobsen*. Your lectures in microwave engineering during my master's studies sparked my interest in the field, which, eventually, led to me pursuing a career in science. Additionally, you connected me with the research institute Norut (now called NORCE), resulting in a part-time job as an engineer at the drone-group during my master studies. This experience proved to be essential in my further research. Your skill in the field and never-ending inventiveness is still surprising, even after almost six years of collaboration. Your contributions to this project are what made it possible, and our partnership has been stellar. Finally, I would like to thank you for your exceptional effort in proof-reading this thesis.

Thanks to my co-supervisor, *Dr. Rune Storvold*, for essential help with facilitating field campaigns and putting me into contact with other relevant researchers and institutes. And, my co-supervisor, *Prof. Torbjørn Eltoft* for arranging the special curriculum in SAR processing. I would also like to acknowledge the CIRFA center leader Torbjørn Eltoft and my work package leader Rune Storvold, for financing this project.

Thanks to CIRFA, who funded this research, and everyone at the CIRFA office for excellent excursions, seminars, and conferences.

Thanks to everyone at NORCE for providing an excellent work environment. A special thanks to the "Drones and autonomous systems" group for help with all kinds of technical implementations or as pilots during fieldwork. In that regard, I must extend an extra thanks to Tore Riise and André Kjellstrup. They have piloted the drones during the various field campaigns. Many of these campaigns would be complete failures without their and solution-oriented work style. These campaigns have granted me priceless field experience.

I would also like to thank *Dr. Markus Eckerstorfer* for your help introducing me to the field of snow science early in this project and for central help with the writing of my first paper and conference proceedings. Together with *Dr. Hanna Wickers*, you have collected almost all the *in situ* data for this thesis.

Thanks to *Dr.* Eirik Malnes for continued support and inclusion in research projects.

I want to thank Karl Magnus Fossan and Bernt Inge Hansen for inspiring and enthusiastic lectures and talks about electronics during my bachelor's studies.

I want to acknowledge the Nansen centre for letting me tag along on the CAA-TEX expedition to the North Pole and to SIOS for funding the field campaigns on Svalbard.

To my friends, bands, family, thank you for supporting me through these years in different ways. A special thanks to Sigurd Eivindson Løkse for proofreading this thesis.

Finally, I owe my deepest gratitude to my girlfriend and best friend, *MD* Ina Lundberg. Thank you for your love, patience, and support throughout this project.



# Contents

<b>Abstract</b>	<b>iii</b>
<b>Acknowledgments</b>	<b>v</b>
<b>List of Figures</b>	<b>xi</b>
<b>List of Tables</b>	<b>xiii</b>
<b>List of Abbreviations</b>	<b>xv</b>
<b>Selected Symbols</b>	<b>xix</b>
<b>1 Introduction</b>	<b>1</b>
1.1 Thesis Outline . . . . .	3
<b>2 Previous Work</b>	<b>7</b>
2.1 Ground Penetrating Radar on Snow . . . . .	7
2.2 Airborne GPR . . . . .	8
2.3 Snow parameter estimation methods . . . . .	9
<b>3 Ground Penetrating Radar Theory</b>	<b>11</b>
3.1 Operating Principle . . . . .	12
3.1.1 The Radar Equation . . . . .	14
3.1.2 Resolution of UWB Signals . . . . .	16
3.1.3 Scattering Mechanisms . . . . .	18
3.2 Antenna Theory . . . . .	20
3.2.1 Radiation Pattern . . . . .	20
3.2.2 Directivity . . . . .	21
3.2.3 Efficiency . . . . .	22
3.2.4 Absolute Gain . . . . .	22
3.2.5 Voltage Standing Wave Ratio and Return Loss . . . . .	23
3.2.6 Half Power Beamwidth . . . . .	25
3.2.7 Polarization . . . . .	25
3.2.8 Scattering Matrix . . . . .	26

3.3	Antenna Types . . . . .	26
3.3.1	Dipole Antennas . . . . .	28
3.3.2	Horn Antennas . . . . .	28
3.3.3	End Fire Tapered Slot Antennas . . . . .	28
3.3.4	Spiral Antennas . . . . .	29
3.3.5	Array Antennas . . . . .	29
3.4	Radar Waveforms . . . . .	30
3.4.1	Amplitude Modulation/Impulse . . . . .	30
3.4.2	Frequency Modulated Continuous Wave . . . . .	31
3.4.3	Stepped Frequency/Vector Network Analysis . . . . .	32
3.4.4	Noise Modulated; M-Sequence . . . . .	32
3.4.5	M-Sequence Parameters . . . . .	34
<b>4</b>	<b>Remote Sensing of Snow</b>	<b>39</b>
4.1	Snow Parameters . . . . .	39
4.2	Scattering Characteristics of Snow . . . . .	43
4.3	Characterizing Snow with UWB Radar . . . . .	49
4.3.1	Case study: Dix Equation . . . . .	51
<b>5</b>	<b>Radar System Development</b>	<b>55</b>
5.1	Antenna Development . . . . .	55
5.2	Hardware Development . . . . .	61
5.3	Software Development . . . . .	64
5.4	Final Remarks on the UWibaSS . . . . .	65
<b>6</b>	<b>Fieldwork</b>	<b>67</b>
6.1	MOSIDEO/CIRFA Experiment . . . . .	68
6.2	INTPART Cruise . . . . .	69
6.3	Statens Vegvesen Demo . . . . .	70
6.4	Freshwater Lake Experiment . . . . .	71
6.5	SIOS Field Campaign . . . . .	71
6.6	CAATEX Cruise . . . . .	72
6.7	Finnvikdalen Experiment . . . . .	74
<b>7</b>	<b>Overview of Publications</b>	<b>77</b>
7.1	Paper Summaries . . . . .	77
7.2	Other Publications . . . . .	79
<b>8</b>	<b>Paper I</b>	<b>83</b>
<b>9</b>	<b>Paper II</b>	<b>95</b>
<b>10</b>	<b>Paper III</b>	<b>123</b>

<b>11 Discussion and Conclusion</b>	<b>135</b>
11.1 Research Conclusions . . . . .	135
11.1.1 Contributions to State of the Art . . . . .	137
11.2 Future Work . . . . .	137
<b>A Miscellaneous Experiments</b>	<b>141</b>
A.1 Sea Ice Measurements with UAV Mounted Radar . . . . .	141
A.2 Freshwater Ice Measurements . . . . .	143
A.3 Rot in Wood Detection . . . . .	145
A.3.1 Test rig . . . . .	145
A.3.2 Results . . . . .	146
A.4 Differentiating Ice Types . . . . .	146
<b>Bibliography</b>	<b>149</b>



# List of Figures

3.1	Physical layout of an airborne radar system. . . . .	13
3.2	Resolution criteria for identical Gaussian envelopes. . . . .	17
3.3	Rayleigh criteria for unequal Gaussian envelopes. . . . .	17
3.4	Resolution criteria for detection of a weak target. . . . .	18
3.5	Reflection and transmission of electromagnetic wave. . . . .	19
3.6	Horizontal radiation pattern. . . . .	21
3.7	$S_{11}$ example. . . . .	25
3.8	Antenna types. . . . .	27
3.9	GPR system design options. . . . .	30
3.10	M-sequence generator. . . . .	35
3.11	Match Filter Output. . . . .	36
3.12	M-sequence transceiver. . . . .	36
4.1	Snow properties frequency of measurement. . . . .	40
4.2	Snow density modeled as a function of depth. . . . .	42
4.3	Snow penetration depth. . . . .	48
4.4	Constellation of A-scans from hyperbolic spreading function. . . . .	50
4.5	Dix's equation uncertainty. . . . .	52
5.1	The first iteration of the radar system. . . . .	57
5.2	The second iteration of the radar system. . . . .	58
5.3	The third iteration of the radar system. . . . .	60
5.4	Block diagrams of the UWIBASS. . . . .	62
5.5	Block diagram of the UWIBASS program workflow. . . . .	65
6.1	Fieldwork locations . . . . .	68
6.2	INTPART cruise locations. . . . .	69
6.3	Fieldwork locations for the SIOS campaign. . . . .	72
6.4	CAATEX cruise locations. . . . .	73
6.5	Map showing the location of the Finnvikdalen experiment. . . . .	75
11.1	Various ice thickness measurement techniques. . . . .	138
A.1	Sea ice interface detection. . . . .	142

A.2	Repeatability of the ice-interface measurements. . . . .	143
A.3	GPS position of the UAV. . . . .	144
A.4	Snow and ice thickness along transect. . . . .	144
A.5	Wood block. . . . .	145
A.6	A-scans of dry and wet wood. . . . .	146
A.7	Surface plot of mean backscattered energy from ice. . . . .	147

# List of Tables

3.1	Radar equation parameters. . . . .	14
3.2	RCS for selected geometries. . . . .	16
4.1	List of selected measurable snow properties. . . . .	41
5.1	Antenna design parameters. . . . .	56
5.2	UWiBaSS key characteristics. . . . .	66





# List of Abbreviations

**1D** one dimensional

**2D** two dimensional

**3D** three dimensional

**ACF** auto-correlation function

**ADC** analog-to-digital converter

**AWI** Alfred Wegener Institute

**CAATEX** coordinated arctic acoustic thermometry experiment

**CIRFA** Centre for Integrated Remote Sensing and Forecasting for Arctic Operations

**CW** continuous wave

**DAC** digital-to-analog converter

**EM** electromagnetic

**EMI** electromagnetic interference

**FFT** fast Fourier transform

**FMCW** frequency modulated continuous wave

**FPGA** field-programmable gate array

**FWHM** full width at half maximum

**GPR** ground penetrating radar

- GPS** global positioning system
- HPBW** half power beam width
- IEEE** Institute of Electrical and Electronics Engineers
- IR** infrared
- IRF** impulse response function
- LCR** large current radiator
- LWC** liquid water content
- MOSIDEO** Microscale interaction of oil with sea ice for detection and environmental risk management in sustainable operations
- MVA** migration velocity analysis
- PCB** printed circuit board
- PRBS** pseudo random binary sequence
- RCS** radar cross-section
- RF** radio frequency
- RTK** real-time kinematic
- RX** receiving
- SAR** Synthetic Aperture Radar
- SDR** software-defined radio
- SIOS** Svalbard integrated arctic earth observing system
- SLOC** source lines of code
- SNR** signal-to-noise ratio
- SWE** snow water equivalent
- T&H** track & hold

**TWT** two way travel time

**TX** transmitting

**UAV** unmanned aerial vehicle

**UWB** ultra wide-band

**UWiBaSS** ultra-wideband snow sounder

**VCO** voltage controlled oscillator

**VNA** vector network analyser

**VSWR** voltage standing wave ratio



# Selected Symbols

Sign	Description	Unit
$A$	Antenna aperture	[m <sup>2</sup> ]
$B$	Bandwidth of transmitted signal	[Hz]
$c$	Speed of light in free space	$\approx 0.2997$ [m/ns]
$\delta$	Penetration depth	[cm]
$d$	Depth	[m]
$e$	Efficiency	[%]
$E$	Electric field	[V/m]
$\epsilon$	Absolute permittivity of medium	[F/m]
$\epsilon_0$	Absolute permittivity of free space	$8.85 \times 10^{-12}$ [F/m]
$\epsilon_r$	Relative permittivity of medium	
$\epsilon'_r$	Real part of relative permittivity	
$\epsilon''_r$	Imaginary part of relative permittivity	
$f$	Frequency	[Hz]
$G$	Antenna gain	[dBi]
$\Gamma$	Reflection coefficient	
$j$	Imaginary unit	$\sqrt{-1}$
$\lambda$	Wavelength	[m]
$\omega$	Angular frequency	[rad/m]
$P_r$	Received power	[W]
$P_t$	Transmitted power	[W]
$R$	Range	[m]
$v$	Propagation velocity of EM-waves	[m/ns]
$S_{11}$	Return loss	[dB]
$\rho$	Density of medium	[g/cm <sup>3</sup> ]
$\mu$	Absolute permeability of medium	[H/m]
$\mu_0$	Absolute permeability of free space	$4\pi \times 10^{-7}$ [H/m]
$\mu_r$	Relative permeability of medium	





# Introduction

In the hydrological cycle, snow is considered the least described factor in the current knowledge of the global water budget and thus a critical component of the Earth's ecosystem [87]. This compound of ice-particles and air, formed by sublimation of vapour in the atmosphere, is very sensitive to climate change and causes strong feedback to climatic factors [7]. Snow-cover is strongly anti-correlated with air temperature [51], and in the ongoing change of conditions on the Earth, the snow-cover extent in the Northern Hemisphere decreases [42] as snow-cover formation and melt are closely related to a temperature threshold of 0 °C. Hence, snow measurements are essential for freshwater management, such as water supply and hydro-power generation, monitoring of climate changes, in addition to risk assessments connected to avalanches and floods. Lastly, some businesses such as ski resorts depend on snow-cover for their economic activity, and the seasonal evolution of the snow-cover is also a major concern in these areas.

Snow-cover can be regarded as a spatially and temporally integrated response to snowfall events, where the temperature during snowfall and melt situations determines central snowpack parameters such as depth, density, stratigraphy, and grain size. The combination of these parameters, in turn, determines several factors, including avalanche risk, snow water equivalent (SWE), and snow albedo [7].

With sparse *in situ* observations and vast snow-covered regions having limited accessibility, snow monitoring mostly relies on remote sensing [63, 78, 87].

However, aircraft or satellite snow observations have several limitations, including spatial resolution. Hence, *in situ* observations are essential in the snow assimilation scheme [63].

The Centre for Integrated Remote Sensing and Forecasting for Arctic Operations (CIRFA)<sup>1</sup> funds the work presented in this thesis in collaboration with NORCE, Norwegian Research Centre<sup>2</sup>. The focus of CIRFA is integrating remote sensing and forecasting, understood as the process of combining remote sensing data from various sensors, *in situ* information, and numerical models, for predictions of oceans and areas covered by sea ice. Snow-cover has a significant impact on sea ice parameters [124]. Most notably, snow causes a strong insulation effect reducing basal ice growth [74], alters freeboard where a heavy snowpack can cause negative freeboard and surface flooding [21], and during the melt season, melted snow can refreeze forming superimposed ice at the surface [52]. *In situ* measurements are traditionally performed manually with snow probes, drills, and density cutters. However, the area coverage is usually relatively low. Nevertheless, collected *in situ* data is used to validate satellite radar measurements generated on a much larger scale.

By mounting a high-resolution, nadir-looking radar to a drone, one can perform snow depth, density, and stratigraphy measurements covering large areas or transects up to 20 km for multi-rotor drones and as much as 500 km for fixed-wing drones. This application could prove useful for several other fields of work such as avalanche risk estimation, bulk snow estimation for hydro-power companies, as well as freshwater ice thickness estimation for ice road safety [47, 88]. Manual snowpack assessment is currently limited by the accessibility (by snowmobile or skis) and safety for the snow-professionals. Moreover, detailed mapping of avalanche risk could steer mountaineers towards safer areas of the mountain. With increasing traffic in mountain areas, a system producing more detailed avalanche risk estimations would be beneficial.

The development of high bandwidth radars reached a milestone when Fourier domain processing became viable in consumer processors. Fourier domain processing enabled the use of continuous wave (CW) signals that spread the frequencies and energy in time. A fast Fourier transform (FFT) can visualize the frequency shift between the transmitted and received signal after mixing. Alternatively, match filter processing (usually in the Fourier domain) re-focuses the signal after reception by correlating the transmitted signal with a stored waveform.

It is well known that radar systems can be used for subsurface sensing, but recent

1. Visit CIRFA at: <https://cirfa.uit.no/>.

2. Visit NORCE at: <https://www.norceresearch.no/>.



developments in RF electronics (namely integrated circuits) have opened up new possibilities for lightweight, high bandwidth radar systems more suitable for unmanned aerial vehicle (UAV) mounting. Traditional snow parameter monitoring and distribution mapping methods with radar entail sled-based ground penetrating radar (GPR) where the antennas are physically coupled to the ground or with a short (10 to 50 cm) distance to the snow surface. With this method, the area coverage and horizontal resolution are significantly greater than manual snow probe measurements. However, for regions with high avalanche risk or low accessibility, a drone-mounted radar system would be superior. The ability to perform autonomous surveys is also beneficial since grid or transect surveys are easily implemented as waypoints in the autopilot map. Additionally, the area coverage can be significantly increased, especially considering fixed-wing mounted radar with speeds up to 100 km/h.

Field verification is mandatory to validate and further develop such a radar system. Consequently, several field campaigns and experiments in collaboration with other institutes, startups, and projects such as SIOS<sup>3</sup>, The Norwegian Polar Institute (NPI)<sup>4</sup>, Varicon<sup>5</sup>, Statkraft<sup>6</sup>, and the Nansen Centre (NERSC)<sup>7</sup> have been a priority throughout this project.

The ability to remotely measure snow depth and density for any snow type could be considered the holy grail of drone-mounted snow radar [19]. Sources to non-invasively measure these parameters will give significant benefits to a number of industries and services as discussed above. However, several requirements need to be fulfilled in terms of radar system design to achieve this goal. The most central design parameters for UAV mounted radar could conceivably be listed as weight, form-factor, drag, range resolution, antenna gain/directivity, signal-to-noise ratio (SNR), and signal penetration depth. Unfortunately, there are usually tradeoffs between some of these parameters, and hence compromises have to be made. These compromises are discussed throughout this thesis.

## 1.1 Thesis Outline

The field of GPR is especially appealing to engineers and scientists (ideally combinations) due to its wide range of disciplines. Developing and operating GPR systems stretch across the field of electromagnetic wave propagation in lossy media via ultra-wideband antenna technology to radar systems design

3. Visit SIOS at: <https://sios-svalbard.org/>

4. Visit NPI at: <https://www.npolar.no/>

5. Visit Varicon at: <https://varicon.no/>

6. Visit Statkraft at: <https://www.statkraft.no/>

7. Visit NERSC at: <https://www.nersec.no/>

and fieldwork. Also, analyzing the recorded data covers coherent waveform signal processing, image processing, and method development. These topics are more or less covered by each paper (Papers I-III).

The three papers are:

**Paper I:** R. O. R. Jenssen, M. Eckerstorfer & S. Jacobsen "**Drone-Mounted Ultrawideband Radar for Retrieval of Snowpack Properties**", IEEE Transactions on Instrumentation and Measurement, vol. 69, no. 1, pp. 221-230, Jan. 2020

**Paper II:** R. O. R. Jenssen & S. Jacobsen "**Drone-mounted UWB snow radar: technical improvements and field results**", Journal of Electromagnetic Waves and Applications, 2020, 34:14, 1930-1954.

**Paper III:** R. O. R. Jenssen & S. Jacobsen "**Measurement of Snow Water Equivalent Using Drone-Mounted Ultra Wide-Band Radar**", In review.

These papers compose the research contributions of the thesis, and the main objectives are:

- To develop an instrument for UAV remote sensing of snow.
- To investigate the various applications for such a system and perform field trials.
- To propose methods to extract snow state parameters, and techniques to improve signal integrity and clutter rejection.

Other published papers (as first author or co-author) are left out of this thesis, but listed in Section 7.2.

The thesis is structured as follows:

**Chapter 3** provides an introduction to the basic concepts of antenna theory and ultra wide-band (UWB) GPR systems.

**Chapter 4** covers fundamental snow parameters and reviews commonly used methods to measure some of these parameters. This chapter also presents snow as an electromagnetic medium and discusses how we can use microwaves to estimate snow parameters.

**Chapter 5** presents the iterations of the radar system prototype, where we discuss design parameters and special considerations in each domain of

development; that is, hardware and software, where hardware is divided into the sub-fields of antenna and system development, while software development is divided into data acquisition and post-processing.

**Chapter 6** describes the field campaigns conducted during this project.

**Chapter 7** summarizes the papers that compose the research contributions of this thesis and other published work.

**Chapters 8-10** presents Papers I-III.

**Chapter 11** concludes this thesis and presents future work.

**Appendix A** presents preliminary work in related subjects using UWB radar.





## Previous Work

### 2.1 Ground Penetrating Radar on Snow

ground penetrating radar (GPR) has been used to measure snow properties for decades [30, 112]. Recent advances in GPR technology have enabled high spatial resolution and sensor systems that are easy to operate and mount on relatively small platforms.

In terms of GPR measurements of the subsurface, a limited amount of work has been done on ultra wide-band (UWB) measurements on snow in comparison to other media. Nevertheless, previous studies have shown correlations between snowpit and radar measurements. Early work by [30] and [37] show that surface and ground layers are easily detected. Ellerbrugh and Boyne [22] investigated the amplitude of scattered radiation as a function of depth in the snowpack and the possibility to correlate backscatter with physical characteristics such as density, hardness, stratigraphy, and moisture content in order to estimate snow water equivalent (SWE) of the snowpack.

Studies using impulse radar [56, 67] revealed that such systems are sensitive to layering in the snow and that SWE could, to some degree, be estimated.

Several studies using frequency modulated continuous wave (FMCW) radar [50, 55, 70, 71, 84, 96] show that the most prominent structures in the snowpack are detectable with radar using ground-based measurement platforms. For instance, an 8 to 18 GHz FMCW system was found to generate stratigraphic

snow information with a correlation coefficient of 0.92 relative to *in situ* depth measurements [71]. Using a commercially available (GSSI SIR-3000) 1 GHz GPR showed a correlation coefficient of 0.86 [100] between GPR and *in situ* snow depth. Even though high correlations are achieved, one should notice that so far it is only at situations with shallow snow depths up to 30 cm in [71] and 80 cm in [100].

Ground-based GPR systems (both commercial and prototypes) have demonstrated the capability for sea ice measurements [38, 64]. For example, a gated step-frequency GPR operating in the 0.5 to 3 GHz range was tested on glacial ice and permafrost on Svalbard and demonstrated snow and ice measuring capabilities to a depth of 11 m from a snowmobile platform [80].

Ground-based GPR can also be used for below snow crevasse detection to improve safety when navigating on glaciers [20, 100].

## 2.2 Airborne GPR

A large air-gap between the antennas and the medium of interest introduces new challenges and design considerations compared to ground-coupled or short air-gap GPR. Nonetheless, airborne GPR is shown to be feasible both theoretically [11] and in practice [120].

In [27, 59, 82, 92, 121] FMCW radars are used to measure snow and ice thickness from an aircraft. Yan *et al.* [120] show aircraft-mounted snow depth measurements with 0.88 correlation relative to *in situ* measurements.

Sea ice thickness measurements from helicopter platforms have also been demonstrated [77], using the commercially available RAMAC GPR. Rückamp *et al.* [94] show ice cap penetration down to the bedrock from a helicopter platform using the 30 MHz BGRP30-System developed at the Institute of Geophysics (University of Munster). Moreover, helicopter-based radars have also shown the ability to detect oil-spills under snow from helicopter platforms using thin-layer reflection analysis [6].

Design parameters for a unmanned aerial vehicle (UAV)-mounted radar intended for snow parameter retrieval was established in [104], with a recommended operating frequency in the 1.5 to 4.5 GHz band. More recent field trials from the same group demonstrate snow depth accuracy of  $\pm 9.1$  cm from an airborne UAV [105]. Moreover, several other research groups have described UWB radars for UAV mounting, where the applications range from detection of ground targets such as cars and humans [61, 62], or ships [106] to topographic

mapping [65], detection of buried objects including landmines [101] and other high scattering targets [122].

Additionally, previous investigations of UAV-mounted software-defined radio (SDR) GPR show great promise [25], and a 1.5 to 9 GHz SDR system is presented in [10]. Furthermore, [119] presents an SDR based radar system for soil moisture mapping. SDR based systems are highly user-configurable where the center frequency and bandwidth can be changed in software and hence during operation in the field.

GHz range UWB radars are relatively simple to mount on UAV compared to MHz radars, due to the smaller antenna size [119]. For fixed-wing UAV, Arnold *et al.* [3] tackle the challenge of using large MHz antennas by using tapered dipole antennas, taped on the wings, with a 35 MHz center frequency (approx. 2 MHz BW). Additionally, a 14 MHz (approx. 1 MHz BW) antenna is mounted along the wings and back to the tail section using a combination of copper tape and wires. The impedance matching of these antennas is acceptable, and the low weight and small (flat) form factor is adequate for UAV mounting. However, dipole antennas can be considered omnidirectional in the plane perpendicular to the radiating element, and hence are weakly directional when mounted horizontally. Arnold *et al.* [3] also outlines the processing steps for along-track SAR focusing of the data (using F-K migration) with further references.

Drone-mounted Synthetic Aperture Radar (SAR) studies demonstrate the possibility of landmine detection with polarimetric SAR [9]. Antenna arrays for GPR systems on drones [93] yield a wider swath when flying in gridded flights, potentially extending area coverage.

There exist commercially available GPR systems that meet the size and weight requirements of UAV mounting<sup>1</sup>. However, several improvements can be made regarding weight, size, and integration with the UAV both mechanically and digitally (i.e., data synchronization for geo-referencing and post-processing).

## 2.3 Snow parameter estimation methods

The scientific study of snow stratigraphy began in the 18th century; however, tools to perform quick, objective, and non-invasive measurements have not been available until recent years [85].

The ground below the snowpack in mountainous and marshland areas often

1. Radarteam: <http://www.radarteam.se/>

contains sparse scattering objects, potentially producing diffraction hyperbolas in a radar B-scan. These objects are usually rocks with a relative permittivity ( $\sim 4-7$ ) different from snow. Migration methods applied on radar imagery at the correct propagation velocity of the intermediate medium cause the hyperbolas to collapse at their focal point. Previous studies using commercial GPR, mounted on a snowmobile, show that SWE can be estimated using F-K migration and manual velocity picking [36]. A similar method also demonstrates auto-focusing using the varimax norm to automatically pick the velocity [12]. Similar results can be produced from offset antenna arrays [31]. Furthermore, Kirchhoff's time migration with a two-layered variable-depth velocity model was used to focus radar image GPR-data from a helicopter platform [95].

Other work shows SWE estimation using manually measured snow depths, snow age, and snow class defined by the location [8]. Manual depth measurements at calibration locations can also be used to estimate SWE with radars [115].

Lundberg *et al.* [67] presents a simple linear model between the radar two way travel time (TWT) and SWE on the form  $SWE = aTWT + b$  where the values of  $a$  and  $b$  are estimated. Furthermore, Lundberg *et al.* [68] also estimate the modifications to the model for wet snow.

Some studies take the concept a step forward and outline methods for automatic detection and segmentation of diffraction hyperbolas. This research includes novel image threshold methods and clustering [17], parabolic fitting [126], apex detection by fitting an analytical hyperbola function to the profile edges detected with a Canny filter [75], template matching algorithms [98], and a neural network approach [5]. Automatic object detection using dynamic time warping is a method that computes a dissimilarity measure between the radar scenario and a reference signal [44] and could be used to locate diffraction hyperbolas prior to segmentation.



# / 3

## Ground Penetrating Radar Theory

The ability to image the ground beneath our feet has fascinated humankind for centuries. However, no single technique can reveal the subsurface composition completely, and thus there are several different methods to image different materials and targets. Seismic imaging, gravity surveying, electrical resistivity, induced polarization, magnetic surveying, nucleonic, radiometric, thermographic, and electromagnetic are all methods to probe the subsurface [14]. Within these, ground penetrating radar (GPR) is a particularly viable approach.

The term GPR refers to a range of electromagnetic techniques designed for locating objects or imaging of the subsurface. The term might be too restrictive as the usage of GPR includes several other surfaces than the ground, e.g., walls, bridges, and even snow.

The design of a GPR system is hugely application dependant where the waveform, software, and hardware selections, are based on the target and the medium under investigation.

GPR applications include [14]:

- Archaeological investigations
- Borehole inspection
- Bridge deck analysis
- Building condition assessment
- Contaminated land investigation
- Detection of buried mines (anti-personnel and anti-tank)
- Evaluation of reinforced concrete
- Forensic investigations
- Geophysical investigations
- Medical imaging
- Pipes and cable detection
- Planetary exploration
- Rail track and bed inspection
- Remote sensing from aircraft and satellites
- Road condition survey
- Security applications
- *Snow, ice and glacier measurements*
- Timber condition
- Tunnel lining inspection
- Wall condition assessment

The GPR technique is in essence not very different from free-space radar. However, GPR needs special consideration with respect to parameters that govern the medium and target, i.e. propagation loss, target characteristics, and clutter.

The next sections describe the basic principles and design considerations used to develop the radar system presented in this thesis. These sections cover basic radar theory, antenna theory, antenna types, and popular waveforms.

### 3.1 Operating Principle

Airborne GPR is a subsurface penetrating radar system that can be mounted on a flying platform to provide high-resolution images of the subsurface. Each radar measurement can be regarded as a one dimensional (1D) vector containing the backscattered power from a set of time delays in the nano-second range. Utilizing the movement of the airborne platform, each 1D measurement

can be synthesized into a two dimensional (2D) image showing a stratigraphical image of the subsurface, also called A-scan and B-scan, respectively.

A radar system that transmits and receives electromagnetic waves by the same antenna is called a monostatic radar system. Conversely, a bistatic radar system uses separate antennas for transmission and reception.

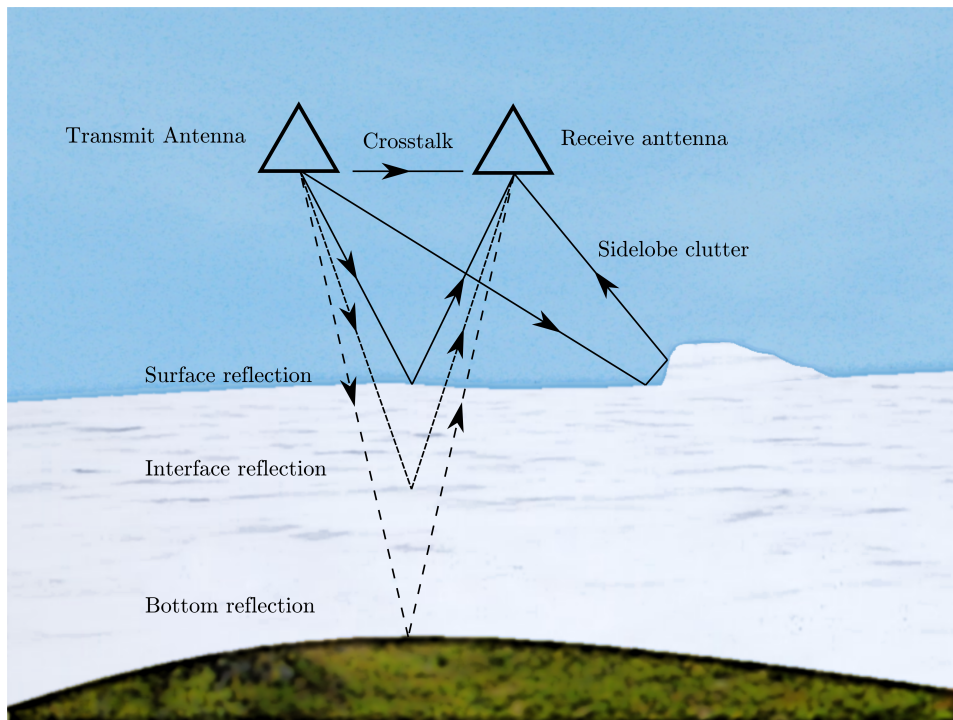


**Figure 3.1:** Physical layout of an airborne nadir-looking bistatic radar system. Not taking into account refraction.

The operating principle of an airborne bistatic GPR system can be described as in Figure 3.1, where five main backscatter categories can be classified as follows:

- Crosstalk; the direct wave from the transmitting to the receiving antenna. Usually the strongest signal in the radar data.
- Surface reflections; the first significant reflection of interest in the radar scene.
- Interface reflection; internal reflections in the medium of interest (stratigraphy).
- Bottom reflection; the last reflection of interest in the radar scene, and

usually the last detectable interface.

- Sidelobe clutter; reflections that are coming from objects outside the main lobe of the antenna. Usually not of interest.

### 3.1.1 The Radar Equation

An intuitive understanding of the radar equation is central for any radar systems developer. The radar equation describes the physical dependencies of the received power, which is the wave propagation from the transmitted power - centrally described as a function of range, losses, target characteristics, antenna gain, and aperture.

The radar equation for a bistatic radar can be formulated as a function of peak received power [107] as:

$$P_r = \frac{P_t G_t A_r \sigma L}{(4\pi)^2 R_t^2 R_r^2} , \quad (3.1)$$

where each parameter is defined in table 3.1.

**Table 3.1:** Radar equation parameters.

Parameter	Description
$P_r$	Received Power
$P_t$	Transmitted Power
$G_t$	Gain of transmitting antenna
$A_r = \frac{G_r \lambda^2}{4\pi}$	Effective aperture of receiving antenna
$G_r$	Gain of receiving antenna
$\lambda$	Transmitted wavelength
$\sigma$	Radar cross section of the target
$L$	Pattern propagation factor (total loss factor)
$\Gamma(\theta)$	Fresnel power reflection coefficient
$R_t$	Distance from the transmitter to the target (range)
$R_r$	Distance from the target to the receiver (range)

The effective aperture of the receiving antenna  $A_r$  is usually taken to be that portion of a plane surface near the antenna, perpendicular to the direction of maximum radiation, through which most of the radiation flows [48]. The

effective aperture can be rewritten in terms of the antenna gain:

$$A_r = \frac{G_r \lambda^2}{4\pi} , \quad (3.2)$$

and in the most common case, where the transmitting and receiving antenna is identical ( $G_t = G_r = G$ ) and approximately in the same location ( $R_t \approx R_r \approx R$ ), we get:

$$P_r = \frac{P_t G^2 \lambda^2 \sigma L}{(4\pi)^3 R^4} . \quad (3.3)$$

A central factor in the radar equation is how the received power decreases as a function of the range  $R$ . The received power is also a function of the target radar cross-section (RCS)  $\sigma$  and is expressed in Equation (3.3) in terms of a point target.

A more adequate RCS of the radar equation for low altitude snow measurements is that of a flat surface. If the flat surface is larger than two Fresnel zones laterally, we can rewrite the radar equation into [111]:

$$P_r = \frac{P_t G^2 \lambda^2 \Gamma(\theta) L}{(4\pi)^2 (2R)^2} , \quad (3.4)$$

where  $\Gamma(\theta)$  is the Fresnel power reflection coefficient, similar to Equation (3.18), however, also accounting for the incidence angle [50]. The radius  $F_n$  of Fresnel zone  $n$  is defined as [111]:

$$F_n = \frac{n\pi}{2} \sqrt{\frac{R\lambda}{2}} . \quad (3.5)$$

Here,  $n$  is the Fresnel zone number,  $R$  is the distance to the target, and  $\lambda$  is the wavelength of the transmitted signal.

Paper I [46] discusses whether this requirement is satisfied for the radar system used in this thesis.

Some RCS for simple geometries can be expressed as in table 3.2.

**Table 3.2:** RCS for selected geometries.

Geometry	RCS
Sphere with radius $a$	$\sigma_s = \pi a^2$
Flat plate with height $a$ and width $b$	$\sigma_p = \frac{4\pi a^2 b^2}{\lambda^2}$
Cylinder with radius $a$ and height $h$	$\sigma_c = \frac{2\pi a h^2}{\lambda}$

Even though the dependence between received power and range is reduced from  $R^4$  to  $(2R)^2$ , Equation (3.4) shows that increasingly distant targets become significantly harder to detect. The loss of power as a function of range is called spreading loss  $L_s$  and is defined as the ratio of the received power to the transmitted power omitting additional losses [14]:

$$L_s = -10 \log_{10} \frac{G^2 \lambda^2 \sigma}{(4\pi)^3 R^4} \quad (3.6)$$

Similarly, for a flat surface target:

$$L_s = -10 \log_{10} \frac{G^2 \lambda^2 \sigma}{(4\pi)^2 (2R)^2} \quad (3.7)$$

### 3.1.2 Resolution of UWB Signals

Several GPR applications only require the depth measurement of a single interface, such as ice thickness measurements or road layer thickness. In such cases, depth can be determined with adequate accuracy by measuring the elapsed time (i.e., two way travel time (TWT)) between the leading edge of the received wavelet and a known reference time such as the surface reflection provided the propagation velocity is known to some accuracy. In the layout shown in Figure 3.1 such a measurement would detect the bottom reflection only.

Nevertheless, suppose the task is to detect a number of features within the medium to a certain accuracy, such as the detection of thin layers or rocks. In that case, a signal having a larger bandwidth is required to distinguish between the various targets. Moreover, it is really the received signal bandwidth that needs to be wide, taking into account antenna effects and absorption in the medium. Typical subsurface media act as low-pass filters that modify the transmitted spectrum in accordance with the electrical properties of the propagating medium [14]. A transmitted pulse is effectively stretched wider

as a function of attenuation, which again is a function of the complex electric permittivity and magnetic permeability of the medium.

The standard Rayleigh criterion for resolution refers to the minimum time interval, which allows two overlapping pulses to be separated by a  $-3$  dB depression of the sum signal. A similar way to measure range resolution is to evaluate the full width at half maximum (FWHM) of a single pulse, which will produce equivalent results if the pulses are identical. Figure 3.2 shows a simulation of the resolution criteria for two identical Gaussian envelopes produced at 3 GHz center frequency with a bandwidth of 5 GHz.

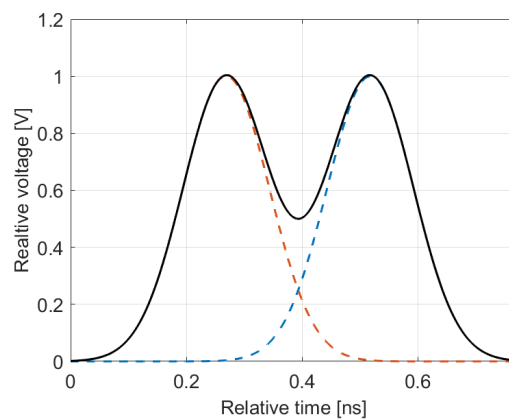


**Figure 3.2:** Resolution criteria for identical Gaussian waveform envelopes.

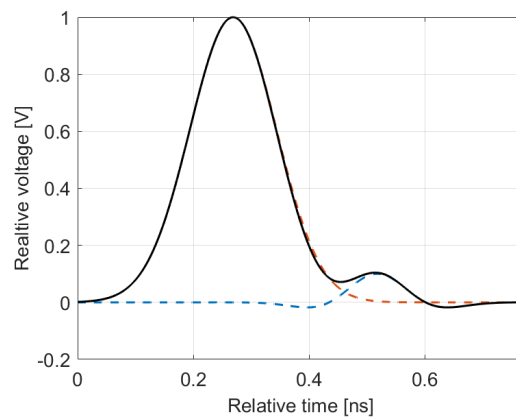


**Figure 3.3:** Rayleigh criteria for unequal Gaussian waveform envelopes.

In a lossy medium with targets having different radar cross-sections, the Rayleigh criteria become unsuitable in the case where the reflected signal from one target is significantly lower than of the other, as seen in Figure 3.3.

In this case, one might consider a different criterion for range resolution to distinguish between pulses of different sizes. Figure 3.4 shows an example criteria where the separation must be equal to the width of the greater signal at a level of 10% of its peak value [14].

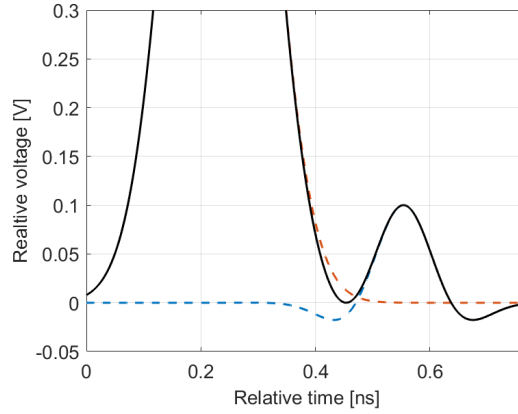


**Figure 3.4:** Resolution criteria for detection of a weak target adjacent to a strong target.

For practical purposes, radar developers usually use the theoretical range resolution to start with, and so did we throughout this project. Theoretically, the range resolution  $\Delta r$  of a pulse compression radar system is given by [91]:

$$\Delta r = \frac{c}{2B} \frac{1}{\sqrt{\epsilon_r}} \quad , \quad (3.8)$$

where  $c$  is the propagation velocity in free space,  $B$  is the radar system bandwidth, and  $\epsilon_r$  is the relative permittivity of the medium, described in more detail in Section 4.2.

### 3.1.3 Scattering Mechanisms

In addition to attenuation, scattering effects also account for some losses. However, in the returning wave, scattering mechanisms are needed as they facilitate the ability to perform subsurface measurements with electromagnetic waves.

When an electromagnetic wave is incident on a dielectric boundary, a portion of the energy is reflected and the rest is transmitted further into the medium, as seen in Figure 3.5. Snell's law describes the relationship between the directions



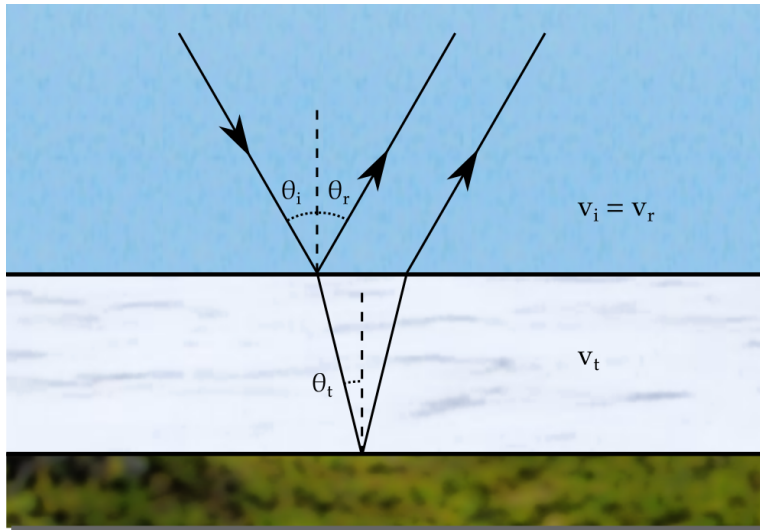


**Figure 3.5:** Reflection and transmission of incident electromagnetic wave at an interface.

of the incident, reflected, and transmitted wave [14]:

$$\frac{\sin \theta_i}{v_i} = \frac{\sin \theta_r}{v_r} = \frac{\sin \theta_t}{v_t} \quad , \quad (3.9)$$

where  $\theta_i$ ,  $\theta_r$ , and  $\theta_t$  is the angle of the incident, reflected, and transmitted signal respectively, and  $v_i$ ,  $v_r$  and  $v_t$  are the corresponding velocities. This type of scattering is called surface scattering.

The roughness of the dielectric boundary influences the radiation pattern of the reflected signal. A perfectly smooth surface will cause specular reflection, which has a theoretical radiation pattern of a delta function. In practice, as the surface roughness increases, the diffuse component of the reflected signal increases, and the coherent part decreases.

In heterogeneous media, the transmitted signal will experience further scattering within the medium due to local dielectric variations. This is called volume scattering and will severely limit the penetration depth as the total loss an electromagnetic wave experiences in a medium is the sum of all the scattering losses and attenuation. Volume scattering is generally weaker than surface scattering since the energy is scattered in multiple directions.

Finally, double-bounce scattering is when surface scattering occurs two times in the propagation path, such as the sidelobe clutter in Figure 3.1.

## 3.2 Antenna Theory

Arguably, the most important part of any radar system is the antenna. The Institute of Electrical and Electronics Engineers (IEEE) defines the antenna as: “*That part of a transmitting or receiving system which is designed to radiate or to receive electromagnetic waves.*” [41]. Such a device is a central part of any radar system. In other words, the role of the radar antenna is to couple the free-space and guided-wave propagation of electromagnetic waves.

A directional antenna concentrates the radiated energy into a shaped directive beam that illuminates the target in the desired direction. The reflected energy is then collected by the receiving antenna, which could (or even should) be the same antenna, and is then usually filtered and sampled by the radar receiver. A typical ultra wide-band (UWB) continuous wave (CW) system utilizes two antennas; one for transmitting and one for receiving. This configuration is due to the simplicity of implementing separate receiver and transmitter channels, when probing in the near-field, instead of using directive coupling or gating on a single output port. The reciprocal behavior of antennas means that the optimum match is when the two antennas are identical. Some of the most applied parameters to characterize antennas are; radiation pattern, gain, voltage standing wave ratio (VSWR), and half power beam width (HPBW) (see below for definitions).

### 3.2.1 Radiation Pattern

The radiation pattern is the spatial distribution that characterizes the electromagnetic field generated by the antenna and can be written as a function  $U(\theta, \phi)$  in spherical coordinates. Usually, it is a 2D plot of the amplitude or power pattern of the antenna in a selected plane.

In Figure 3.6, we see the horizontal radiation pattern of a general directional antenna. This particular antenna is, to some degree, bidirectional as it has a significant backward lobe  $180^\circ$  away from the main lobe. An omnidirectional antenna has approximately the same amplitude in all directions in at least one plane.

Assuming the antenna is stationary or moving relatively short compared to the distance traveled during the acquisition time of the radar system, we can imagine at each sampled data point a collection of several returning pulses from different scattering objects. These reflected pulses become part of a weighted sum where each returning pulse has a weight based on their direction of arrival. This effect is inherent in any radar system and is caused by the antenna radiation pattern.

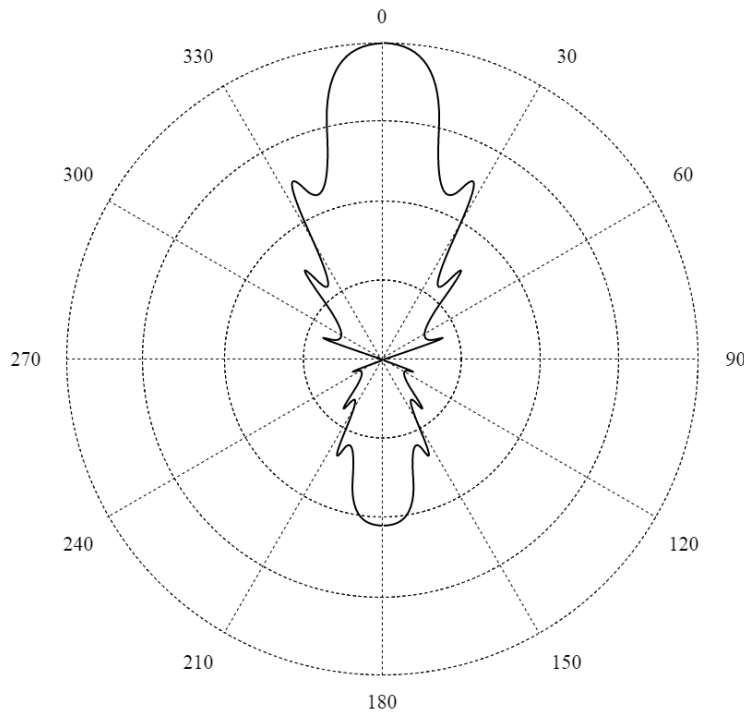


Figure 3.6: Horizontal radiation pattern for a directional antenna.

### 3.2.2 Directivity

Directivity is defined as: “The ratio of the radiation intensity in a given direction from the antenna to the radiation intensity averaged over all directions. The average radiation intensity is equal to the total power radiated by the antenna divided by  $4\pi$ . If the direction is not specified, the direction of maximum radiation intensity is implied.” [41]. Directivity is a measure of how ‘directional’ an antennas radiation pattern is, and technically a function of angle, expressed as [48]:

$$D(\theta, \phi) = \frac{U(\theta, \phi)}{\frac{1}{4\pi} \int_0^{2\pi} \int_0^\pi |U(\theta, \phi)|^2 \sin\theta d\theta d\phi} = \frac{4\pi U(\theta, \phi)}{P_{rad}} \quad [\text{dBi}] \quad , \quad (3.10)$$

where  $U(\theta, \phi)$  is the radiation intensity (or radiation pattern), which is the power density per unit solid angle, and  $P_{rad}$  is the total radiated power. A solid angle is known as the angle of the antenna main lobe (maximum radiation). Antenna directivity is usually referenced to the radiation intensity of an isotropic source [41]. Hence, it is given in the unit dB-isotropic or dBi.

Directivity is a function of angle, but usually, when specifying directivity for an antenna, the peak directivity  $D_{max}$  is given.

$$D_{max} = \frac{4\pi U(\theta, \phi)_{max}}{P_{rad}} \quad [\text{dBi}] \quad , \quad (3.11)$$

### 3.2.3 Efficiency

The efficiency of an antenna can be described as the ratio of the power delivered to the antenna ( $P_{in}$ ) relative to the power radiated from the antenna ( $P_{rad}$ ). That is, a high-efficiency antenna radiates most of the power available at the antenna input terminals. If most of the power is absorbed within the antenna, it is considered a low-efficiency antenna, basically producing heat. Antenna efficiency is a ratio presented as a number between 0 and 1, often quoted in terms of percentage (e.g., 0.5 is 50 %) [48]:

$$e = \frac{P_{rad}}{P_{in}} \quad . \quad (3.12)$$

This measure takes into account the reflection, conduction, and dielectric efficiency of the antenna. Except for reflection, these terms are difficult to measure individually. However, numerical computation can be used to identify the different loss factors.

If the reflection coefficient  $\Gamma$  is known, the reflection efficiency  $e_r$  can be calculated as:

$$e_r = (1 - |\Gamma|^2) \quad , \quad (3.13)$$

which is related to return loss (see Section 3.2.5).

### 3.2.4 Absolute Gain

An antenna's ability to concentrate energy in a narrow angular region (a directive beam) is described in terms of antenna gain [41]. We can define antenna gain as the ratio of the peak radiated power compared to the mean

radiation intensity of a perfectly efficient antenna  $P_{in}/4\pi$  [48]:

$$G = \frac{4\pi U(\theta, \phi)_{max}}{P_{in}} \quad [\text{dBi}] \quad . \quad (3.14)$$

Absolute gain is more commonly quoted than directivity because it takes into account the efficiency of the antenna.

Antenna gain can be related to directivity and antenna efficiency by [48]:

$$G = eD_{max} \quad . \quad (3.15)$$

Partial gain is defined as the absolute gain related to a given polarization [41].

High-gain antennas such as horns or reflectors are said to be aperture-type antennas. The gain of these antennas can be described with the effective antenna aperture  $A$  from Equation (3.2). In this case, we need to introduce the aperture efficiency  $e_a$ , which includes the previously mentioned antenna efficiency  $e$  and the antenna illumination efficiency. The gain can then be expressed as:

$$G = e_a \frac{4\pi}{\lambda^2} A \quad . \quad (3.16)$$

### 3.2.5 Voltage Standing Wave Ratio and Return Loss

For a signal source to efficiently deliver power to an antenna, the impedance of the source and (or) transmission line must be well matched to the impedance of the antenna. This requirement also applies to the impedance matching between the receiving antenna and transmission line as well as internal components within the radar hardware.

The voltage standing wave ratio (VSWR) is directly related to the performance of the antenna as it is a measure of how well matched the antenna is to the transmission line or transceiver system. Power reflected by an antenna back onto the transmission line interferes with the forward traveling power, creating a standing voltage wave. The ratio between the maximum and minimum standing wave is the VSWR. In return, this depends on the reflection coefficient

$\Gamma$  at the input terminals of the antenna [89]:

$$VSWR = \frac{V_{max}}{V_{min}} = \frac{1 + |\Gamma|}{1 - |\Gamma|} . \quad (3.17)$$

The reflection coefficient for guided microwaves is defined as [89]:

$$\Gamma = \frac{Z_{in} - Z_0}{Z_{in} + Z_0} , \quad (3.18)$$

where  $Z_0$  is the characteristic impedance of the transmission line and  $Z_{in}$  is the input impedance of the antenna. These impedances are frequency dependent, which must be taken into account when working with UWB systems since antenna design considerations can alter the rate of change in impedance within the operational frequency band. Generally, UWB antennas are designed for minimal impedance variation across the operational bandwidth.

In other words, VSWR describes the frequency-dependent impedance matching between two ports such as antenna and transceiver. Bandwidth is described as *“The range of frequencies within which the performance of the antenna, with respect to some characteristic, conforms to a specified standard.”* [41], and is therefore, closely related to VSWR.

VSWR can also be related to antenna mismatch loss, also called return loss or  $S_{11}$ :

$$S_{11} = -20 \log |\Gamma| . \quad (3.19)$$

The scattering parameter  $S_{11}$  is described in Section 3.2.8.

Figure 3.7 shows an example of  $S_{11}$  for a UWB antenna. In practice, the bandwidth of an antenna is commonly defined as the range of frequencies with  $S_{11}$  below  $-10$  dB [49]. When measuring  $S_{11}$  in practice, it is not only the impedance mismatch at the antenna termination that will cause reflections, but also internal reflections in the antenna construction and especially reflections from the impedance matching between the antenna and free space. Hence, time-gating of the measurement is needed to measure the impedance matching at the antenna terminal solely. However, for most practical applications,  $S_{11}$  measurements include all the different antenna reflections as it is the sum that determines the antennas overall performance.

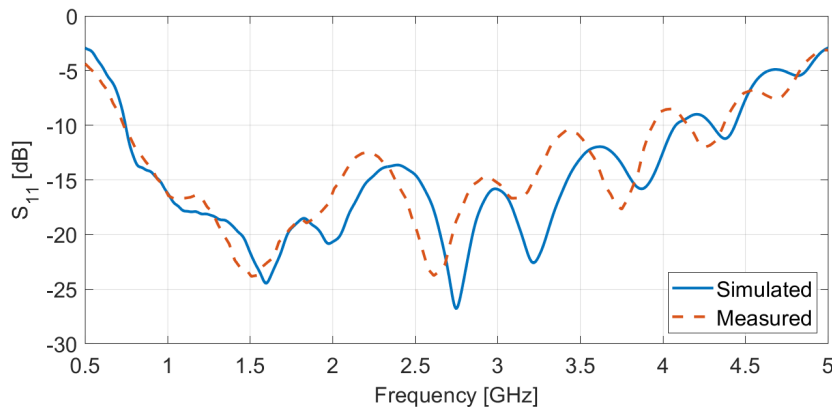


Figure 3.7:  $S_{11}$  example of UWB antenna.

When measuring  $S_{11}$ , an-echoic chambers (alternatively large halls or free-space) should be used to avoid reflections from walls and other obstacles producing clutter in front of the antenna.

### 3.2.6 Half Power Beamwidth

The half power beam width (HPBW) is defined by the IEEE as: “In a plane containing the direction of the maximum of a beam, the angle between the two directions in which the radiation intensity is one-half the value of the beam” [41]. The half-power beamwidth describes the width of the main beam of the antenna radiation pattern. In other words, the angular separation in which the maximum magnitude of the power radiation pattern decreases by 50% (-3 dB).

HPBW is an adequate measure to distinguish different types of antennas in terms of directivity and indicates the footprint of the antenna. It can also be used as a measure of the transversal resolution.

### 3.2.7 Polarization

Polarization is defined by IEEE as: “In a specified direction from an antenna and at a point in its far field, the polarization of the (locally) plane wave, which is used to represent the radiated wave at that point.” [41]. The electric field is perpendicular to the direction of propagation, and it is the direction of this electric field that is the polarization of the electromagnetic wave. The polarization is the figure that the electric field traces out while propagating. Typical polarizations used in radar sensing tasks are linear, circular, and hybrid polarization.

### 3.2.8 Scattering Matrix

A microwave network represented in terms of incident, reflected, and transmitted waves can be mathematically represented by a scattering matrix. The scattering matrix provides a complete description of the network as seen at its  $N$  ports. The scattering matrix relates the voltage waves incident on the ports to those reflected from the ports [89]. The scattering parameters are typically measured by a network analyzer, where the most used parameter in terms of antenna design is the antenna mismatch loss  $S_{11}$  also known as return loss described in Section 3.2.5.

The scattering matrix (also known as S-matrix) is defined in relation to the amplitude of the incident  $V_N^i$  and reflected  $V_N^r$  voltage waves as:

$$\begin{bmatrix} V_1^r \\ V_2^r \\ \vdots \\ V_N^r \end{bmatrix} = \begin{bmatrix} S_{11} & S_{12} & \dots & S_{1N} \\ S_{21} & S_{22} & \dots & S_{2N} \\ \vdots & \vdots & \ddots & \vdots \\ S_{N1} & S_{N2} & \dots & S_{NN} \end{bmatrix} \begin{bmatrix} V_1^i \\ V_2^i \\ \vdots \\ V_N^i \end{bmatrix} \quad (3.20)$$

where a specific element in the S-matrix can be determined as:

$$S_{mn} = \frac{V_m^r}{V_n^i} \quad , \quad (3.21)$$

where incident voltages on other ports than port  $n$  is zero (terminated with matched loads). We can find  $S_{mn}$  by driving a port  $n$  with an incident wave of voltage  $V_n^i$  and measure the reflected or transmitted amplitude  $V_m^r$  at port  $m$ .

## 3.3 Antenna Types

Antennas come in a wide variety of shapes and configurations, where the only broad common factor is that the radiating element is made from conductive materials. This section briefly summarizes the most frequently used GPR antennas, shown in Figure 3.8.



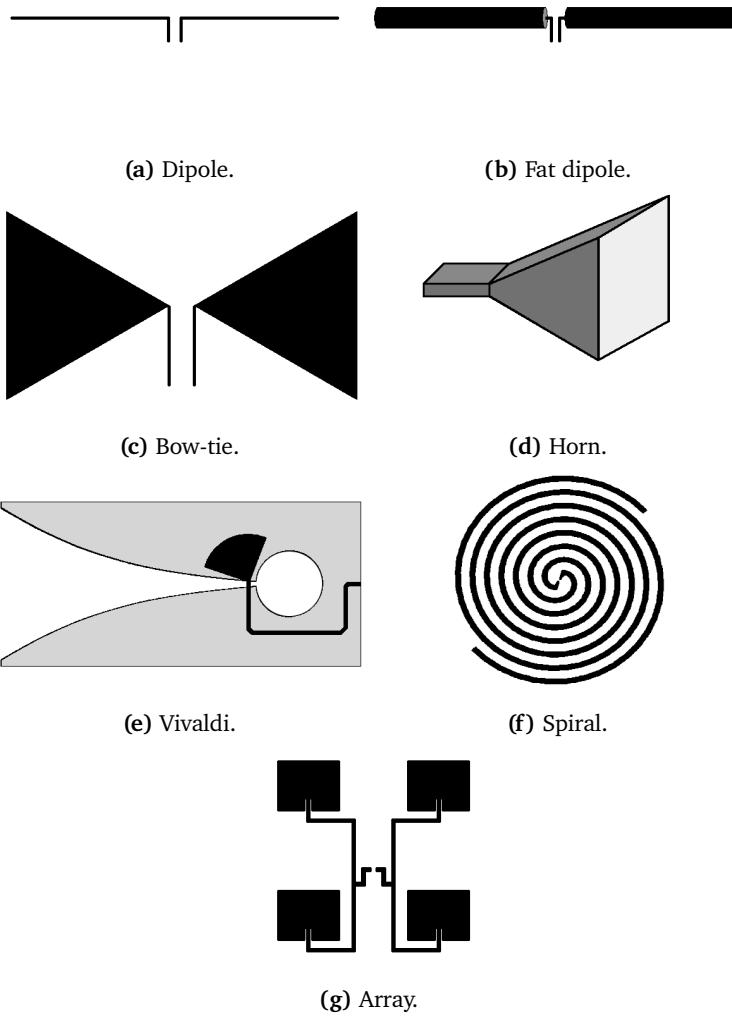


Figure 3.8: Antenna types.

### 3.3.1 Dipole Antennas

Perhaps the most widely used antenna type considering all applications, the dipole antenna (see Figure 3.8a) in essence consists of two identical radiating conductors usually oriented such that the total length is approximately one half of the signal wavelength. These antennas generally show low directivity and bandwidth, however by thickening the conductors, such as in Figure 3.8b, or implementing planar solutions such as bow-tie antennas in Figure 3.8c, the bandwidth can be increased. The most popular dipole type for GPR applications is the bow-tie antenna due to its ease of construction with printed circuit board (PCB) methods and the possibility for UWB characteristics. The flare angle of the bow-tie strongly affects the radiation pattern and input impedance (hence, VSWR) and can be tuned to best fit the application. Bow-tie antennas can be resistively loaded at the flare ends to reduce internal reflections. Other planar dipole antennas include elliptical, rectangular, and biconical dipoles which also achieve wider bandwidths than the standard dipole.

### 3.3.2 Horn Antennas

Horn antennas consist of a flaring metal waveguide shaped like a horn to direct electromagnetic waves in a beam (see Figure 3.8d). The gradual flare of the horn is to match the impedance of a waveguide (usually  $50 \Omega$ ) to the impedance of free space ( $377 \Omega$ ), which allows the antenna to radiate efficiently. Horn antennas usually have excellent gain, directivity, and sidelobe performance. Ultra-wide bandwidths can be achieved with dual ridge horns. The input impedance of a typical horn antenna varies slowly over a wide frequency range implying wideband  $S_{11}$  and VSWR performance. Horn antennas are usually made of aluminium, copper, or steel, making them heavy compared to planar PCB antennas. However, several studies have investigated the possibility of using lighter materials such as graphene-containing carbon composite materials [123] or 3D printed horn antennas coated in conductive paint, or metalized 3D prints [60, 69, 76].

### 3.3.3 End Fire Tapered Slot Antennas

End-fire tapered slot antennas can be regarded as a 2D horn antenna where the slot can be linearly or exponentially tapered. The exponentially tapered slot antenna is also known as the Vivaldi antenna, shown in Figure 3.8e. The Vivaldi antenna is typically known for its wide bandwidth, medium directivity, and long electrical length compared to its physical size due to the exponentially tapered shape of the slot. The basic Vivaldi antenna type can be modified to improve directivity, bandwidth, impedance matching, or size. Some of these

modifications are described in Section 5.1.

### 3.3.4 Spiral Antennas

The spiral antenna is arguably the antenna type most correctly classified as "frequency independent." Not surprisingly, the bandwidth is finite in practice due to the finite length of the antenna arms and finite inner gap width, as shown in Figure 3.8f. The maximum and minimum operating frequency of the spiral antenna is determined by the inner and outer diameter, respectively [48].

Antennas radiate specific frequencies from a region called the active region, where the currents add constructively for each frequency and produce coherent radiation. In the case of spiral antennas, when a wideband pulse is fed into the spiral antenna, the active region will propagate along the spiral arms, effectively deconstructing the pulse into its frequency components, creating a chirp. A de-chirping procedure in software reconstructs the pulse after reception. This is accomplished by correcting for the non-linear phase with a model of the change in the group delay of the antenna [23].

### 3.3.5 Array Antennas

Array antennas (see Figure 3.8g), often called phased-array antennas, is two or more spatially separated antennas. The signals from the antennas are combined in order to achieve improved performance compared to a single antenna. Antenna arrays have a plethora of uses. The most central purposes are to increase overall gain, "steer" the main lobe of the antenna, or determine the direction of an incoming wave.

The gain of antenna arrays can be significantly increased and even steered by controlling the phase delay of the signal to each radiating element.

### 3.4 Radar Waveforms

This section outlines the most used waveforms for GPR, with extra focus on pseudo random binary sequence (PRBS) waveforms since it is used in this project. Other waveforms not mentioned include polarization modulation and single (or dual) frequency methods. When choosing the waveform for a radar system, the radar sensing task and the full network of options should be considered. Figure 3.9 illustrates some of the choices that must be made, from the radar sensing task to the digital processing stage.

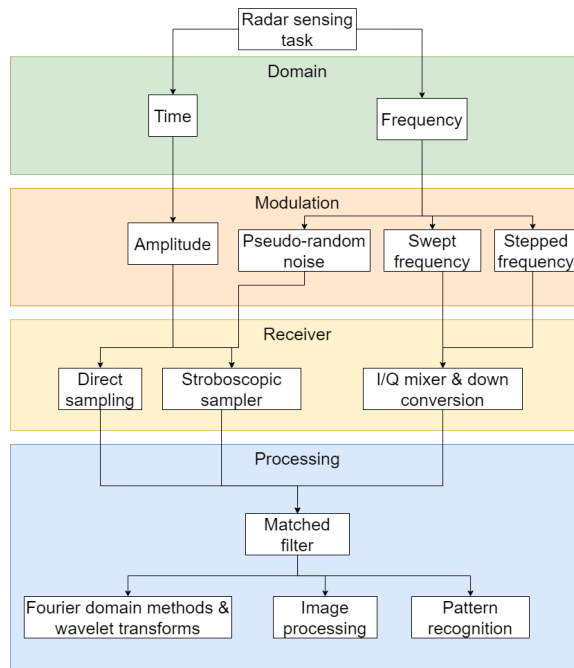


Figure 3.9: GPR system design options.

The operating frequency band of the radar system is also crucial for the radar sensing task, where different waveforms and antenna types allow for more or less flexibility in that regard.

#### 3.4.1 Amplitude Modulation/Impulse

Classical radar sensing tasks such as detection and ranging are usually accomplished by analyzing the impulse response of the scenery. Impulse radar directly measures the impulse response function (IRF) in the time domain using short pulses as the transmitted signal. The bandwidth of the system limits the measured IRF. The shorter the pulse, the wider the bandwidth. Sub-ns pulses are needed to produce ultra-wideband pulses [35]. There exist single-

shot oscilloscopes capable of real-time sampling of such pulses<sup>1</sup>; however, such systems are bulky and costly. Hence, real-time sampling is not often feasible in miniature radar systems. However, capturing one complete waveform over several subsequent impulse periods is possible using a fixed pulse repetition rate and stroboscopic sampling. With this method, only one (or a few) samples are taken for each generated pulse, and each sub-sample must be taken at a known offset from the impulse event. This method reduces the sampling rates down to the MHz to kHz range, making high-resolution analog-to-digital converter (ADC) possible. However, sub-sampling reduces the receiver efficiency as most of the transmitted power is ignored for each sub-sample, and hence, a longer time is needed to build a complete IRF. Also, the target and platform are assumed quasi-stationary during the sampling sequence. A general rule is that the translatory movement must not exceed the range resolution during the IRF acquisition [28].

Typical duty cycles of pulse radars are 1 % or even lower, which is a significant contrast to CW techniques that can go up to 100 %, implying that a large amount of energy needs to be put into a tiny portion of the whole signal period to maintain a good signal-to-noise ratio (SNR). This energy demand results in high maximum voltage pulses that both the transmit and receive electronics need to handle. Shielding of the other surrounding electronics is also more acute when using pulse radars.

### 3.4.2 Frequency Modulated Continuous Wave

Continuous-wave (CW) refers to sensors that use continuous signals (often looping signals) for their measurements. Single-frequency CW signals (i.e., sinusoidal) can detect doppler shift in the received signal to estimate the velocity of the target, but however, with no range information. Unless we consider interferometric measurements for simple targets [86]. Sweeping the signal frequency across a bandwidth (i.e., modulating the frequency) results in range resolution.

A frequency modulated continuous wave (FMCW) radar system transmits a signal with a continuously changing frequency using a linear voltage sweep controlling a voltage controlled oscillator (VCO), resulting in a frequency that sweeps across a chosen frequency band. The received signal is mixed with the transmitted waveform (in a given time instance), resulting in the difference in frequency between the instantaneous transmitted and received frequency, which is proportional to the target range.

1. For more information on single-shot oscilloscopes, visit: <https://www.keysight.com/en/pcx-x2015004/oscilloscopes?cc=NO&lc=eng&tab=x901106>

Note that this waveform still responds to doppler shift. Hence, doppler ambiguity is introduced when the target or radar platform is moving. This ambiguity is solved by sweeping the frequency in a triangular shape instead of a sawtooth shape.

### 3.4.3 Stepped Frequency/Vector Network Analysis

Network analyzers are devices used to characterize electrical networks. The network analyzer uses input and output ports to connect to the device under test and measures transmission and reflection between the ports and device. The operation of a vector network analyser (VNA) is similar to FMCW; however, the frequency is changed in discrete steps allowing for settling time for each single frequency sine wave. Suppose antennas are connected to the test ports of a VNA. In that case, it will gather the frequency domain IRF of the antenna aperture, easily converted to time-domain IRF with the Fourier transform, given that the frequency steps are constant across the bandwidth.

Stepped frequency is also used for dedicated radar sensors such as in [80]. This waveform proves to be excellent for radar sensing tasks and is highly configurable in terms of frequency range and number of steps, which defines the unambiguous range. One drawback is the settling time for each frequency step in the order of tens of  $\mu s$ , limiting the measurement rate (IRF/s).

### 3.4.4 Noise Modulated; M-Sequence

Noise modulated signals provide good possibilities for GPR systems. The receiver is less susceptible to interference, and the radiated power is evenly spread throughout the spectrum. As with the other CW methods mentioned, this poses a considerable advantage over impulse waveforms as the transmitted energy can be spread out equally in time, increasing the duty-cycle and reducing the signal peak power. This reduction in instantaneous signal level leads to low-cost RF circuit integration [97]. Further, non-linear distortion will also be reduced for active components compared to pulse excitation due to the low peak power [89]. If real noise is used as a stimulus (i.e., the transmitted signal is not periodic), the received signal must be sampled and correlated with the transmitted signal.

A different approach to noise modulated waveform generation is pseudo-noise waveforms. These waveforms are periodic and hence not strictly random. However, the waveform has properties similar to random signals, such as a pulse-like auto-correlation function (ACF). Such signals can also cover large bandwidths, and sub-sampling can easily be applied due to their periodic nature.

For pseudo-noise waveforms, the transmitted signal does not need mixing with the incoming signal since correlation calculation is performed with a stored digital representation of the known signal. This being a coherent signal, most interference is canceled through the correlation (i.e., match filtering).

A maximum length binary sequence, or in short an M-sequence is a type of PRBS in the family of pseudo noise signals. The description pseudo random is used since the signal is periodic and hence not strictly random. However, the waveform has properties similar to random signals such as a pulse-like autocorrelation function  $R_{xx}(\tau)$ :

$$R_{xx}(\tau) = \frac{1}{T} \int_T x(t)x(t+\tau)d\tau \approx \delta(\tau) \quad , \quad (3.22)$$

where  $x(t)$  is the M-sequence signal, and  $T$  is the period of one sequence.

A signal having a short autocorrelation function has, in turn, a large bandwidth and can, in principle, be used as a stimulus for UWB radar imaging. However, the raw backscattered signal  $y(t)$  is not particularly useful for radar imaging. The cross-correlation function  $R_{yx}(\tau)$  representing the cross-correlation between the transmitted and backscattered signal contains more interesting information:

$$R_{yx}(\tau) = \frac{1}{T} \int_T y(t)x(t+\tau)d\tau \quad . \quad (3.23)$$

The interesting information lies in the impulse response  $h(t)$  between the transmitting and receiving antennas which contain the scattering behaviour of targets within the aperture of the antennas. The impulse response is related to  $R_{yx}(\tau)$  and  $R_{xx}(\tau)$  by a convolution [14]:

$$R_{yx}(\tau) = h(\tau) \otimes R_{xx}(\tau) \quad . \quad (3.24)$$

If the autocorrelation function  $R_{xx}(\tau)$  is a Dirac pulse  $\delta(\tau)$  (i.e., infinite bandwidth), Equation (3.23) simplifies to:

$$R_{yx}(\tau) \propto h(\tau) \quad . \quad (3.25)$$

Equation (3.25) states that the cross-correlation function between the received

and transmitted signal is proportional to the impulse response function as long as the autocorrelation function of the transmitted signal is narrow compared to the actual impulse response function of the target.

The basic concept of signal generation is to produce a binary sequence from a fast shift register controlled by a constant frequency oscillator/clock. The constant frequency oscillator results in a more stable system time-base compared to waveforms that require a changing frequency (e.g., sweeping oscillator, VCO).

Since this is the waveform used in this thesis, more attention is given to its parameters in the next section.

### 3.4.5 M-Sequence Parameters

An M-sequence is a binary signal generated by a digital shift register, where the number of flipflops  $m$  in the register defines the order of the pseudo-random code [26]. The master clock frequency  $f_c$  activates the shift registry and generates a pseudo-random sequence of logical values (0 or 1), visualized as a sequence of rectangular pulses of varying width and spacing.

The total length (in 'chips' or range bins) of such a sequence is defined as:

$$N = 2^m - 1 \quad , \quad (3.26)$$

where each element have a period  $T_0$  of:

$$T_0 = \frac{1}{f_c} \quad . \quad (3.27)$$

To generate the pseudo-random sequence from the shift register, "XOR" feedback loops are used with coefficients ("a" in Figure 3.10) set to a chosen logical value. The values of the coefficients are what defines the sequence [26].

The duration of a full sequence is the inverse of the measurement rate (equivalent to pulse repetition frequency or IRF/s):

$$T_p = NT_0 = \frac{1}{IRF/s} \quad . \quad (3.28)$$



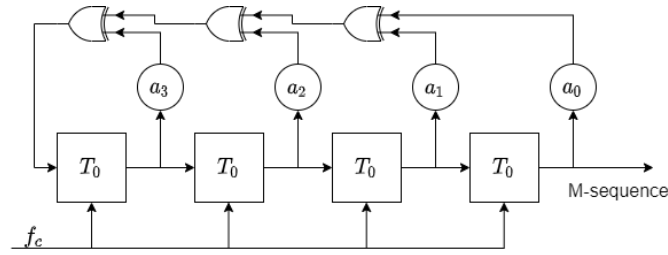


**Figure 3.10:** 4-th order M-sequence generator example.

The unambiguous range in a given non-magnetic medium for an M-sequence radar  $R_0$  can be expressed as [14]:

$$R_0 = \frac{\frac{c}{\sqrt{\epsilon_r}}(2^m - 1)}{2f_c} \quad , \quad (3.29)$$

where  $c$  is the propagation velocity in free space,  $\epsilon_r$  is the relative permittivity of the medium,  $m$  is the order of the M-sequence shift register, and  $f_c$  is the clock frequency.

The bandwidth of the signal can with some simplification be related to one parameter, the master clock frequency  $f_c$  [14]:

$$B \approx \frac{f_c}{2} \quad [\text{Hz}] \quad . \quad (3.30)$$

The M-sequence has a short auto-correlation function resulting in a flat spectrum over a broad bandwidth. The sidelobes of the autocorrelation function largely depend on the sequence length, where the sidelobes decrease with increasing shift registry length. The longer the sequence, the more similar it is to real noise (see Figure 3.11). The length of the shift registry also affects the unambiguous range of the radar as each bit represents a range bin (from Equation (3.26)) in the processed scan. A registry length of  $m = 9$ , translates to 5.75 m unambiguous range in air, based on Equation (3.29).

The most suitable commercial radar hardware for pseudo-noise signal generation was found to be the ILMsens m:explore transceiver system<sup>2</sup>. 9 and 12 order versions have been used in this project.

The basic concept of signal generation and reception is described in Figure 3.12.

2. Visit the ILMsens website at: <https://www.uwb-shop.com/products/m-explore/>

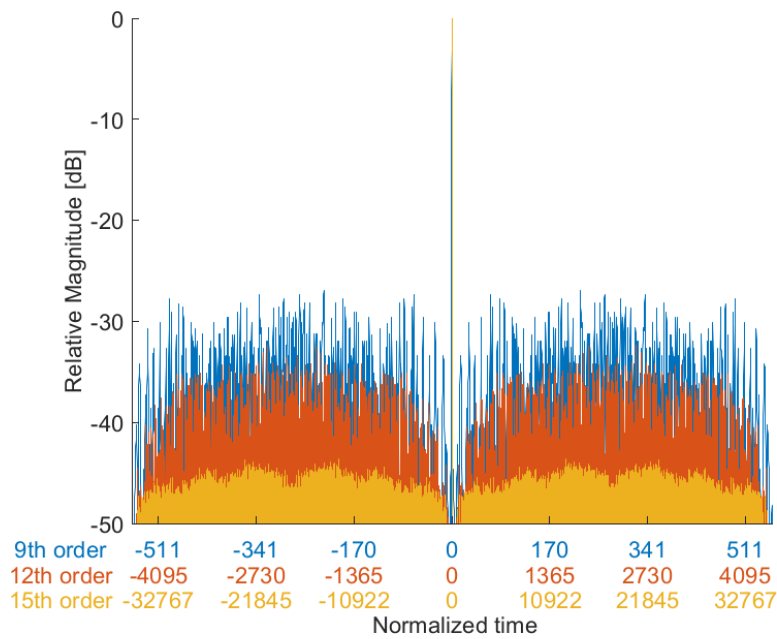


**Figure 3.11:** Match filter output for 9th (blue), 12th (red), and 15th (yellow) order shift registers. The time axis is normalized with respect to the register bit lengths. The unit is, therefore, in bits.

The M-sequence generator (Figure 3.10) is driven by a stable clock source with frequency  $f_c$ . The stability of the clock frequency is critical to the performance of the sensor, as it defines the maximum bandwidth (Equation (3.30)), unambiguous range (Equation (3.29)), and penetration depth shown in Section 4.2. The M-sequence signal is then filtered by an anti-aliasing filter set at  $f_c/2$ , amplified, and transmitted by the antenna.

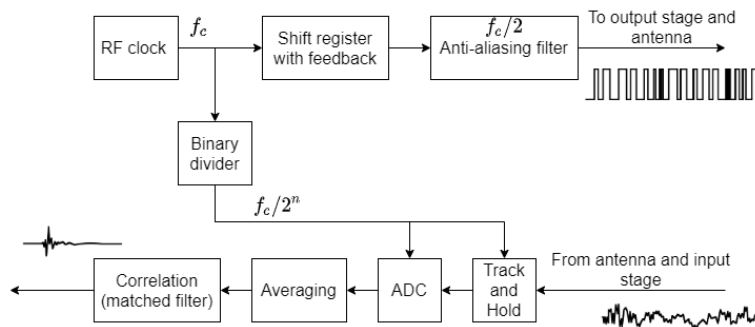


**Figure 3.12:** Basic concept block diagram of an M-sequence transceiver.

Stroboscopic sampling is accomplished using a binary divider to control a track & hold (T&H) ADC. A T&H ADC captures the voltage and holds its value at a constant level for a specified time, in this case controlled by the binary divider

(see Figure 3.12). Hence, exploiting the periodicity of the signal. The signal is sampled at a frequency  $f_c/2^n$  where typical values for  $n$  are in the range of 32 to 256. Consequently, the IRF is measured across several M-sequence periods. Additionally, the receiver has built-in averaging to increase SNR. Finally, the sampled signal is correlated with the stored sequence employing Equation (3.23) in the Fourier domain for computational speed.



# /4

## Remote Sensing of Snow

This chapter introduces snow as a physical medium together with its electromagnetic properties. A description of how radar waves respond to this medium is presented, and finally, methods to estimate snow properties with such waves.

### 4.1 Snow Parameters

Snow can generally be considered as a medium of randomly scattered ice particles suspended in a background medium, which, in the case of dry snow, is air [109]. However, the complexity of snow increases with the introduction of compounds like liquid water (i.e., wet snow) and salinity (e.g., snow on sea ice).

There are several different macrophysical properties used to describe snow, and some are measured more often than others, due to both their significance or ease of attainability. Some properties also have significant error margins, even with the most modern sensors available today.

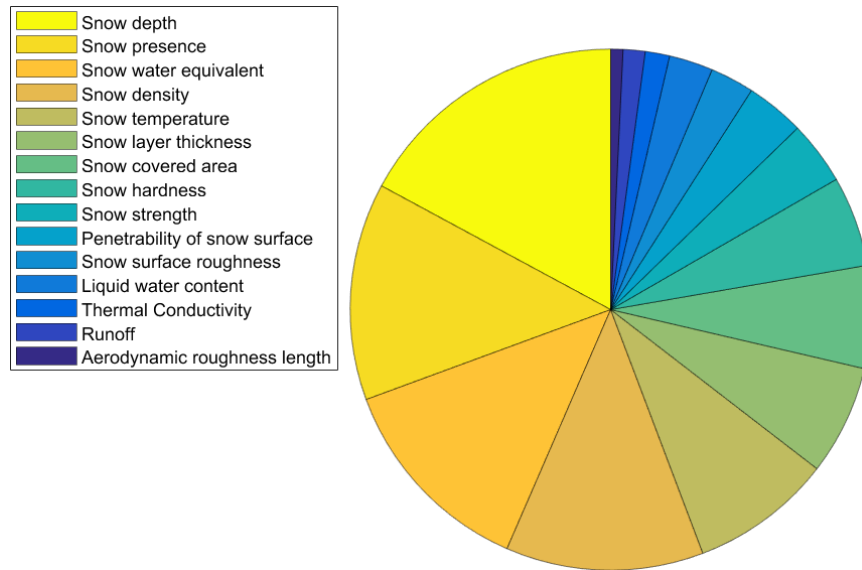


**Figure 4.1:** Snow properties frequency of measurement. Adopted from [87].

Figure 4.1 shows a selection of snow properties and the sampled frequency of measurement according to [87], for which snow depth, presence (binary), snow water equivalent (SWE) and density are the most frequently measured parameters; primarily due to the wide variety of applications where these are involved. Additionally, these parameters are also relatively easy to obtain with low confidence intervals compared to, e.g., liquid water content.

The most common microphysical properties recorded are grain shape and size [87], often for research purposes and avalanche risk assessment. Table 4.1 lists the definition of central snow parameters gathered from [87] and [24].

As stated in Table 4.1, SWE is the resulting depth of water from a completely melted mass of snow. SWE is typically expressed in millimeters of equivalent water, which is equivalent to kilograms per square meter or liters per square meter, thus referring to the unit surface area of the considered snow sample [24].

The SWE can be expressed as the product of the snow depth in meters and the vertically-integrated density in kilograms per cubic meter:

$$\text{SWE} = d_s \rho_s \quad [\text{kg/m}^2] \quad . \quad (4.1)$$

**Table 4.1:** List of selected measurable snow properties from [87] and [24]

Parameter	Definition
Snow depth	Snow depth denotes the total height of the snowpack (i.e., the vertical distance in centimeters from base to snow surface). Unless otherwise specified, snow depth is related to a single location at a given time. Thus, the manual snow depth measurements are often made with one or more fixed snow stakes. On the other hand, portable snow depth probes allow for measurements along with snow courses and transects. The slope-perpendicular equivalent of the snow depth is the total thickness of the snowpack.
Snow density	Density, that is, mass per unit volume ( $\text{kg}/\text{m}^3$ ), is normally determined by weighing snow of a known volume. Sometimes total and dry snow densities are measured separately. Total snow density encompasses all of the constituents of snow (ice, liquid water, and air), while the dry snow density refers to the ice matrix and air only.
Snow water equivalent	Snow water equivalent (SWE) is the vertical depth of water that would be obtained if the snow cover melted completely, which equates to the snow-cover mass per unit area.
Liquid water content	Liquid water content (LWC) is defined as the amount of water within the snow that is in the liquid phase. This parameter is synonymous with the free-water content of a snow sample.
Snow hardness	Hardness is the resistance to penetration of an object into the snow. Hardness measurements produce a relative information value that depends on the instrument. Therefore, the device has to be specified.
Stratigraphy	The snow layer thickness, or stratigraphy, (measured in centimeters or fractions thereof) is an essential parameter when characterizing the current state of a snowpack. Layer thickness is usually measured vertically.
Presence of snow	A binary observation of the presence of snow cover at the measurement location, usually based on a snow cover fraction threshold of 50%.

Snow density  $\rho_s$  can be crudely modeled as a function of snow depth  $d_s$  given a certain region and time of year [31]:

$$\rho_s = 352 + 75 \ln(d_s) \quad [\text{g/cm}^3] \quad . \quad (4.2)$$

Alternatively, by combining several more parameters such as: elevation above sea level  $E$ , degree days  $D_d$  when  $T > 0^\circ\text{C}$  and wind days  $D_w$  when  $T > 0^\circ\text{C}$  and wind speed  $W > 2 \text{ m/s}$ , Bruland et al., [8] present a more complex model that is here adapted to model snow density as:

$$\rho_s = 0.324(1 - e^{(-50d_s - 1.8E - 4.7D_d - 4.2D_w)10^{-4}}) + 0.148 \quad [\text{g/cm}^3] \quad . \quad (4.3)$$

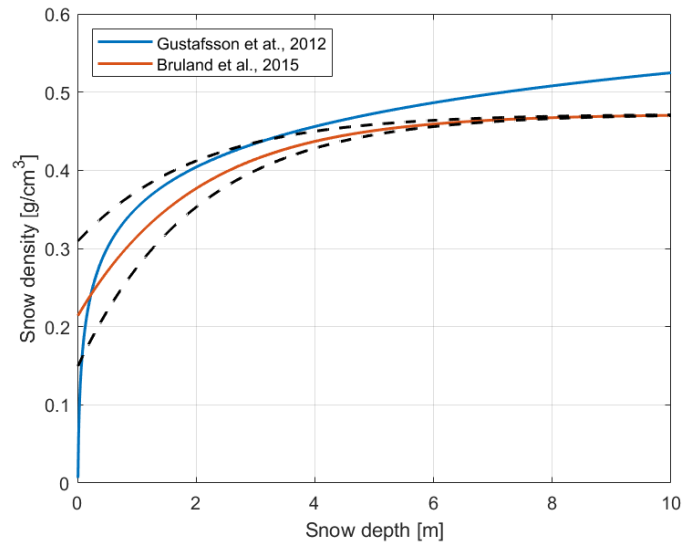


**Figure 4.2:** Snow density modeled as a function of depth with two different models, from Equations (4.2) and (4.3). Dashed lines indicate the range of the model in Equation (4.3) with typical values for the additional parameters.

Figure 4.2 compares the two models in Equations (4.2) and (4.3), where the black lines indicate the upper and lower range of the model in Equation (4.3) with typical values for the additional parameters. Notice that the two lines collapse to one line with increasing snow depth, implying that the additional parameters introduced in Equation (4.3) become less influential as the snow depth increases.



## 4.2 Scattering Characteristics of Snow

The backscattered signal from snow is a function of snow density, snow particle diameter, surface roughness, temperature, conductivity, and liquid water content (LWC), as well as electromagnetic (EM) wave parameters such as frequency, polarization, and incidence angle. In general, snow is electromagnetically a three-component dielectric mixture of air, ice particles, and liquid water [33].

In radar sensing tasks of snow, the frequency-dependent complex relative dielectric constant is arguably the most central parameter. It governs the attenuation in the medium, which is the primary constraint to penetration depth. Furthermore, a reasonably accurate estimate of the complex relative dielectric constant can be used to estimate snow density and LWC.

EM wave propagation can from Maxwell's equations be represented by a one dimensional (1D) plane wave equation with propagation along the z-axis [14]:

$$\frac{\partial^2 \mathbf{E}}{\partial z^2} = \frac{1}{v^2} \frac{\partial^2 \mathbf{E}}{\partial t^2} \quad , \quad (4.4)$$

where the velocity of propagation  $v$  is a function of the absolute magnetic permeability and electric permittivity:

$$v = \frac{1}{\sqrt{\mu_0 \mu_r \epsilon_0 \epsilon_r}} = \frac{1}{\sqrt{\mu \epsilon}} \quad [\text{ms}^{-1}] \quad , \quad (4.5)$$

and the velocity in free space is:

$$c = \frac{1}{\sqrt{\mu_0 \epsilon_0}} \quad [\text{ms}^{-1}] \quad . \quad (4.6)$$

These equations include:

The absolute magnetic permeability of free space:  $\mu_0 = 1.26e^{-6} [\text{Hm}^{-1}]$ .

The absolute electric permittivity of free space:  $\epsilon_0 = 8.86e^{-12} [\text{Fm}^{-1}]$ .

The complex relative permittivity:  $\epsilon_r = \frac{\epsilon}{\epsilon_0}$

The complex relative permeability:  $\mu_r = \frac{\mu}{\mu_0}$

The relative permeability is 1 for nonmagnetic geologic materials. Hence, the propagation velocity in a given medium is simplified to:

$$v_r = \frac{c}{\sqrt{\epsilon_r}} \quad [\text{ms}^{-1}] \quad , \quad (4.7)$$

where  $\epsilon_r$  is frequency-dependent and can vary along the propagation axis for heterogeneous materials.

The relative permittivity, also called the dielectric constant of a material, could be viewed as the ratio of capacitance in a capacitor using that material as a dielectric, compared to a capacitor with the same dimensions that has vacuum as its dielectric. The relative permittivity is a dimensionless complex number and may be expressed as:

$$\epsilon_r = \epsilon'_r + j\epsilon''_r \quad . \quad (4.8)$$

The conductivity in the material  $\sigma$  is also a complex number in Siemens per meter [S/m]:

$$\sigma = \sigma' + j\sigma'' \quad [\text{S/m}] \quad . \quad (4.9)$$

From Equations (4.8) and (4.9), the real and imaginary terms can be described as:

$\epsilon'_r$  is the dielectric polarisation term, referring to induced polarization in the material.

$\epsilon''_r$  represents the energy loss due to the polarisation lag causing scattering and ultimately heat from the mechanical coupling between atoms and induced dipole radiation in the material.

$\sigma'$  refers to Ohmic conduction, as in the relationship between the magnitude of current density and electric field.

$\sigma''$  is related to Faradic diffusion, or phase lag between the electric field and current density. I.e.,  $\sigma''$  describes the slowness in charge carriers response to a changing electric field.

The real part of the conductivity of snow  $\sigma'$  is usually small, and has been measured in the range of  $1 \times 10^{-4}$  to 0.01 mS/m [14, 29].

When  $\sigma$  is small, which is the case for snow, the ratio of the imaginary and real parts of the complex permittivity is a dimensionless factor commonly named the material loss tangent [103]:

$$\tan \delta = \frac{\epsilon''}{\epsilon'} \quad . \quad (4.10)$$

The velocity of propagation  $v_r$  is also reduced by an increase of the loss tangent in addition to the relative dielectric constant [14]. However,  $\tan \delta$  must be significantly greater than 1 for any slowing to occur, and it is reasonable to assume that for snow  $\tan \delta < 1$ . Hence, Equation (4.7) holds.

The amplitude of an electromagnetic field  $E_0$  starting at  $t = 0$  and  $z = 0$  in a conducting dielectric can be described by a solution to the plane wave Equation (4.4) [14]:

$$E(z, t) = E_0 e^{-\alpha z} e^{j(\omega t - \beta z)} \quad , \quad (4.11)$$

where the field is propagating in the  $z$ -direction,  $t$  is time,  $\omega = 2\pi f$  is the angular frequency,  $\alpha$  and  $\beta$  are the attenuation and phase constant, respectively. The first exponential term describes the attenuation, while the second describes the propagation of the wave.  $\alpha$  and  $\beta$  represent the complex components of the wavenumber.

The attenuation and phase constant can be expressed in terms of frequency, permittivity and permeability as:

$$\alpha = \omega \left( \frac{\mu \epsilon'}{2} \left( \left[ 1 + \left( \frac{\epsilon''}{\epsilon'} \right)^2 \right]^{\frac{1}{2}} - 1 \right) \right)^{\frac{1}{2}} \quad , \quad (4.12)$$

$$\beta = \omega \left( \frac{\mu \epsilon'}{2} \left( \left[ 1 + \left( \frac{\epsilon''}{\epsilon'} \right)^2 \right]^{\frac{1}{2}} + 1 \right) \right)^{\frac{1}{2}} \quad . \quad (4.13)$$

The attenuation constant can be expressed in dB/m and its inverse is denoted

as the skin depth  $\delta$ :

$$\delta = \frac{1}{\alpha} \quad , \quad (4.14)$$

also called penetration depth.

Penetration depth is defined as the depth (or distance) a plane wave has to travel for the amplitude to reduce to  $1/e$  (or 37 %) of the transmitted value. This depth is used to describe how "lossy" a medium is and limitations regarding radar depth probing. However, it should be noted that this definition of penetration depth only takes into account attenuation, ignoring scattering losses. Hence, in reality,  $\delta$  is lower because of scattering losses.

The penetration depth  $\delta$  in materials with relative magnetic permeability  $\mu_r$  approximated to 1, such as snow or ice, can be re-written in terms of the relative permittivity  $\epsilon_r$  as [18, 110]:

$$\delta = \frac{\lambda_0}{4\pi} \left( \frac{\epsilon_r'}{2} \left( \left[ 1 + \left( \frac{\epsilon_r''}{\epsilon_r'} \right)^2 \right]^{\frac{1}{2}} - 1 \right) \right)^{-\frac{1}{2}} \quad , \quad (4.15)$$

where  $\lambda_0 = \frac{c}{f}$  is the wavelength in free space.

Consequently, the loss in the medium can be expressed as:

$$L = 10 \log(e^{\frac{1}{\delta}}) \quad [\text{dB/m}] \quad . \quad (4.16)$$

If  $\tan \delta \ll 1$ , which usually is the case for dry snow, Equation (4.15) is simplified to:

$$\delta \approx \frac{\lambda_0 \sqrt{\epsilon_r'}}{2\pi \epsilon_r''} \quad . \quad (4.17)$$

In the microwave region,  $\tan \delta$  is in the order of  $10^{-2}$  to  $10^{-3}$  for snow [110].

Since  $\epsilon_r''$  of water is several orders of magnitude larger than that of dry snow, Equation (4.17) states that even minimal amounts of liquid water in the snow-

pack can dramatically decrease the penetration depth  $\delta$ . Furthermore, the penetration depth also decreases as a function of frequency, which will decrease for liquid water up to the relaxation frequency of water (10 to 20 GHz) [34].

To determine the penetration depth in homogeneous and isotropic materials, the relative complex dielectric constant from Equation (4.8), must be known. The value of  $\epsilon_r$  depends on several snow state variables. Predicting the microwave response can be complicated due to the depth gradient of liquid water content or salinity concentration within the snowpack.

The relation between snow dielectric and density has been modeled both theoretically [109] and empirically [108]. Several empirical models relate both dry and wet snow to the relative dielectric constant. If we assume the liquid water (and salinity) content to be negligible, then the dielectric constant is real-valued and solely dependent on density.

The dielectric constant of snow can be written as [108]:

$$\epsilon'_r = 1 + 1.7\rho_s + 0.7\rho_s^2 \quad , \quad (4.18)$$

where  $\epsilon'_r$  is the real part of the relative dielectric constant and  $\rho_s$  is the density of the snow in  $\text{g}/\text{cm}^3$ .

Considering dry snow with density below  $0.5 \text{ g cm}^{-3}$ , which is often the case in nature, a linear relationship gives an acceptable approximation [108]:

$$\epsilon'_r = 1 + 2\rho_s \quad . \quad (4.19)$$

Regarding snow containing significant amounts of liquid water (approximately from 2% up to 10%), the real part of the dielectric constant can be calculated as [108]:

$$\epsilon'_r = 1 + 1.7\rho_s + 0.7\rho_s^2 + 8.7W_u + 70W_u^2 \quad , \quad (4.20)$$

where  $W_u$  is the wetness by volume fraction.

The liquid water content also contributes to the imaginary part of the permittivity to the point where it is not negligible. The imaginary part of the permittivity

can be calculated by [108]:

$$\epsilon_r'' = 0.9W + 7.5W^2 \quad . \quad (4.21)$$

As previously stated, the complex dielectric constant of snow and ice can be estimated using both empirical and theoretical models for the real and imaginary parts. Figure 4.3 shows a comparison of selected models used to calculate penetration depth. The models were collected from: [33, 39, 40, 72, 73, 79, 108, 109]. The Strong fluctuation model for dry Snow [109] treats snow as a medium of randomly scattered ice particles suspended in a background medium, which, in the case of snow, is air. This model takes into account grain size, which further decreases the penetration depth for high frequencies (> 5 GHz). As frequency or snow density increases, the model diverges from the empirical models.

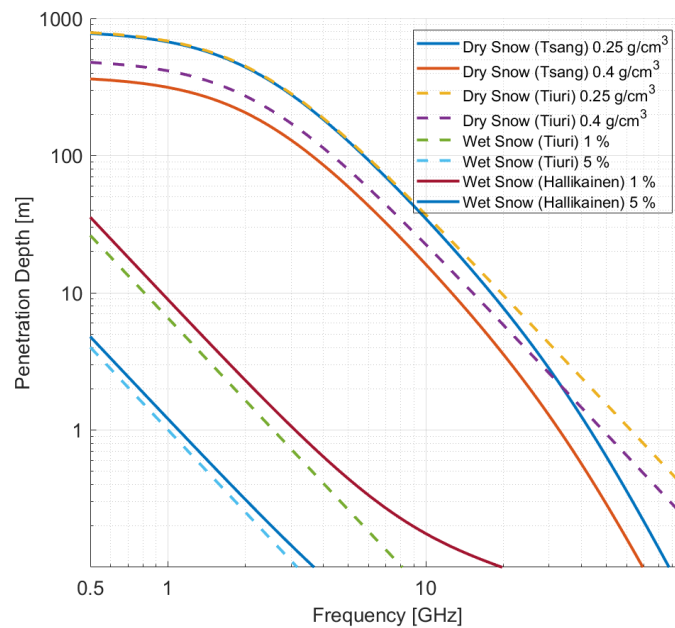


**Figure 4.3:** Penetration depth at a temperature of 268 K shown as a function of frequency for dry snow with 0.5 mm grain size and wet snow with a dry snow density of  $0.4 \text{ g/cm}^3$ . Both snow types (wet and dry) are calculated with two different models, where the main difference is that the Tsang model accounts for grain size.

### 4.3 Characterizing Snow with UWB Radar

The use of EM waves to extract snow state parameters are widespread with several different wave-forms, platforms, and processing methods [13, 30, 66] (see also Chapter 2). Common to all techniques are the effects a layered medium has on propagating microwaves. In this section, we will look at some methods to measure snow depth and density from ground penetrating radar (GPR).

Snow depth is usually measured by evaluating the two way travel time (TWT) (denoted as  $t$ ) from the snow surface to the ground and calculating the distance traveled with an estimate of the propagation velocity.

For homogeneous and isotropic materials, the relative propagation velocity  $v_r$  is related to the relative dielectric constant  $\epsilon_r$  as in Equation (4.7):

$$v_r = \frac{c}{\sqrt{\epsilon_r}} \quad [\text{ms}^{-1}] \quad (4.22)$$

where  $c$  is the propagation velocity in free space. The depth  $d$  is then:

$$d = v_r \frac{t}{2} \quad [\text{m}]. \quad (4.23)$$

These equations give important information about GPR measurements in snow. That is, we need the dielectric constant to estimate the depth in the medium. Hence, GPR measured snow depth contains all the information to estimate SWE, since there is a relation between the dielectric constant and snow density as stated in Equations (4.18) and (4.20). In the same way, extracting the propagation velocity from radar data enables calculation of the real part of the relative dielectric constant.

Consider a point target buried in the medium under examination. Moving the radar laterally across the target will create a hyperbolic spreading function as in Figure 4.4. The relationship between the propagation velocity  $v_r$  and the hyperbolic spreading function can be written as [14]:

$$v_r = 2 \sqrt{\frac{x_{n-1}^2 - x_0^2}{t_{n-1}^2 - t_0^2}}, \quad (4.24)$$

where  $x$  and  $t$  denotes the position of the radar (slow-time) and the time to each reflection (fast-time), respectively.

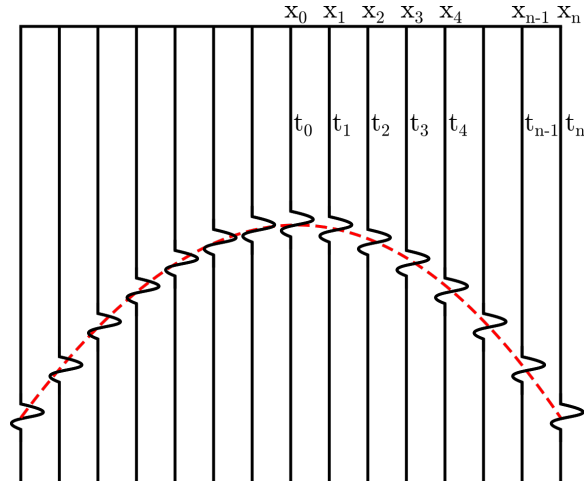


**Figure 4.4:** Constellation of A-scans from hyperbolic spreading function.

There are several different methods to extract the propagation velocity from the hyperbolic spreading function. Paper III discusses various techniques and presents a scheme using migration velocity analysis (MVA) to determine the average radar wave velocity. F-K migration is a commonly used migration method to focus the radar data for a fixed velocity. An estimate of the average propagation velocity is found by running the migration for several test velocities and calculating the degree of focusing with auto-focusing metrics. The actual propagation velocity in the snow is then calculated using Dix's equation for a layered velocity model.

For an  $m \times n$  migrated image  $s(x, y)_{v_t}$  at test velocity  $v_t$ , the degree of focusing can be calculated using several different autofocusing expressions [117].

Since the apex of the hyperbolas should have a maximum at the correct propagation velocity, the average image intensity for each test velocity  $v_t$  can be calculated to evaluate the focusing:

$$AI(v_t) = \frac{\sum_{i=1}^m \sum_{j=1}^n |s(x_i, y_j)_{v_t}|^k}{[\sum_{i=1}^m \sum_{j=1}^n |s(x_i, y_j)_{v_t}|]^k}, \quad (4.25)$$

where  $k \in [2, 4]$  and  $v$  is the migration velocity.

However, this metric has poor performance for increasing signal-to-noise ratio (SNR) [117]. Therefore, a higher order technique should be used that involves



the variance of the migrated image:

$$AH(v_t) = \frac{\sum_{i=1}^m \sum_{j=1}^n [|s(x_i, y_i)_{v_t}| - \hat{\mu}]^k}{(mn - 1)\hat{\sigma}^k} , \quad (4.26)$$

where  $k \geq 1$ ,  $\hat{\mu}$  and  $\hat{\sigma}$  are the mean and variance of the migrated data. In [116], a  $k$  value of 10 was found to be optimal. This autofocusing metric was used in Paper III.

The best fit velocity  $v_{rms}$  represents the average bulk velocity from the antennas to the ground. Hence, to remove the influence of the air section down to the snow surface and calculate the average propagation velocity in the snow  $v_s$ , we use the Dix equation [15]:

$$v_s = \sqrt{\frac{v_{rms}^2 t_{tot} - v_{air}^2 t_{air}}{t_{tot} - t_{air}}} , \quad (4.27)$$

where  $t_{tot}$  is the total TWT in the data,  $t_{air}$  is the TWT of the air section and  $v_{air}$  is the approximate propagation velocity in the atmosphere (i.e., approximately 0.2997 m/ns).

Evaluating Equation (4.27), we see that if  $t_{air}$  increases towards  $t_{tot}$ , then a small change in  $v_{rms}$  will result in a large change in  $v_s$ .

In other words, the demand for accuracy of  $v_{rms}$  estimation increases with an increasing fraction of air compared to the total length of the radar scene.

### 4.3.1 Case study: Dix Equation Velocity Estimation Uncertainty

Let us consider a case with a constant snow depth of 2 m, and for different altitudes above the snow we calculate the uncertainty of the velocity estimate. The uncertainty in the calculated interval velocity  $\Delta v_I$  can be found by [32]:

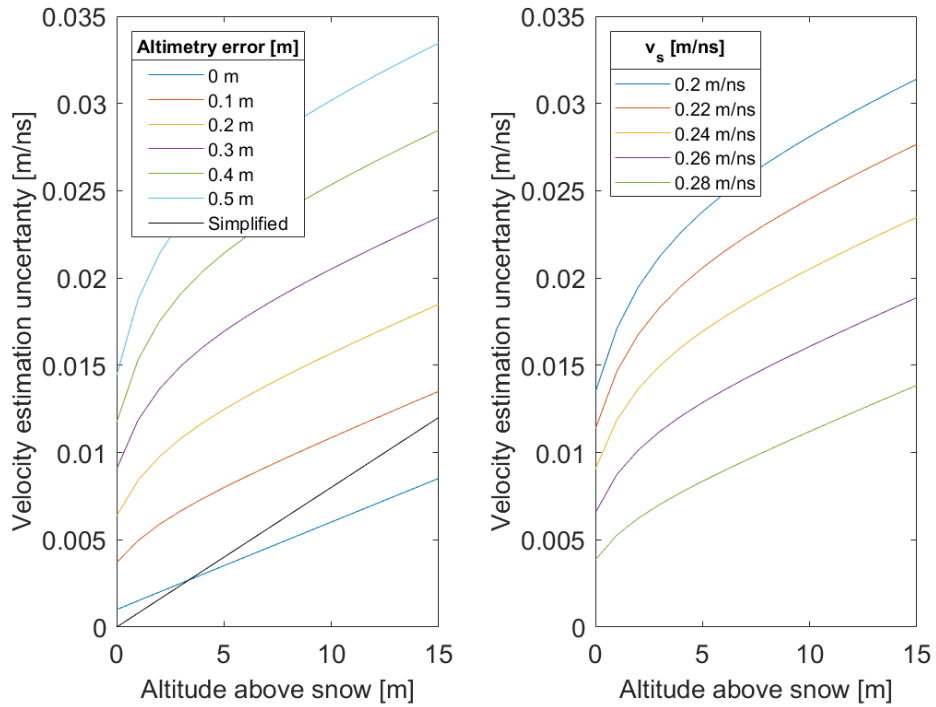
$$\Delta v_I = \left(\frac{1}{ac}\right)^{\frac{1}{2}} [v_{rms} t_{tot} |\Delta v_{rms}| + v_{air} t_{air} |\Delta v_{air}|] + \frac{1}{2} \left(\frac{b^2}{a^3 c}\right)^{\frac{1}{2}} [t_{tot} |\Delta t_{air}| + t_{air} |\Delta t_{tot}|] , \quad (4.28)$$

where  $\Delta v_{rms}$ ,  $\Delta v_{air}$ ,  $\Delta t_{tot}$  and  $\Delta t_{air}$  is the error in the velocities and incidence times, respectively, and:

$$\begin{aligned} a &= t_{tot} - t_{air} \quad , \\ b &= v_{rms}^2 - v_{air}^2 \quad , \\ c &= t_{tot}v_{rms}^2 - t_{air}v_{air}^2 \quad . \end{aligned}$$

A set of assumptions can greatly simplify this relatively complex equation. Assuming the layers are thin compared to the total depth, the velocity contrast is small which result in a constant error in  $v_{rms}$ . A simplified version of Equation (4.28) is presented in [32]:

$$\Delta v_I \approx \frac{2t_{air}}{a} \Delta v_{air} \quad . \quad (4.29)$$



(a) Constant propagation velocity (0.24 m/ns). (b) Constant altimetry error (0.3 m).

**Figure 4.5:** Dix's equation uncertainty as a function of altitude above snow, for altimetry errors (a) and different propagation velocities (b).

Figure 4.5a shows the uncertainty in Dix's equation with a constant  $\Delta v_{rms}$  of 0.001 m/ns,  $\Delta v_{air} = 0$  and a set of errors in the incidence times converted to distance. In practice, the incidence time error represents errors from the altimetric sensor determining the altitude above the snow as well as errors from the detection of the snow surface.

Similarly, evaluating the same uncertainty model with a fixed altimetry error of 0.3 m and allowing the propagation velocity in the snow to change, also results in a varying uncertainty. This is equivalent to evaluating the uncertainty for different snow densities (see Equation (4.18-4.21)). Figure 4.5b demonstrates that the uncertainty in Dix's equation also depends on the propagation velocity in the medium of interest. Consequently, the demand for accurate estimations of  $v_{rms}$  increases with altitude, altimetry errors, and snow density.

Figure 4.5 underlines that the altitude above the snow plays a crucial part in the accuracy of the velocity estimate. Hence, the altitude above the snow surface should be as small as practically possible for this estimation technique.



# /5

## Radar System Development

This chapter describes the radar system as of today, and some of the developments and improvements that were implemented throughout the project. The chapter is divided into three parts describing the development of each central part of the radar system, and finally, the current system is presented. The complete radar system has been named Ultra Wideband Snow Sounder or abbreviated, UWiBaSS.

### 5.1 Antenna Development

It could be argued that the most crucial part of any radar system is the antennas. The antennas for the ultra-wideband snow sounder (UWiBaSS) have gone through several improvements and adaptations for different applications since the first version during the author's master thesis work.

For an "air-launched" ground penetrating radar (GPR), a directional antenna is a key factor, which is not necessarily straightforward to achieve while retaining ultra wide-band (UWB) characteristics. The main design parameters and attributes are listed as in table 5.1. However, the combination of these parameters are difficult to achieve completely.

For all antenna design processes, a central aspect is that if one attribute is improved, usually it is at the cost of another. Hence, it is generally a compro-

**Table 5.1:** Antenna design parameters.

Attribute	Desired value
Bandwidth	0.1 to 6 GHz
Antenna Gain	> 10 dBi
Return Loss	< -10 dB across BW
Weight	< 1 kg
Drag (aerodynamics)	As low as possible
Water and icing proof	Yes
Mechanical stability	Low vibration during flight
Size	As small as possible

mise between the design parameters that eventually ends up as the realized antenna.

With these design parameters in mind, several different antenna types are eligible for investigation where each antenna has its pros and cons.

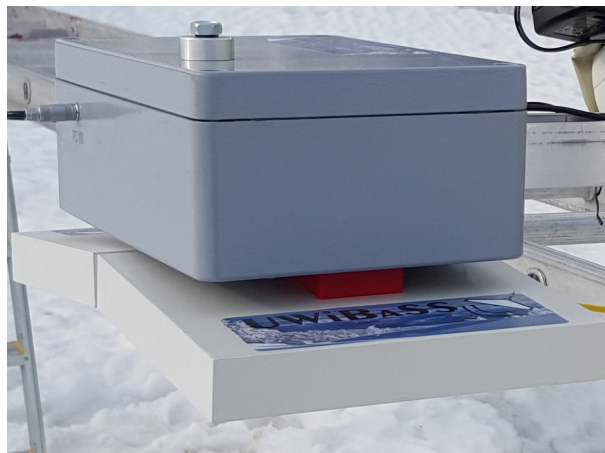
**Spiral Antenna: Pros;** good impedance matching across a large bandwidth and planar mounting resulting in low drag. **Cons;** low directivity, chirp impulse response, and bidirectional. Hence, needs cavity backing.

**Patch Antenna: Pros;** low weight, size and drag. Easy to manufacture. **Cons;** low directivity and bandwidth.

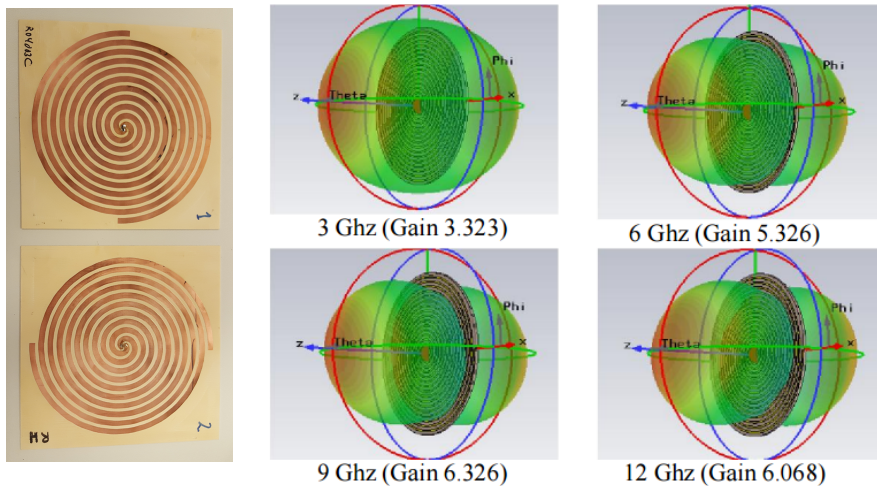
**Horn Antenna: Pros;** excellent directivity and bandwidth. **Cons;** high weight and drag.

**Vivaldi Antenna: Pros;** good directivity and bandwidth, low weight and drag. Easy to manufacture. **Cons;** prone to vibration and reduced directivity in H-plane.

The first antennas produced for the UWIBASS were two Archimedean spiral printed circuit board (PCB) antennas in a bistatic configuration (see Figure 5.1a). These antennas deliver excellent impedance matching across a large bandwidth; however, the directivity was low. The spiral antenna radiates an equal amount of power in both directions incident to its plane (see Figure 5.1c). Hence, a cavity backing of absorbent material was needed to reduce ringing and interference with the unmanned aerial vehicle (UAV) electronics.



(a) Spiral antennas with cavity backing mounted under radar electronics box.

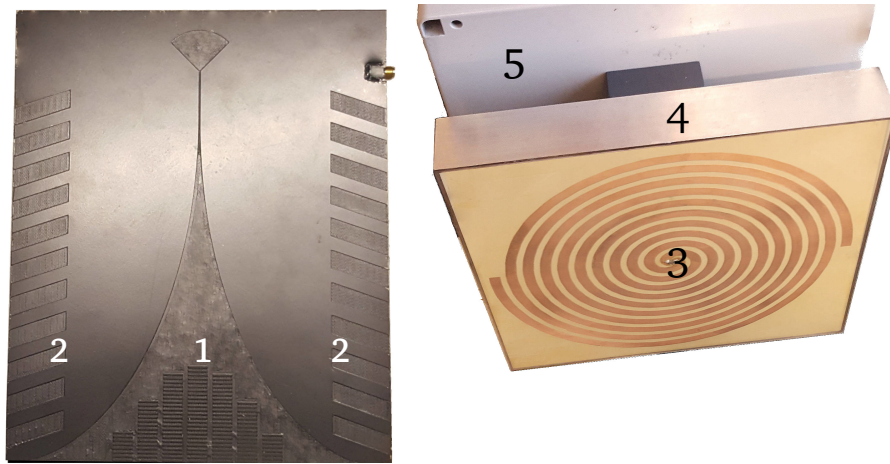


(b) Produced PCB of spiral antennas.

(c) Simulated radiation pattern for spiral antenna.

**Figure 5.1:** The first iteration of the radar system with the complete mounted system (a), close up of the spiral antennas (b), and the radiation pattern of spiral antennas.

The second iteration of the antenna configuration consisted of a spiral transmitting (TX) antenna and two Vivaldi receiving (RX) antennas mounted in a 90 degree offset, shown in Figure 5.2. This configuration enabled circular polarization transmission and linear polarization reception with each linearly polarized signal in 90-degree offset, resulting in hybrid polarization where the reflected signal could be reconstructed by the two RX channels.



(a) Vivaldi antenna prototype with printed lens (1) and inserted slits (2), and Archimedean spiral antenna (3) with cavity backing (4) mounted below radar box (5). The spiral is superimposed on the image as it is not visible from the outside.



(b) Radar system mounted on an octocopter drone (Kraken), with the transmitting spiral antenna (1) mounted below the radar box (2), and the two receiving Vivaldi antennas (3) in 90 degrees offset on the sides.

**Figure 5.2:** The second iteration of the radar system with spiral and Vivaldi antennas (a) and radar system mounted on Kraken (b).

Vivaldi antennas are widely used in UWB systems much due to their light-weight and the ease of production through PCB etching or milling technology [4]. The Vivaldi antennas were modified beyond the standard Vivaldi design to reduce the antenna footprint and increase directivity. The main improvements are listed as follows:



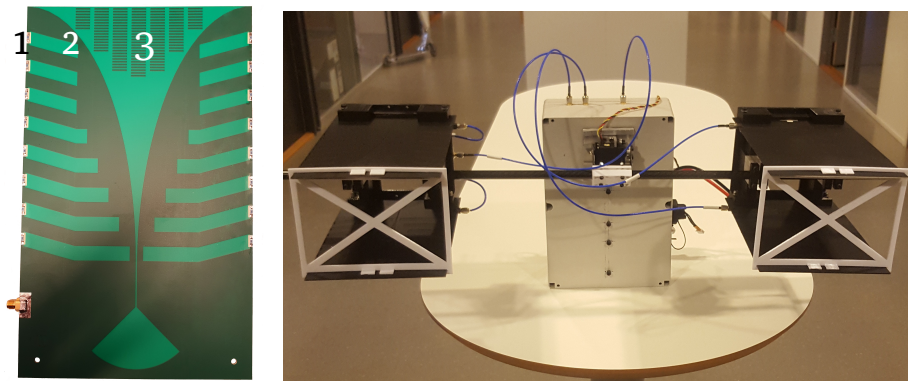
- **Printed lens in aperture:** [4] conducted research on printed lenses in the Vivaldi antenna aperture where it was found that the use of printed lens leads to increased gain and reduced sidelobe levels. The lens was fabricated in the same manner in our antennas, only modified to accommodate the larger bandwidth requirements for the UWIBASS.
- **Inserted slits:** [54] proposed the use of inserted slits in tapered slot antennas, demonstrating a significant increase in bandwidth with implemented slits of adequate size compared to the basic tapered slot antenna. A similar design was implemented on the Vivaldi antennas in order to obtain the required bandwidth while keeping a minimum antenna area. Figure 5.2a shows the prototype antenna with both slits and printed lens patches.

The third antenna configuration (and the present one) consisted of four next-generation Vivaldi antennas mounted in pairs as RX and TX arrays, shown in Figure 5.3b. With this configuration, we add a transversal dimension to the otherwise planar antennas. Thus, we focus the antenna beam along the most de-focused axis (H-plane), significantly improving overall antenna directivity compared to a single element (see Figure 4 in Paper II).

In addition to the previously mentioned Vivaldi modifications, resistive loads in the opening of the inserted slits were added to dissipate the current distribution occurring at the sides of the antennas (see Figure 5.3a). This modification reduces ringing from residual energy not radiated by the antenna at the front aperture, hence, reduced  $S_{11}$ . It was found, through simulation, that a resistor value of approximately  $1\text{ k}\Omega$  is optimal. After fabrication of the antenna PCB, a simple  $S_{11}$  test of  $1\text{ k}\Omega$ ,  $10\text{ k}\Omega$  and open ( $\approx \infty\ \Omega$ ) was tested to crudely indicate that  $1\text{ k}\Omega$  was best suited as in the simulation. Due to the large amount of work involving soldering different resistors onto the antenna for testing more resistor values, no further testing was conducted.

The degree of freedom related to the spacing between the antennas was optimized through simulation. The ideal distance for a 0.7 to 4.5 GHz bandwidth was found to be approximately 11 cm maximizing antenna gain while maintaining low spurious sidelobes.

Figure 5.3b shows the two sets of Vivaldi antennas mounted in a bistatic configuration with approximately 50 cm spacing between the pairs. The TX signal is distributed to the two Vivaldi antennas using a 2-way power splitter. The radar system has two RX inputs enabling a direct connection with each RX antenna. The antenna mounting is entirely 3D printed, resulting in a light-weight, easy to manufacture, and nearly electrically neutral part.



(a) Vivaldi antenna, with resistive loads (1), inserted slits (2), and printed lens in aperture (3). (b) Vivaldi antenna arrays (painted black) mounted in a bistatic configuration using 3D printed parts.



(c) Antenna prototype (and radar box) mounted under "Cryocopter FOX." The antenna angle regulation mechanism has a slight angle when not powered up to ensure tension on stabilizing bungees when pointing in nadir.

**Figure 5.3:** The third iteration of the radar system with close up of modified Vivaldi antenna (a), radar system with dual Vivaldi antennas (b), and the same radar system mounted under a UAV (c).

During this project, approximately 60 unique parts for the UWIBASS was 3D modeled, prototyped, and produced, mostly with 3D printing, but also in aluminium using machining tools. Some of these parts are described in the

next section.

## 5.2 Hardware Development

The radar system consists of several modules on both the digital and radio frequency (RF) side. As in the previous section, the active electronics have also gone through several iterations. An overview of the complete radar system is outlined in Figure 5.4. Here, it is shown that the system consists of 3 main parts: The radar system itself, the UAV and the ground station to control the radar system. It is important to include the UAV in the diagram as the radar data depends on the autopilot data to reference each measurement in space. The radar computer (Odroid<sup>1</sup>) collects autopilot data through a Mavlink data-stream where altitude, global positioning system (GPS) position, and attitude (roll, pitch, and yaw) is fused with the radar data.

The ground station has an individual radio-link to the radar where the measurements can be controlled and monitored. Real-time processing and visualization of the radar data live at the ground station is enabled with a high bandwidth connection.

The central part of the radar system is the ILMsens m:explore SH-3100<sup>2</sup> RF measurement device. It was developed for a range of different measuring requirements. The m:explore reliably serves four fields in total: Impedance spectroscopy, microwave imaging, short-range radar, network analysis, and time-domain reflectometry. For our application, the sensor is used as a short-range radar.

The radar system is controlled by a single board acquisition computer that communicates with the SH-3100 and the ground station while simultaneously pre-processing the collected data in a parallel process. The demand for computing power is high in such a system, especially if the goal is a high measurement rate (IRF/s). A single measurement with the SH-3100 (m9 sensor and two RX channels) is approximately 10 kb of data, resulting in a data rate of 10 Mb/s for a 1 kHz measurement rate, which implies a high computational load if we are to pre-process the data and transmit it back to the ground station.

1. Visit Hardkernel at: <https://www.hardkernel.com/>

2. Visit the ILMsens website at: <https://www.uwb-shop.com/products/m-explore/>

### UWiBaSS block diagram

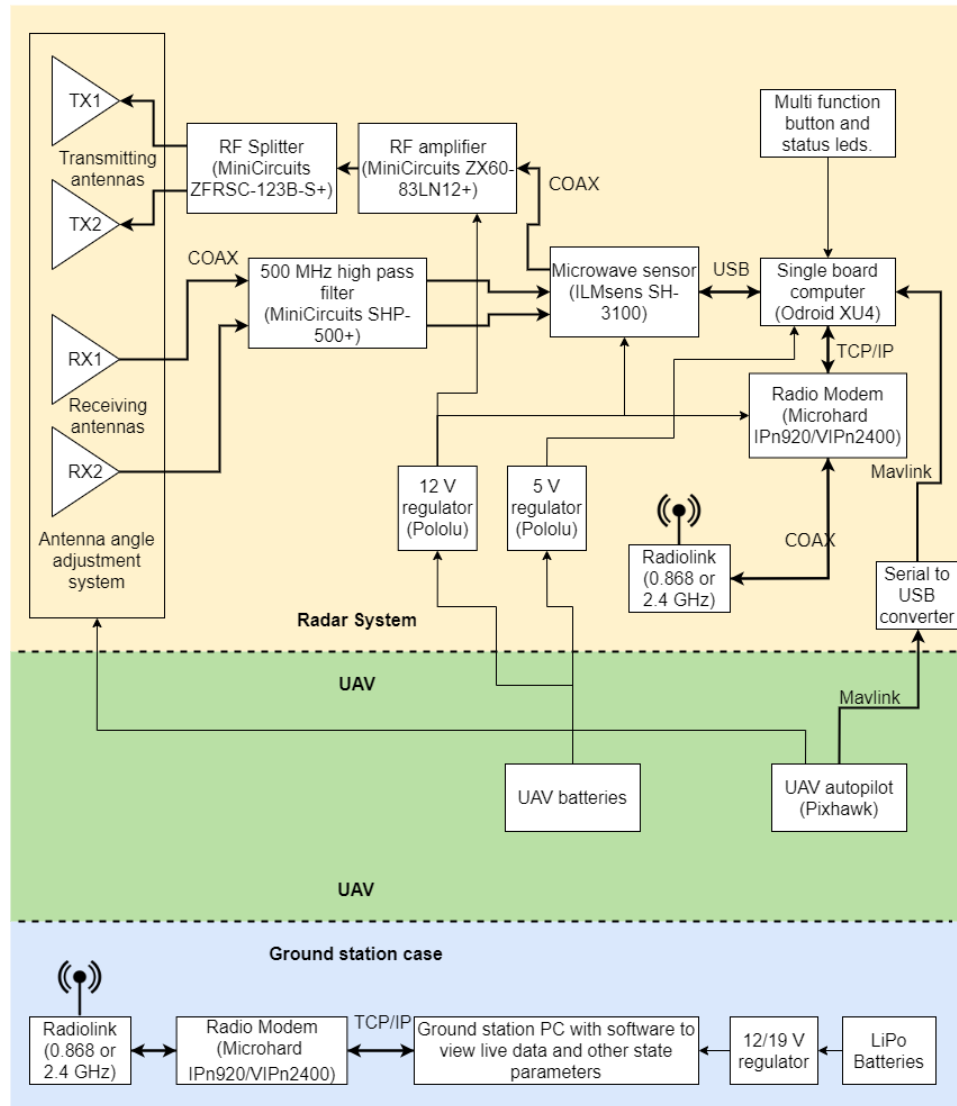


Figure 5.4: Block diagrams of the UWiBaSS.

On the transmitting side of the RF path, several different amplifier-modules have been used. The main parameters for choosing an amplifier for this system is size, bandwidth, and gain. Recently, Minicircuits released the ZX60-83LN12+, which has a significantly higher gain than previous models with similar bandwidth.

Following the signal path in Figure 5.4, the next module is a high bandwidth signal splitter to enable transmission on both of the TX antenna elements. After the splitter, we use semi-rigid coaxial cables of equal length to ensure equal phase at the active region of the antennas.

The crosstalk in a bistatic radar system is dominated by the low-frequency components of the transmitted signal [99]. Hence, a high pass filter (500 MHz cutoff) is mounted on the receiving path to reduce transceiver crosstalk. The high pass filter enables higher TX output power without saturating the RX channel, and the separation between the two channels can be reduced. The high pass filter can easily be removed to ensure that all low-frequency content is received, e.g., when measuring wet snow.

During the first field test, it was found that an antenna angle adjustment system was needed to regulate the angle as close to nadir as possible since the UAV often has a slight angle of attack while flying. The 3D printed antenna mount was then fitted with a servo motor set up to be directly controlled by the UAV autopilot.

Typically, the modules used in the UWIBASS have metal casings, usually aluminium. To reduce weight and ensure maximal flight time, many of the casings were remodeled in 3D CAD software and printed in PETG plastic. The plastic casings were coated in nickel-silver conductive paint to assure sufficient electromagnetic interference (EMI) shielding from the different modules. This modification resulted in a weight reduction for each module of 75% compared to the original aluminum housings.

### 5.3 Software Development

The main goal of the software development was to create a program that can handle the high-speed data stream as efficiently as possible while keeping tabs on internal temperatures that might overheat in the closed waterproofed box. Throughout this project, approximately 17 000 source lines of code (SLOC) [2] was written in several different programming languages including Python (1k), C++ (1k) and Matlab (15k).

The basic architecture for the UWIBASS software consists of a set of C++ functions that handle the transmission, collection, and pre-processing of the radar data, all controlled by a Python wrapper that handles communication and synchronization with the autopilot, file organization, communication over the radio-link, fail-safe modes and activation, initialization and other controls for the radar sensor.

This type of program architecture was chosen for its high-level programming of tasks with low computational load and dedicated functions written in a lower-level language to handle the heavy lifting. Figure 5.5 shows the workflow in the software with color codes for programming language and user inputs over radio-link.

The post-processing scripts were mainly written in MatLab; however, a light-weight version of the post-processing was implemented as a Python script as well. In short, the post-processing involves subtracting the dataset with a reference measurement (i.e., free space measurement), bandpass filtering, Fourier domain windowing, and Hilbert transforming [45]. The supplemental data, such as the fast-time vector, is used to generate depth vectors that are further modified after the snow propagation velocity is estimated. The UAV autopilot data (e.g., GPS, altitude, attitude) is referenced to the radar data by their corresponding timestamps and is interpolated to an appropriate size for geo-referencing. These processing steps are described in more detail in [45, 46].

At this point in the post-processing, the data goes through light image processing steps such as Wiener filtering and, optionally, a contrast enhancement procedure to improve snow interface visibility. Finally, analysis methods developed during this project are conducted, including the depth estimation presented in Paper I and Paper II, the altitude and gain correction presented in Paper II, and the auto-focusing procedure to estimate density presented in Paper III.

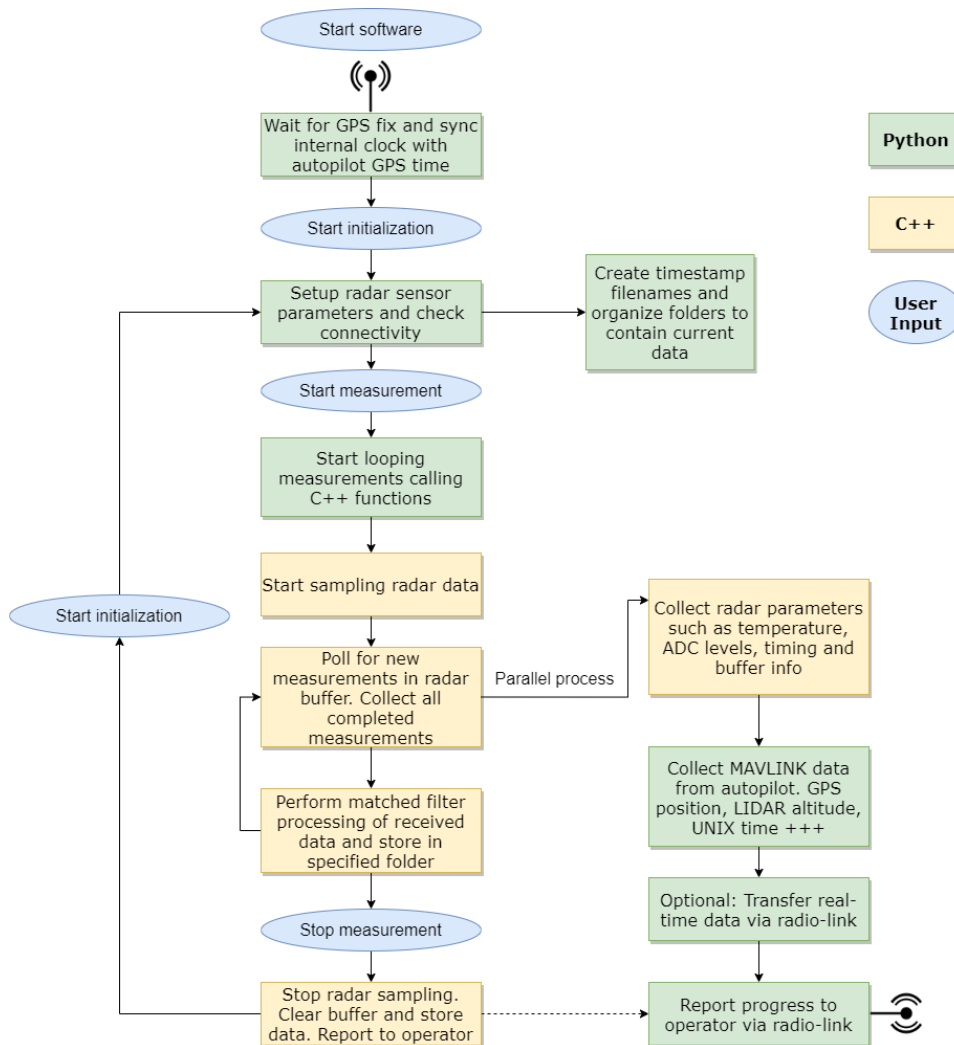


Figure 5.5: Block diagram of the UWIBASS program workflow.

## 5.4 Final Remarks on the UWIBASS

The UWIBASS is a radar system under constant development. Modifications are made to customize the transmitted signal for the sensing task at hand, such as lowering the frequency response for sea ice sensing. Additionally, modules are added to improve the overall system performance as new technologies arise.

The current radar system is optimized for snow measurements. That involves antennas specifically designed to push the bandwidth below 1 GHz for better penetration depth in wet snow while still keeping acceptable performance up to 4.5 GHz to retain resolution. The key characteristics of the current version

**Table 5.2:** UWiBaSS key characteristics.

<b>Attribute</b>	<b>Value</b>
Signal generation	UWB Pseudo noise
System bandwidth	3.8 GHz (0.7 to 4.5 GHz)
Range resolution	$\approx 5$ cm
M-sequence clock frequency	12.8 GHz
Measurement rate	52 Hz (max 1 kHz)
MLBS order	9 (511 range bins)
Nominal output power	17.3 dBm
Unambiguous range in air	5.98 m
Average power consumption	8.1 to 9 W
Total Weight	$\approx 3$ kg

of the UWiBaSS are listed in Table 5.2.

The UWiBaSS is the result of extensive field testing where in addition to data collection, meaningful hands-on experience is gained in regards to UAV mounted instrumentation. This includes mechanical stability, EMI, communication solutions, and the development of small and light-weight sensor systems.

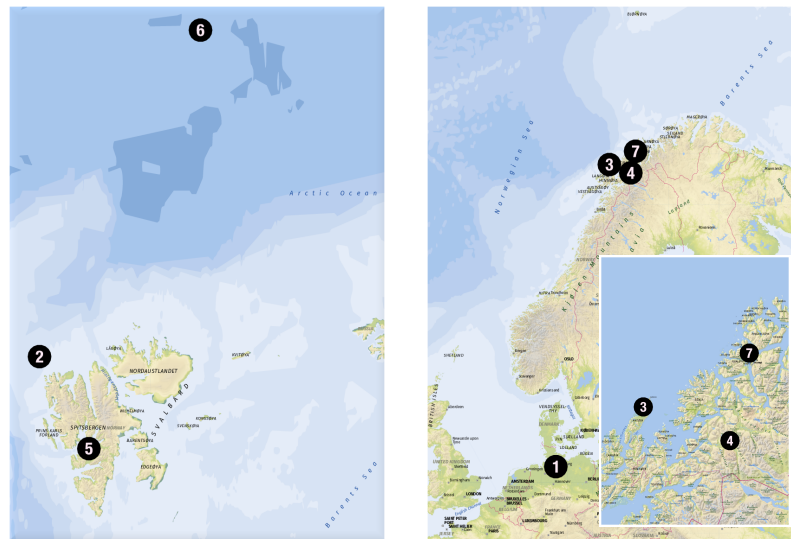


# /6

## Fieldwork

To adequately test a newly developed radar system, accurate ground truth (*in situ*) information is essential to validate the sensor and methods. This chapter describes the conducted field campaigns from which the data in this work originates and other campaigns and experiments where the results are published in reports or are to be published in the future.

Some other campaigns are not mentioned here as they were conducted mainly to test different iterations of the radar system or its integration into the unmanned aerial vehicle (UAV) platform. The locations of the above-mentioned campaigns are shown in Figure 6.1 where the tag numbers correspond to the following section numbers in this chapter.



(a) Svalbard and polar ice locations. (b) Norway and Germany locations, with zoomed-in section.

**Figure 6.1:** Fieldwork locations described in the following sections where the numbers correspond to the section numbers.

## 6.1 MOSIDEO/CIRFA Experiment HSVA Hamburg, Germany [14/03/2017 to 04/04/2017]

In the Arctic, the presence of sea ice presents a challenge to safe and sustainable operations. To optimize planning and minimize the impact of inadvertent oil spills, oil-in-ice experiments were performed in the Arctic Environmental Test Basin (AETB) at the Hamburg Ship Model Basin (HSVA) from 14 March to 4 April 2017 [83]. These experiments were part of the Microscale interaction of oil with sea ice for detection and environmental risk management in sustainable operations (MOSIDEO) project.

The main goal for the ultra-wideband snow sounder (UWIBASS) was to investigate the possibility to detect the presence of oil spills under the ice surface. Due to wet ice conditions, the radar was not able to penetrate the ice. However, differences in surface roughness between two different ice types (columnar and granular) could be detected (see Appendix A.4).

The author also installed and operated several other instruments during the experiment. Those sensors include an IR camera, a spectrometer (Trios Ramses), a surface roughness laser, a fluorescence meter, and a hyperspectral camera (Rikola). The infrared (IR) camera provided some interesting results by de-

tecting surface temperature changes when the oil was injected. The oil spill underneath the ice acts as an insulating layer impeding the flow of heat from the water, effectively creating cold patches on the ice surface [53], which were detected with the IR camera.

## 6.2 INTPART Cruise

### Polar ice edge (RV Lance) [18/05/2017 to 24/05/2017]

The INTPART program promotes the development of long-term relations between Norwegian higher education and research institutions and strong research groups and institutions in eight priority partner countries: Brazil, Canada, China, India, Japan, Russia, South Africa, and the US. From 2017, the program also included partnerships with institutions in Germany and France. The INTPART program is a collaborative effort between the Research Council of Norway and the Norwegian Agency for International Cooperation and Quality Enhancement in Higher Education (DIKU).

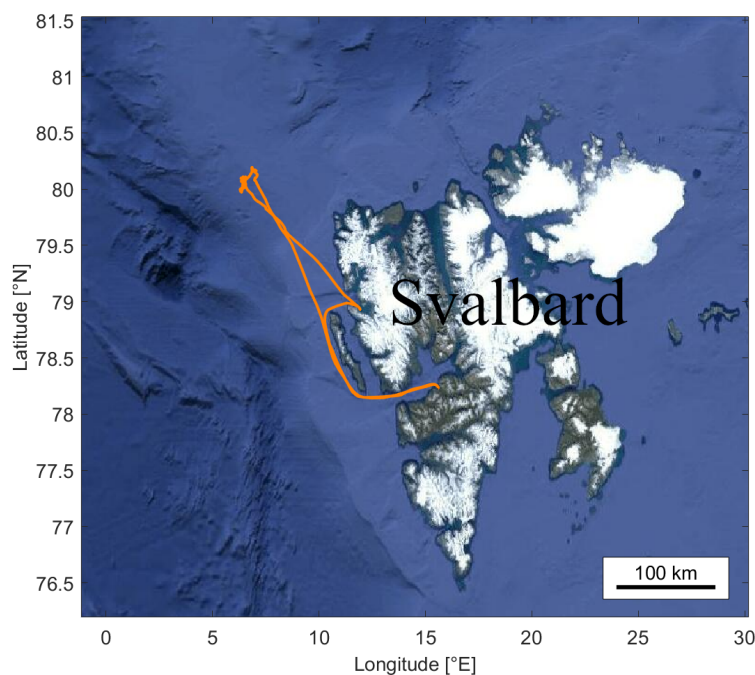


**Figure 6.2:** Plot of the position of RV Lance during the INTPART 2017 cruise.

A part of the INTPART program involves field courses, and this particular field course took place at the polar ice edge outside Svalbard onboard RV Lance. The main goal of the cruise was to educate Ph.D. and Master students about fieldwork on sea ice, such as taking ice cores, measuring snow density, salinity and taking CTD's (Conductivity, Temperature, Depth) of the ocean water column. Additionally, we were able to bring the UWIBASS and the Kraken UAV. Both airborne and handheld measurements with the UWIBASS were conducted on the ice stations. With the first flight over sea ice, we collected field data reported in Paper I.

The cruise included a visit to Ny-Ålesund where we visited the Koldewey-station of the German Alfred Wegener Institute (AWI). Here we witnessed a weather balloon launch at the "Balloon house" and was presented the Koldewey Aerosol Raman Lidar (KARL) used to determine the concentration of aerosols in the atmosphere.

Figure 6.2 shows a plot of the ship position during the cruise indicating the areas where work on the ice was performed (farthest north), and the visit to Ny-Ålesund.

### **6.3 Statens Vegvesen Demo Andøya, Norway [14/02/2018 to 16/02/2018]**

This campaign was the first demonstration for a contractor, The Norwegian Public Roads Administration<sup>1</sup> (Statens Vegvesen). In this case, we investigated the possibility of detecting buried people under a wet snowpack.

The demonstration took place on Andøya, where we showed that the radar could resolve snow stratigraphy in wet snow conditions and detect a buried person under 1.5 m of wet snow.

This campaign is the first the author did not attend personally. Thus a comprehensive manual was written to allow other users to operate the UWIBASS. This manual is continuously updated where the goal is that many other researchers can use the UWIBASS without too much prior knowledge.

1. Visit NPRA: <https://www.vegvesen.no/>

## **6.4 Freshwater Lake Experiment Bardu, Norway [14/02/2018 to 16/02/2018]**

This campaign set out to test the latest version of the radar system on the Kraken UAV. The test took place on a freshwater lake in the mountains of Bardu, close to the UAV pilots (Tore Riise) cabin [68.8°N, 18.3°E]. Here we evaluated the performance of the radar system operating in cold conditions measuring thick snow and ice. One challenge discovered on this campaign was that the FPGA module of the ILMsens SH-3100 sensor had occasional errors when the temperature of the sensor dropped below approximately 0°C where the USB interface disconnected from the Odroid computer. This issue was fixed by mounting a small heating element inside the radar. An automatic "re-connect and resume measurements" sequence was added to the radar's main control program. Additionally, a new field protocol was implemented where power should be applied to the radar for at least 5 minutes before starting measurements. The discussed malfunction has not occurred after these improvements.

As presented in Appendix A.2, the UWIBASS demonstrated the ability to measure ice thickness on the freshwater lake. This result was presented at the International Snow Science Workshop (ISSW) in Innsbruck, 2018.

## **6.5 SIOS Field Campaign Svalbard, Norway [30/03/2019 to 04/04/2019]**

Svalbard integrated arctic earth observing system (SIOS) is a regional observing system for long-term measurements in and around Svalbard, addressing Earth System Science questions and to bring observations together into a coherent and integrated observational program that will be sustained over a long period. Within SIOS, researchers can cooperate to access instruments, acquire data, and address questions that would not be practical or cost-effective for a single institution or nation alone.

This field campaign took place on selected locations on inland Svalbard (see Figure 12, in Paper II), where snow depth was mapped in 100 by 100 m grids and delivered as a data product to SIOS.

With an average temperature of approximately -20°C, the experiences made in terms of cold weather operations from the Bardu campaign came to good use.

The data collected on this campaign was used in Paper II.

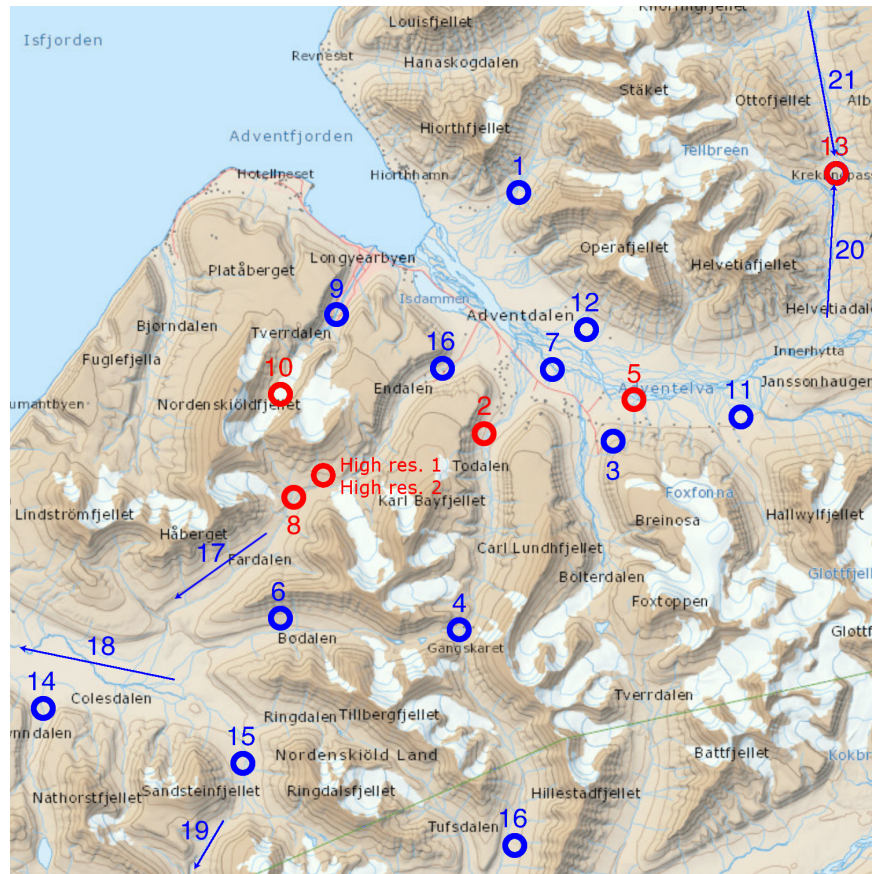
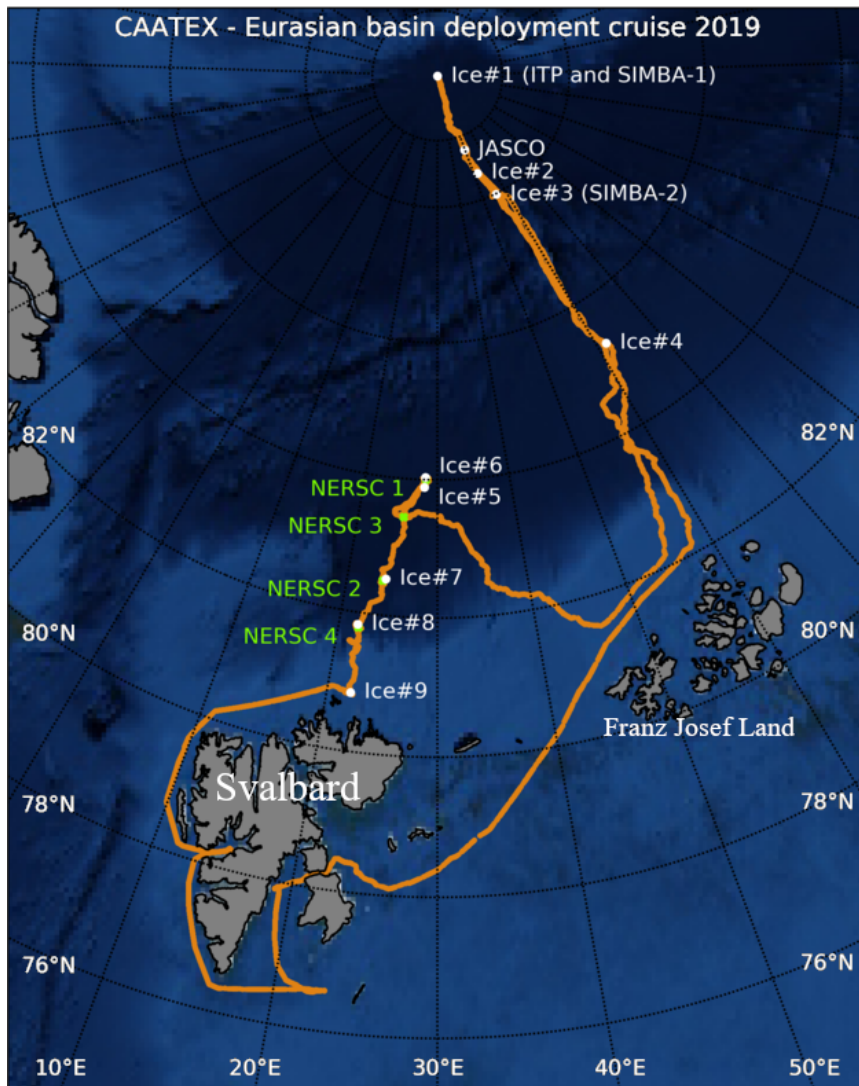


Figure 6.3: Fieldwork locations around Longyearbyen for the SIOS campaign.

## 6.6 CAATEX Cruise Polar ice cap (KV Svalbard) [13/08/2019 to 10/09/2019]

The coordinated arctic acoustic thermometry experiment (CAATEX) addresses research in the central Arctic Ocean, especially the ocean climate change. The Arctic region experiences substantial climate change, but yet the central Arctic Ocean under the sea ice is poorly observed and remains largely unknown. A particular focus in CAATEX is to obtain regional to basin-scale information about ocean temperature from acoustic thermometry and standard oceanographic instrumentation.



**Figure 6.4:** Plot of the position of KV Svalbard during the CAATEX cruise. Ice stations and buoy deployments are marked as Ice# and NERSC, respectively.

This campaign took place on the polar ice cap onboard KV Svalbard. The main task of the cruise was to deploy sonar buoys to measure the mean temperature of the polar sea [118]. The UWIBASS and Cryocopter FOX tagged along and managed to get time to work on the ice during the night while the crew was resting (except the polar bear guards). We performed airborne sea ice measurements with the radar during this campaign and took *in situ* data such as ice thickness, ice cores, snow depth, and freeboard.

Figure 6.4 shows a plot of the ship position during the cruise and the ice stations

where the radar measurements were taken. Additionally, Figure 6.4 shows the locations the sonar buoy was deployed, marked as NERSC1, 2, et cetera.

Side note: This cruise ended up writing a bit of polar history as KV Svalbard managed to reach the North Pole as the first Norwegian ship to do so.

## 6.7 Finnvikdalen Experiment Tromsø, Norway [02/04/2020]

Two field campaigns was planned for the winter season of 2020:

- **SIOS field campaign:** Set out to measure snow depth and density in long (20 km) transects.
- **Varicon/Statkraft Suldal campaign:** Field demonstration for Statkraft comparing traditional sled ground penetrating radar (GPR) with the UWIBASS mounted on a UAV. Set out to measure snow depth and density for snow water equivalent (SWE) estimation.

The main scientific goal of these campaigns was to test methods to estimate snow density, where the migration velocity analysis (MVA) method described in Section 4.3 was to be tested. Both of these campaigns were canceled due to the Covid-19 outbreak, and efforts were made to find alternatives to test the proposed method.

As a plan B after the cancellations, a small scale experiment was conducted in early April in Finnvikdalen. With limited resources and gear, the main task of this campaign was to test the upgraded radar system and different methods to estimate snow density.

Figure 6.5 shows the location of the site on Kvaløya in Tromsø.

The dataset for this campaign resulted in sparking the idea for the method proposed in Paper III, and was used as the field trials data.



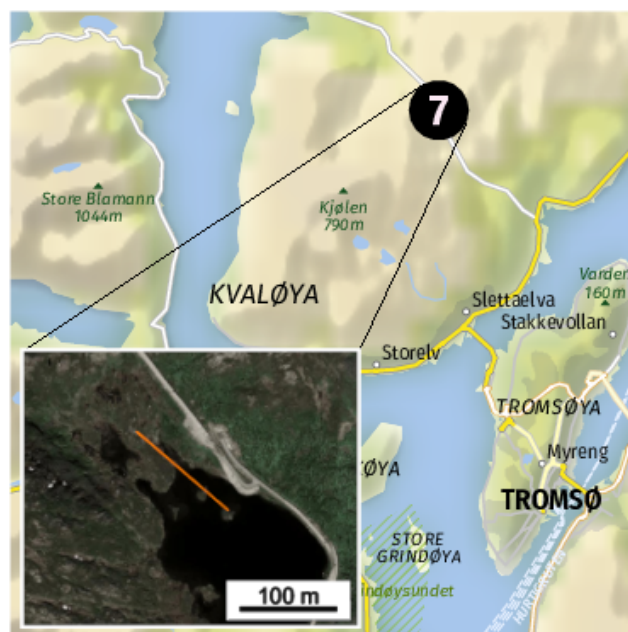


**Figure 6.5:** Map showing the location of the Finnvikdalen experiment and zoomed-in section showing the transect that was measured.





# Overview of Publications

This chapter provides an executive summary of the three publications presented in Chapters 8-10.

## 7.1 Paper Summaries

### Paper I

R. O. R. Jenssen, M. Eckerstorfer & S. Jacobsen "**Drone-Mounted Ultrawideband Radar for Retrieval of Snowpack Properties**", IEEE Transactions on Instrumentation and Measurement, vol. 69, no. 1, pp. 221-230, Jan. 2020

This paper introduces the radar system and goes through important design considerations for drone-mounted ground penetrating radar (GPR). The hardware and the integration onto the drone are described in detail. At this point, the ultra-wideband snow sounder (UWiBASS) is at the second iteration described in Chapter 5, and the pros and cons of the spiral antenna are discussed. Results from field trials are presented with good correlation compared to *in situ* validation data with a correlation of 0.87. This paper serves as a future reference that describes the technical implementation of the UWiBASS in more detail.

### *Contributions by the authors*

The design parameters for the prototype radar system were established in collaboration with S. Jacobsen. Antenna design, simulation, and fabrication were conducted by S. Jacobsen. Mechanical design, fabrication, and installation were done by me. I wrote all the code for the radar operation, post-processing, and analysis. I executed the fieldwork and analysis. *In situ* measurements were conducted by M. Eckerstorfer, and I wrote the first draft of the manuscript. All the authors contributed to finalizing the paper.

## **Paper II**

R. O. R. Jenssen & S. Jacobsen "**Drone-mounted UWB snow radar: technical improvements and field results**", *Journal of Electromagnetic Waves and Applications*, 2020, 34:14, 1930-1954.

This paper presents the next iteration of the UWIBASS, a new processing method, and field results. In particular, we introduce a novel antenna configuration, useful processing techniques for drone borne radar such as altitude correction, and we show snow depth measurements taken in grid flights compared to *in situ* depth in the same grid. The grid measurements are compared, yielding a spatial correlation coefficient of 0.97. Additionally, we observe that two shorter transects where *in situ* snow depth is taken, at ten times higher resolution (high res. 1 and 2) compared to the grid surveys, show significantly higher correlations suggesting that the manual *in situ* measurements are too sparse to be directly interpolated and compared to the radar data.

### *Contributions by the authors*

The antenna system improvements were developed in collaboration with the co-author. Antenna design, simulation, and fabrication were conducted by S. Jacobsen. Other improvements to the UWIBASS were conceived and implemented by me; including mechanical design, fabrication, installation, and communication with the unmanned aerial vehicle (UAV) autopilot. I wrote all the code for the radar operation, post-processing, and analysis. I executed the fieldwork and analysis. *In situ* measurements were conducted by H. Wickers. I wrote the first draft of the manuscript. Both authors contributed to finalizing the paper.

### Paper III

R. O. R. Jenssen & S. Jacobsen "**Measurement of Snow Water Equivalent Using Drone-Mounted Ultra Wide-Band Radar**", In review.

This paper presents an improved scheme for measuring snow water equivalent (SWE) from a moving UAV which in turn is based on non-invasive snow density measurements from the same platform. The scheme involves estimating snow depth and density by using well-established F-K migration theory and the Dix equation for layered media in addition to altitude correction of the flying platform presented in Paper II. The goal is to estimate the propagation velocity in the snow using an autofocusing metric on migrated sections of radar data with different test velocities. The paper describes the method in detail and presents results from Monte Carlo simulations of the method to establish that the method is unbiased, which is important if we are to use spatial averaging on the estimations to reduce noise.

Finally, results from a field trial are presented, which (albeit limited in volume) show good agreement with *in situ* density and good agreement with the Monte Carlo simulations for the statistical spread of snow density estimates. Depth measurements up to 5.5 m are also presented where the radar system proves capable of highly repeatable depth measurements from an altitude of 7 m above the snow surface.

#### *Contributions by the authors*

The initial idea was conceived by the co-author and me. All improvements to the UWIBASS, mechanical design, mounting, and communication with the UAV autopilot were made by me. I implemented all the code for the analysis except for the appendix. I executed the fieldwork and analysis. *In situ* measurements were executed by M. Eckerstorfer. I wrote the first draft of the manuscript. Both authors contributed to finalizing the paper.

## 7.2 Other Publications

### As first author

1. Jenssen, R. O. R., Eckerstorfer, M., Vickers, H., Høgda, K. A., Malnes, E., & Jacobsen, S. K. (2016, October). **Drone-based UWB radar to measure snow layering in avalanche starting zones**. In Proceedings of the International Snow Science Workshop, Breckenridge, Colorado (pp. 573-

577) 2016.

This conference paper outlines the general idea of the radar system and show preliminary results from the proof of concept trials. We present the testing of a UWB radar system and show its capabilities of detecting snow stratigraphy. To simulate airborne operations, we have during the spring 2016 operated the radar system via a stationary rig 1 m above the snow, along 4.2 m long transects. For verification, we dug a full snow profile pit, identifying snow stratigraphy, liquid water content, and snow density

2. Jenssen, R. O. R., Eckerstorfer, M., Jacobsen, S. K., & Storvold, R. (2018, October). **Drone-Mounted UWB Radar System for Measuring Snowpack Properties: Technical Implementation, Specifications and Initial Results.** In Proceedings of the International Snow Science Workshop, Innsbruck, Austria (pp. 7-12) 2018.

In this conference paper, we present the characteristics and specifications of the current drone-borne radar system and show results from two different campaigns. We were able to resolve snow stratigraphy in great detail in a dry snowpack, identifying the most prominent layers. Our second example shows the system's capabilities of detecting a person buried under 1.5 m of wet snow.

### **As co-author**

3. M. Eckerstorfer, R. O. R. Jenssen, A. Kjellstrup, R. Storvold, E. Malnes, and S. K. Jacobsen, **UAV-borne UWB radar for snowpack surveys**, Report for Statens Vegvesen, 2018.

A report for The Norwegian Public Roads Administration (NPRA) summarizing the capabilities and technical characteristics of the UWIBASS and Kraken UAV, designed for conducting snow surveys. During a demonstration performed at Andøya, Norway, the radar system proved capable of resolving snow stratigraphy in wet snow conditions, as well as detecting a buried person under 1.5 m of wet snow

4. C. Petrich et al., **An overview of the Mosideo/Cirfa experiments on behavior and detection of oil in ice**, 41st AMOP Tech. Semin. Environ. Contam. Response, AMOP 2018, no. October, pp. 112–122, 2018.
5. C. Petrich et al., **MOSIDEO/CIRFA tank experiments on behavior and detection of oil in ice**, in Proceedings of the International Conference on Port and Ocean Engineering under Arctic Conditions (POAC), 2019,

vol. 2019-June. Also presented at The International Glaciological Society Sea Ice Symposium.

These papers present the setup of the HSVA oil in ice experiment and general ice properties from the samples. It was found that the movement of oil differed considerably between the investigated ice types (Columnar and granular). Predicting the behavior of oil in ice based on environmental conditions will help optimize the approaches used in spill detection and response.







## Paper I

### **Drone-Mounted Ultrawideband Radar for Retrieval of Snowpack Properties**

Rolf Ole Rydeng Jenssen, Markus Eckerstorfer & Svein Ketil Jacobsen

Published in:

*IEEE Transactions on Instrumentation and Measurement*, vol. 69, no. 1,  
January 2020





## Paper II

### **Drone-mounted UWB snow radar: technical improvements and field results**


Rolf Ole Rydeng Jenssen & Svein Ketil Jacobsen

Published in:

*Journal of Electromagnetic Waves and Applications, vol. 34, no. 14,  
August 2020*



# Drone-mounted UWB snow radar: technical improvements and field results

Rolf Ole R. Jenssen <sup>a,b</sup> and Svein Jacobsen<sup>a,b</sup>

<sup>a</sup>UiT – The Arctic University of Norway, Tromsø, Norway; <sup>b</sup>NORCE – Norwegian Research Centre, Tromsø, Norway

## ABSTRACT

Drone borne radar systems have seen considerable advances over recent years, and the application of drone-mounted continuous wave (CW) radars for remote sensing of snow properties has great potential. Regardless, major challenges remain in antenna design for which both low weight and small size combined with high gain and bandwidth are important design parameters. Additional limiting factors for CW radars include range ambiguities and antenna isolation. To solve these problems, we have developed an ultra-wideband snow sounder (UWiBaSS), specifically designed for drone-mounted measurements of snow properties. In this paper, we present the next iteration of this prototype radar system, including a novel antenna configuration and useful processing techniques for drone borne radar. Finally, we present results from a field campaign on Svalbard aimed to measure snow depth distribution. This radar system is capable of measuring snow depth with a correlation coefficient of 0.97 compared to in situ depth probing.

## ARTICLE HISTORY

Received 25 March 2020  
Accepted 18 July 2020

## KEYWORDS

UWB radar; antenna design; UAV; snow;

## 1. Introduction

A complete understanding of the Arctic cryosphere has historically been hindered by its large extent, remoteness, and restrictions in measurement methods and equipment. Remote sensing provides methods for observing the snow cover through indirect measurement and parameter estimation. For instance, ice extent is often estimated without direct verification [1,2], but many cryospheric properties including snow thickness or density require direct measurement for calibration and validation [3]. In cryospheric data collection, such as snow pits and ice core extraction, sample site selection and sample size are limited by weather, safety concerns, marine navigability as well as snow or ice thickness, convenience, and accessibility. Therefore, it is of interest to study the application of unmanned aerial vehicle (UAV)-based radar, which could offer efficient, non-invasive, and continuous field data collection of cryospheric data. This includes snow depth and

**CONTACT** Rolf Ole R. Jenssen  [rolf-ole.r.jenssen@uit.no](mailto:rolf-ole.r.jenssen@uit.no)

© 2020 The Author(s). Published by Informa UK Limited, trading as Taylor & Francis Group  
This is an Open Access article distributed under the terms of the Creative Commons Attribution-NonCommercial-NoDerivatives License (<http://creativecommons.org/licenses/by-nc-nd/4.0/>), which permits non-commercial re-use, distribution, and reproduction in any medium, provided the original work is properly cited, and is not altered, transformed, or built upon in any way.

stratigraphy, potentially expanding datasets used for modeling, or used directly as a data product.

In the context of remote sensing of snowpack parameters, the microwave response from snow is determined by snowpack parameters (depth, density, liquid water content, layering, crystal structure, temperature, surface roughness) and radar parameters (range, frequency, incidence angle). Therefore, ground truth data are often required to verify or calibrate measurements. As such, the success of indirect data collection for calibration and validation relies on the ability of the data acquisition device to measure these properties.

This study focuses on the indirect measurement of snow thickness and stratigraphy with high precision, where, in the case of dry snow, the main contributing element for such measurements is snow density. Snow density directly influences the dielectric constant of snow [4], which in turn influences the reflection of the radar signal. Snow density is currently manually measured, but future work includes a study with the aim to develop methods for extracting this parameter directly from radar measurements.

The UWIBaSS discussed in this paper is a ground-penetrating radar system developed for drone-mounted operations. A preceding iteration of this radar system was presented in [5].

Previous studies show that ultra wide-band (UWB) radars are able to measure snow depth and even stratigraphy with high accuracy. For instance, an 8–18 GHz frequency modulated continuous wave (FMCW) system was found to generate stratigraphic snow information with a correlation coefficient,  $C$ , of 0.92 relative to *in situ* depth measurements up to snow depths of 30 cm [6], while other studies show similar, but smaller, correlations:  $C = 0.86$  [7], and  $C = 0.78$  [8]. Nevertheless, one should note that high correlations are achieved, however, only at shallow snow depths up to 30 cm. A recent study demonstrates a lightweight FMCW Ku-band (14–16 GHz) radar for snowpack remote sensing [9]. Additionally, a gated step-frequency ground penetrating radar (GPR), operating in the 0.5–3 GHz range, enables snow and ice measuring capabilities to a depth of 11 m, operated from a snowmobile platform [10]. Moreover, it has previously been shown that aircraft-mounted radar systems are also capable of measuring snow depth with  $C = 0.88$  *in situ* correlation [11], while other radar systems demonstrate snow interface detection [12], or even both snow and ice interface detection [13]. Another paper established design parameters for a UAV mounted radar intended for snow parameter retrieval [14], with a recommended operating frequency in the 1.5–4.5 GHz band. Furthermore, a number of other research groups have described UWB radars for UAV mounting, where the applications range from detection of ground targets such as cars, humans [15,16], and ships [17] as well as topographic mapping [18], detection of buried objects including landmines [19] and other high scattering targets [20]. Additionally, investigations of UAV-mounted software defined radio (SDR) GPR have previously been examined [21].

In the field of Drone-mounted synthetic aperture radar (SAR), recent studies show the possibility of landmine detection with polarimetric SAR [22] and antenna arrays for GPR systems on drones [23] which yield a wider swath when flying in grid flights, potentially extending area coverage.

This paper presents hardware and software improvements of the UWIBaSS and field results both from altitude experiments (Section 4.2) and snow measurements (Section 5).

## 2. Theory

Perhaps the most central quality parameters when taking snow measurements with radars are penetration depth and spatial resolution. This section will go through the limiting factors these parameters impose on radar sensing of snow.

### 2.1. Penetration depth

The distance an electromagnetic wave travels through a medium before its intensity is reduced by  $1/e$  (about 37%) is referred to as the penetration depth and is used in practice to estimate how microwaves attenuate within a medium.

The EM-wave penetration depth of snow and ice is a function of radar frequency, brine volume, incident angle, temperature, density, liquid water content, snow particle diameter and conductivity of the ice or snow [24].

To determine the penetration depth, the complex dielectric constant,  $\epsilon$ , must be known. The complex dielectric constant is defined by Daniels [25]:

$$\epsilon = \epsilon_0(\epsilon_r' - j\epsilon_r''), \quad (1)$$

where  $\epsilon_0$  is the free-space dielectric constant,  $\epsilon_r'$  the relative dielectric constant, and  $\epsilon_r''$  the relative imaginary dielectric constant. The value of  $\epsilon$  depends on several snow state variables. Predicting the microwave response can be complicated due to the depth gradient of liquid water content and/or salinity concentration within the snowpack, in addition to the frequency dependence of all parameters. Often  $\epsilon$  is simplified and estimated semi-empirically [24,26].

The penetration depth  $\delta$  in a snow or ice medium is controlled by scattering and absorption losses. If scattering losses are assumed to be negligible,  $\delta$  can be expressed as [27,28]:

$$\delta = \frac{\lambda}{4\pi} \left( \frac{\epsilon_r'}{2} \left( \left[ 1 + \left( \frac{\epsilon_r''}{\epsilon_r'} \right)^2 \right]^{1/2} - 1 \right) \right)^{-1/2}, \quad (2)$$

where  $\lambda$  is the wavelength for free space.

Consequently the loss in the medium can be expressed as:

$$L = 10 \log(e^{1/\delta}) \quad [\text{dB/m}]. \quad (3)$$

If  $\epsilon_r''/\epsilon_r' \ll 1$ , which usually is the case for snow, equation (2) is simplified to [27]:

$$\delta \approx \frac{\lambda \sqrt{\epsilon_r'}}{2\pi \epsilon_r''}. \quad (4)$$

Since  $\epsilon_r''$  of water is several orders of magnitude larger than that of dry snow, even very small amounts of liquid water in the snowpack can dramatically decrease the penetration depth  $\delta$ .

The complex dielectric constant of snow and ice can be estimated using both empirical and theoretical models for the real and imaginary parts. Figure 1 shows a comparison of selected models used to calculate penetration depth. The models were collected from:

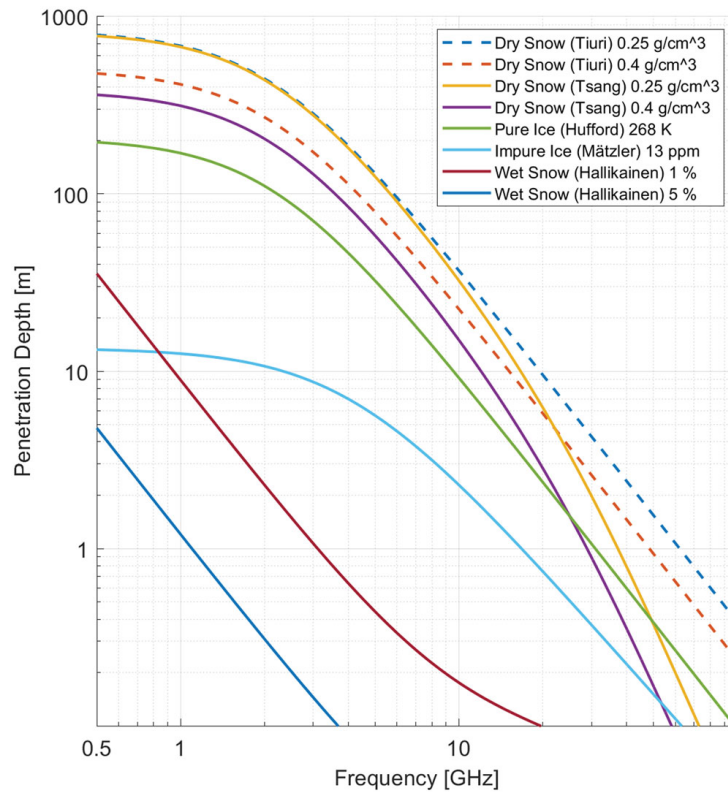


**Figure 1.** Penetration depth at a temperature of 268 K shown as a function of frequency for dry snow with 0.5 mm grain size, wet snow with dry snow density of 0.4 g/ccm, freshwater ice, and impure ice. Dry snow penetration depth is calculated with two different models, where the main difference is that the Tsang model accounts for grain size.

[4,29–35]. The complex dielectric constant of snow has several adequate empirical models [4,31]. However, these models are limited to the low-frequency approximation ( $\approx 1$  GHz) for which the effects of scattering can be neglected. This limitation implies that the low-frequency dielectric constant is not dependent on grain size. The Strong Fluctuation Model for Dry Snow [32] treats snow as a medium of randomly scattered ice particles suspended in a background medium which, in the case of snow, is air.

Penetration depth models for all mentioned media are depicted in Figure 1.

Generally, these media act as low pass filters in the microwave frequency range where lower frequencies penetrate deeper into the medium.

Based on the results from Figure 1, we need a radar system that operates at sufficiently low frequencies to penetrate most snow types and still have a high enough bandwidth (i.e. resolution) to resolve internal layers in the snowpack.

## 2.2. Resolution

The range resolution of a pulse compression radar system is given by Richards [36]:

$$\Delta r = \frac{c}{2B} \frac{1}{\sqrt{\epsilon_r}}, \tag{5}$$



where  $B$  is the effective bandwidth of the radar transmitter and receiver and  $\epsilon_r$  is the complex relative dielectric constant.

Equation (5) shows that the radar system bandwidth is a fundamental parameter of the range resolution and, theoretically, the only factor that can be modified to improve the range resolution significantly. For high-valued dielectric media,  $\epsilon_r$  also has a marked impact on the range resolution. In radar applications, additional factors such as pulse compression, Fourier domain windowing, and image processing methods affect the radar system output range resolution, however, only to a minor degree.

More importantly, the total bandwidth of any radar system also depends on the bandwidth of the transmitting (TX) and receiving (RX) antennas. The radar sensor used in the UWibaSS has a bandwidth of 0.1–6 GHz, which makes the bandwidth of the antennas the main limiting factor for the total bandwidth, as all applied antenna designs have bandwidths that are sub-bands within this bandwidth of nearly 6 octaves.

The next two sections will present technical and software methods to improve on the limiting factors presented.

### 3. Methods: technical improvements

This section presents the recent technical improvements made to the UWibaSS motivated by the limiting factors presented in the previous section. These improvements include antenna re-design and further radar system development that increase the versatility and usability of the UWibaSS.

#### 3.1. Radar system description

The radar system consists of 6 main modules:

- (1) Radar sensor
- (2) Single board computer
- (3) Radio modem
- (4) RF amplifier on TX channel
- (5) Antenna system
- (6) Power handling board, Mavlink serial connection and heating element.

The radar system consists of an ILMsens SH-3100 radar sensor, a Minicircuits ZX60-83LN12+ amplifier for the TX channel, dual Vivaldi antennas in a bistatic configuration and an Odroid XU2 single board acquisition computer. The system is described in more detail in [5], and the new improved antenna system is described in Section 3.3 below. The integration with the UAV is illustrated in Figure 2 where the block diagram of the UWibaSS illustrates synchronization and data transfer between the UAV autopilot as well as antenna angle regulation.

The ILMsens SH-3100 UWB sensor has several desirable characteristics concerning high-resolution radar imaging.<sup>1</sup> Using their own developed m-sequence pseudo-random noise (PRN) signal generator, this sensor performs well for radar sensing tasks, especially when we have restrictions regarding high peaks of transmitted energy commonly associated with pulse radars. Additionally, the use of maximum length binary sequence (MLBS) allows for a

UWiBaSS block diagram

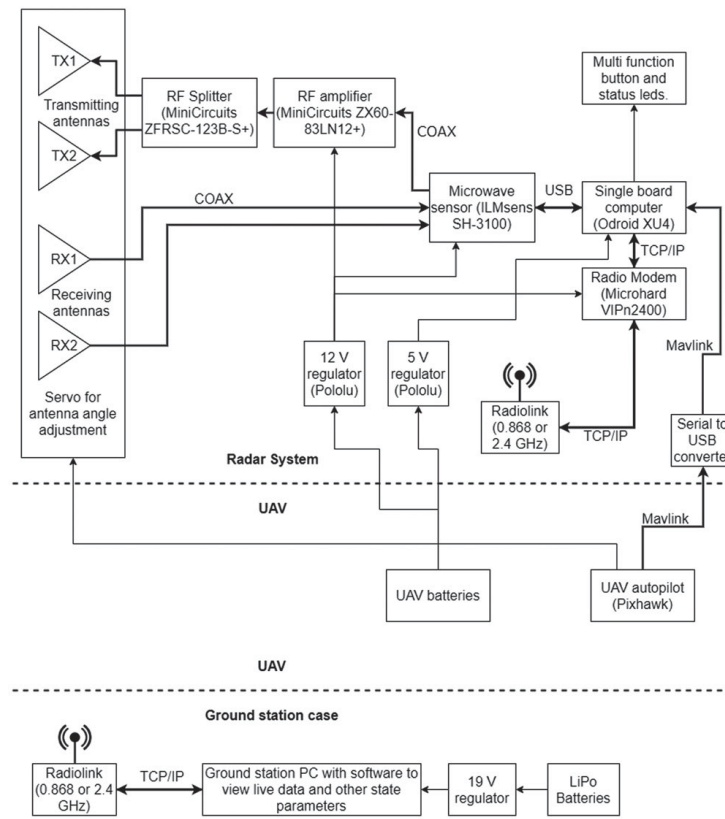


Figure 2. Block diagrams of the UWiBaSS.

single frequency oscillator, thus reducing clock jitter. The sensor has a transmitter channel and two receiver channels working in parallel.

Table 1 describes the key characteristics of the radar system. The bandwidth is the combined bandwidth of the sensor and the antennas. Thus, the resolution is the measured Full Width at Half Maximum (FWHM) distance of a processed radar pulse.

The radar sensor is used in conjunction with four linearly polarized transceiving antennas mounted in pairs as RX and TX arrays, a concept described in more detail in Section 3.3.

### 3.2. UAV platform

The UAV used to carry the UWiBaSS is a purpose-built X8 multicopter called “Fox”. The “Fox” uses four 12 cell 88Ah Li-Po batteries and can lift a maximum payload of 25 kg. Each of the eight engines (U11, 120KV) has a maximum rated thrust of 12.3 kg using 27” propellers. For navigation and control, a “Cube Black” running “Arducopter” is used. It is set up with a “Here+” real-time kinematic (RTK) global positioning system (GPS),<sup>2</sup> providing significantly more accurate position estimates than regular GPS devices. In single-channel mode with less than 20 km distance to the base station, the positioning system has relative and absolute accuracy better than 10 cm and 1 m, respectively. Additionally, an SF11<sup>3</sup> laser rangefinder accurately measures the distance to the ground. This also provides

**Table 1.** UWibaSS key characteristics.

Attribute	Value
Signal generation	UWB Pseudo noise
System bandwidth	3.8 GHz (0.7–4.5)
Range resolution	≈ 5 cm
m-sequence clock frequency	13.312 GHz
Measurement rate	52 Hz (max 1000 Hz)
MLBS order	9 (511 range bins)
Nominal output power	17.3 dBm
Unambiguous range in air	5.9 m
Average power consumption	8.1–9 W
Total Weight	≈ 3 kg
Transmitter	
No high voltage peaks	
Low field strength operation	
Power splitter into Dual Vivaldi antenna prototype	
Receiver	
Continuous, synchronous sub-sampling operation	
Timebase jitter less than 20 fs (rms)	
Dual Vivaldi prototype with each antenna	
Element into separate channel	

autonomous flights that has been used in data collection for the field campaign described in Section 5.

### 3.3. Antenna improvements

The UWibaSS has been tested with several different antenna configurations: Using RX and TX spiral antennas [37], a combination of Vivaldi and spiral antennas [5] and currently dual, modified Vivaldi antennas in a bistatic configuration. With the latter configuration, we add a transversal dimension to the otherwise planar antennas. This focuses the antenna beam along the most de-focused axis (H-plane), significantly improving overall antenna directivity compared to a single element (see Figure 4). In addition to the dual antenna configuration, the Vivaldi antennas have inserted slits to shift the effective bandwidth to lower frequencies while keeping a small form factor [38]. Additionally, the antennas are modified with a printed lens in the aperture to increase gain and reduce side-lobe levels [39]. Finally, the inserted slits have also been modified with resistive loads in the opening of the slits to dissipate the current distribution occurring at the sides of the antennas. This modification reduces ringing from residual energy not radiated by the antenna at the front aperture. It was found, through simulation, that a resistor value of approximately 1 k $\Omega$  is optimal. Figure 3(a) shows a close-up photo of the modified Vivaldi antenna with inserted slits, printed lens in aperture, and resistive loads.

The spacing between the antennas was optimized through simulation. The ideal distance for a 0.7–4.5 GHz bandwidth was found to be about 11 cm.

Figure 3(b) shows the two sets of Vivaldi antennas mounted in a bistatic configuration with approximately 50 cm spacing between the pairs. The TX signal is distributed to the two Vivaldi antennas using a 2-way power splitter. The radar system has two RX inputs enabling a direct connection with each RX antenna. The antenna mounting is entirely 3D printed resulting in a lightweight, easy to manufacture and nearly electrically neutral part.

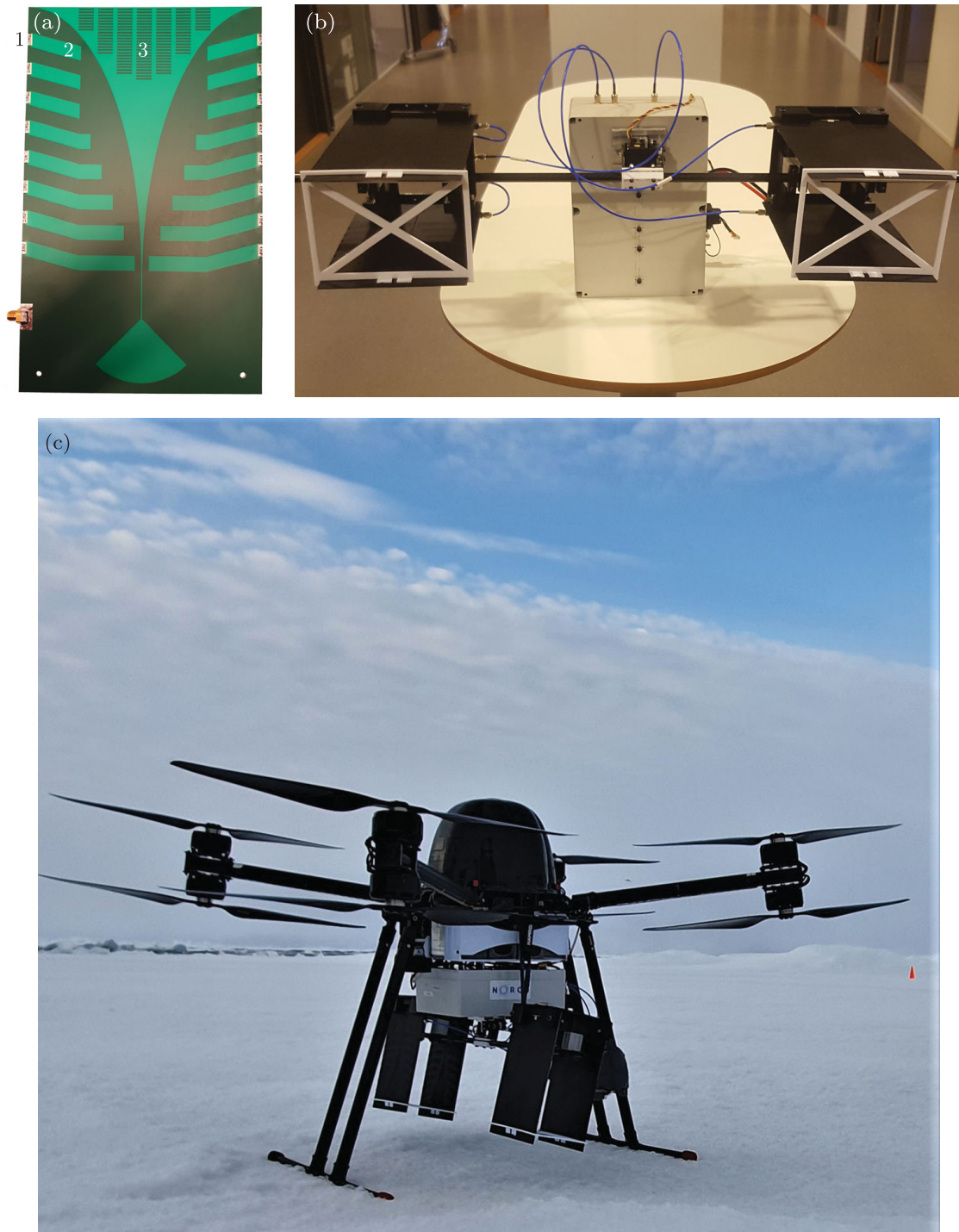


**Figure 3.** Close up of Vivaldi antenna (a), radar system with dual Vivaldi antennas (b), and the same radar system mounted under a UAV (c). (a) Close-up of modified Vivaldi antenna, with resistive loads (1), inserted slits (2) and printed lens in aperture (3). (b) Dual Vivaldi antennas mounted in bistatic configuration (painted black) and (c) Antenna prototype (and radar box) mounted under “Cryocopter FOX”. The antenna angle regulation mechanism have a slight angle when not powered up, to keep tension on stabilizing bungees when pointing in nadir.

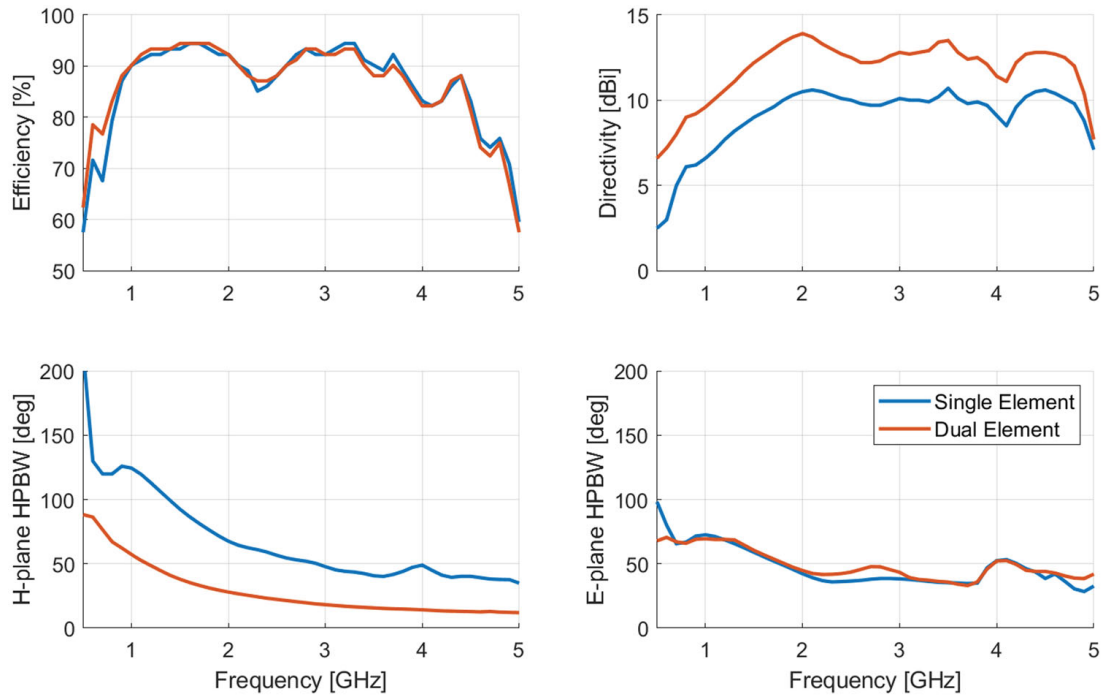


**Figure 4.** Simulated antenna parameters.

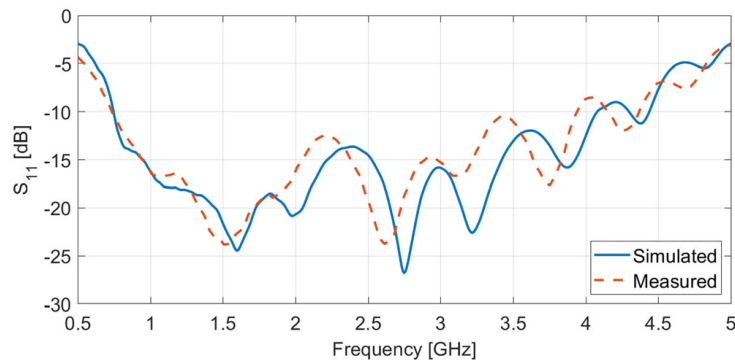


**Figure 5.** Simulated and measured return loss for the modified Vivaldi antenna.

Simulations of the antenna array configuration was performed in CST microwave studio suite,<sup>4</sup> and is shown in Figure 4. The simulations show approximately 3 dBi increased directivity across the frequency range, and a significant reduction in half power beam width (HPBW) in the H-plane beam compared to a single element antenna. The increase in directivity is similar to the directivity of a dipole in the H-plane. Simulations also show little change in the antenna efficiency and the same  $S_{11}$  (Figure 5) if we assume ideal power splitting and that parasitic effects between the dual elements are negligible. Comparing the simulated and measured  $S_{11}$  in Figure 5 shows a slight shift downwards in the band. This might be due to the dielectric effect of the antenna silkscreen not included in the simulation. Additionally, we have installed an RF amplifier (Minicircuits ZX60-83LN12+) that increased the nominal output power from  $-7$  dBm to 17.3 dBm. These improvements are all motivated by increasing the penetration depth and effective observation range of the radar system.

**Table 2.** Comparison of single Vivaldi antenna and dual modified Vivaldi antenna.

Antenna configuration	Single	Dual with slits
Bandwidth	0.95–6 GHz	0.7–4.5 GHz
Penetration depth <sup>a</sup>	9.7 m	18.2 m
Theoretical range resolution	2.97 cm	3.94 cm
Directivity at 2 GHz	10.5 dBi	13.9 dBi

<sup>a</sup>Calculated at lowest frequency in bandwidth for snow with 1% liquid water content (LWC).

A servo-based antenna angle regulation mechanism was designed to enable measurements in slanted terrain as well as working to stabilize the antenna from UAV movement. The angle regulation mechanism can be set to keep a specific angle and use the UAV gyroscope to regulate that angle relative to the UAV movements; however, only along one axis. When performing surveys over flat terrain, the angle regulation mechanism points the antennas in nadir. Furthermore, the UAV has retractable feet minimizing clutter from the UAV air-frame.

Table 2 compares the dual Vivaldi antenna configuration with the single Vivaldi antenna configuration used on the previous iteration of the radar system. In addition to the dual configuration, the new Vivaldi antennas have inserted slits which effectively shifts the bandwidth of the antenna downwards. As seen in Table 2, the antenna bandwidth is also reduced by approximately 1.25 GHz resulting in approximately 1 cm degraded range resolution. However, the penetration depth for wet snow is almost doubled with this configuration.

### 3.4. Other improvements

The radar sensor and radio modem have been modified with 3D printed enclosures to reduce weight. This modification results in a weight reduction of 75% compared to the original aluminum housings. The 3D printed enclosures were coated in conductive paint to provide RF shielding. Further, the Odroid XU4 can read the Mavlink data stream coming from the UAV autopilot and store relevant data such as altitude, heading, speed, and position, together with the pre-processed radar data.

Direct connection to the UAV batteries produces significant noise due to the high variation in current draw from the speed regulators. The power handling board allows the radar system to accept a direct connection to the batteries using power filtering and regulation to 12 and 5 volts. The radar system now accepts 12–48 V at the power input.

The 868 MHz radio modem generates a network link between the ground station PC and the single board computer onboard the UAV. This enables full control of the radar system while airborne, as well as monitoring of the status of the radar system such as temperature and analog-to-digital converter (ADC) levels. Additionally, when using a higher bandwidth modem (e.g. 2.4 GHz), real-time processing and live stream of the radar image is enabled.

## 4. Methods: software improvements

This section will briefly go through the processing steps of the radar data, before presenting a method on how to measure outside the unambiguous range with this kind of radar, as well as presenting a calibration procedure to remove the effect of varying altitude.

### **4.1. Radar data processing**

With limited antenna isolation owing to UAV mounting restrictions, the main focus of the processing is to remove antenna cross-talk and improve signal to noise ratio (SNR). The first technique applied to the radar data is the match filter processing performed on each received A-scan by cross-correlating the received signal with a locally stored sequence matching the transmitted sequence. This cross-correlation is stored locally on the radar control computer.

The post-processing procedure involves subtracting a reference measurement, normally a measurement from a flight well above the unambiguous range of the radar, or subtracting the slow-time mean of the entire B-scan to only look at dynamics in the data.

The signal then undergoes an FFT Hanning-windowing procedure, Hilbert transform windowing and is finally interpolated to fit the range relative to the propagation velocity in the medium under investigation. In the case of snow, the distance to the air-snow interface is first measured by processing the radar data as if the intermediate propagation medium for the radar signal was air, which is then changed at the identified air-snow interface.

The detection of the first interface can be done automatically or manually, depending on the overall SNR in the data. If the data is very noisy (i.e. from high altitude measurements, say above 20 m), the automatic detection procedure has problems detecting the correct interface which often is visible to the human eye.

Additional image processing methods such as Wiener filtering is used to reduce speckle, and contrast stretching can be applied to increase the contrast in the image for ease of interpretation.

The pre-processed image will be influenced by the varying altitude of the UAV. When the UAV is in "altitude hold" mode, the altitude variation according to the laser altimeter (and the first reflection in the radar image) is approximately 40 cm. Therefore, it could be beneficial to rectify the image based on the laser altimeter. If altimetric data are available from the UAV-mounted laser altimeter, the air-snow interface reflection is corrected for the altitude variation. Figure 6 shows a segment of a transect before and after altitude correction. The top surface of the snowpack is treated as flat for the purpose of measuring snow depth. The shifting procedure is a circular shift at each A-scan according to the laser altitude taken at the closest timestamp.

The processing steps of the altitude correction shown in Figure 6 can be listed as follows:

- Associate each A-scan with a laser altitude measurement using corresponding timestamps.
- Find closest index of laser altitude in radar range vector. Effectively converting laser altitude to radar range-bin position.
- Circularly shift each A-scan according to the converted laser altitude.

### **4.2. Measuring outside the unambiguous range**

The output m-sequence signal generated from this sensor is a pseudo-random sequence that is correlated upon reception. One of the drawbacks of this waveform is that it is strictly periodic and cannot be delayed/range-gated to move the unambiguous range further down range. This results in an unambiguous range that depends on the sequence

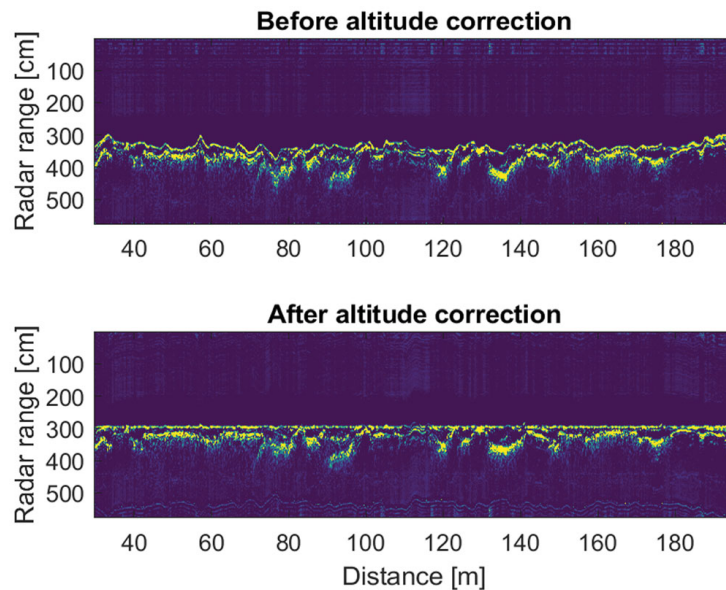


**Figure 6.** Example radar image before and after altitude correction.

length and clock frequency (Equation (1) in [5]). The longer the sequence length, the longer the unambiguous range. However, the data size for each sequence will also increase and results in a reduction in measurement rate, if the processing power is not changed. For future “fixed-wing” UAV UWaSS applications, ground speed and altitude will increase significantly compared with multi-rotor UAV. Therefore, we need a method to increase the range of the radar system while keeping the measurement rate as high as possible.

After reception, the received signal goes through a match filter process. If we consider the case of a single target moving down range from the radar, when the target moves to the end of the unambiguous range, it becomes wrapped around to the beginning of the radar range. We e.g. have a radar system with 10 m unambiguous range and a target at 12 m; in theory, the target should appear at 2 m after the match filter procedure. This is due to the inherent cyclic property of convolution using the discrete Fourier transform (DFT) in match filter processing, and can not be avoided. For drone-mounted GPR, where there usually is air between the antennas and the target (ground), we can assume that in most cases the air will appear as a homogeneous medium with little attenuation and marginal clutter. In this situation, we can perform measurements with the radar system while the target is outside the unambiguous range. This idea was tested in a field campaign on Svalbard 2019, where Figures 7 and 9 show that the radar system is able to measure the snow depth at altitudes far beyond the unambiguous range. We also observe that the received power decreases according to the radar equation (Figure 8), which will eventually limit the range of the radar system due to a smaller SNR with distance.

We could define a window; “Ambiguity window” in which our target should be contained such that it does not wrap around to the next window. As long as the path to the target is not obstructed, little or no clutter will be present. For the UWaSS the 3 first windows are defined in Table 3.



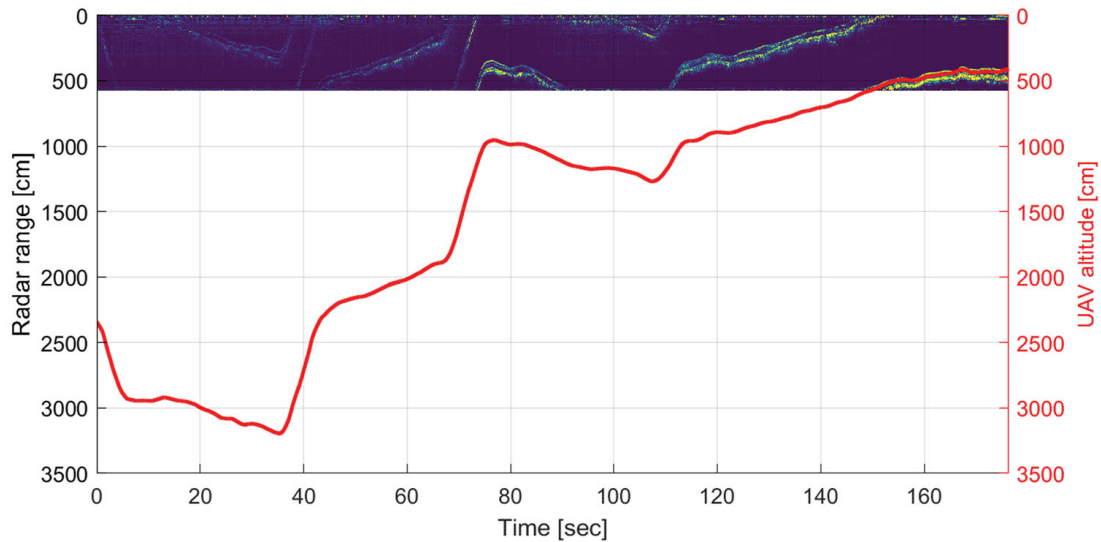


**Figure 7.** Example showing radar image and UAV altitude with the UAV mostly flying outside the unambiguous range, and entering the ambiguous range at approximately 150 s.

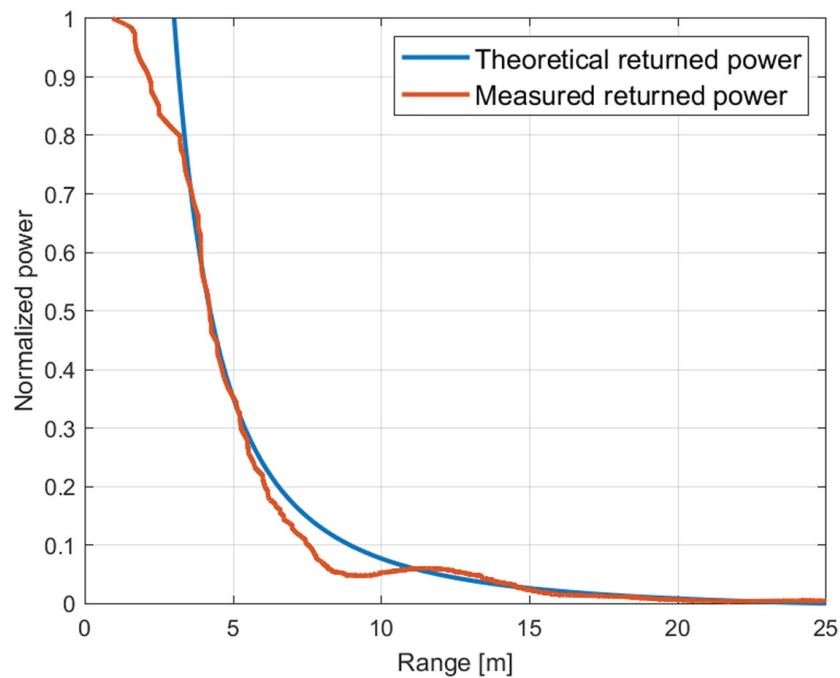


**Figure 8.** Returned power compared to the theoretical returned power according to the radar equation. Data was collected with a drone-mounted radar with a max unambiguous range of 5.7 m.

To avoid ambiguities in the measurements, the radar system is used in conjunction with a laser rangefinder. The rangefinder does not need high resolution for the purpose of identifying which window our target is within. Nevertheless, high resolution is needed for the altitude correction and the calibration procedure presented later in this paper.

The advantage of measuring outside the unambiguous range is that we can use sensors with short-windows which benefit from high measurement rate and less unnecessary data (e.g. data used to describe propagation in the air). However, one of the drawbacks of using

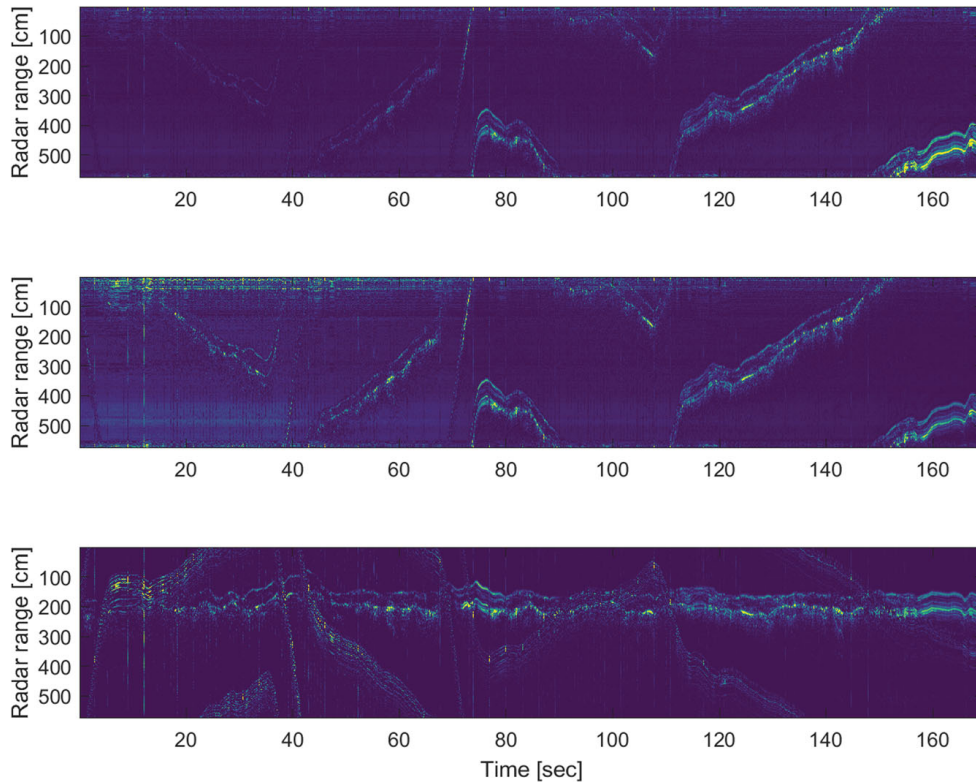


**Figure 9.** The same data as in Figure 7, before any correction (top) after altitude dependent power calibration (middle) and finally after the shifting procedure (bottom).

**Table 3.** Ambiguity windows.

Window number	Start of window	End of window
1	0 m	5.7 m
2	5.7 m	11.4 m
3	11.4 m	17.1 m

a shorter shift registry for the m-sequence is that this raises the noise floor [5]. Additionally, if the target length (in this case, the snow depth) is longer than the unambiguous range, the measured profile will overlap, thus complicating the interpretation.

Other studies show similar results for CW radars. Albanese and Klein [40] have shown that using two code clocks can extend the unambiguous range. Zhang et al. [41] demonstrated a similar solution to range ambiguity using FMCW signals in combination with two-tone CW signals to obtain high precision range measurements with SDR.

The major drawback of using CW radars beyond the unambiguous range are that one can not increase the output power indefinitely. In a bistatic CW radar, the RX antenna is always receiving and if the TX power is too high, the receiver electronics can be saturated or even blown by the antenna crosstalk. This can, in principle, be solved by using range gated radar systems [10].

Figure 7 show an example data-set chosen for high variations on altitude. This case can be considered extreme since the UAV normally maintains a somewhat stable altitude (e.g. Figure 6) during data collection. However, this example was chosen to illustrate how the processing method works.

From Figures 7 and 8, we can construct a calibration procedure that shifts and calibrates each A-scan according to the laser altimeter. The shifting procedure is the same method as shown in Figure 6. Calibration involves multiplying each slowtime vector (corresponding to a laser altitude) with the range dependence from the radar equation. In this case, we are using the special variant of the radar equation for flat surfaces [42]. The calibrated pixel value in terms of power  $n_c$  becomes:

$$n_c = n(4\pi)^2(2R_{alt})^2, \quad (6)$$

where  $n$  is the non-calibrated pixel value in terms of power and  $R_{alt}$  is the radar altitude. This calibration procedure results in pixel values that are independent of altitude and mostly depend on the changes in dielectric constant at different media interfaces.

Figure 9 show an example of how to process the radar data such that we can measure outside the unambiguous range. Notice in the bottom image in Figure 9 that the crosstalk varies as the inverse of the radar altitude. Improved crosstalk rejection will mitigate this. Also, notice that the rectification is far from perfect regarding the air-snow interface. This is due to the different mounting positions of the UWibaSS and the laser altimeter on the UAV resulting in different responses to small angles when the UAV tilts. The most apparent variation occurs when the UAV has rapid changes in altitude, which should be avoided in normal data collection scenarios. Additionally, inaccuracies in the laser altimeter play a small part. Nevertheless, this result can be used in further analysis and image improvement.

A comparison of the pixel variance before and after the calibration procedure is shown in Figure 10, where the variance stays significantly more constant in the calibrated image. However, a slight increase in variance is shown as altitude rises. This is because we are introducing more noise to the image with this calibration. With this calibration procedure, the variation in the received radar signal due to the radar altitude is almost removed. This procedure could be used to estimate the density, and possibly the dielectric constant for dry snow if we can ignore the imaginary part of the dielectric constant.

The antenna crosstalk is not that trivial to remove when facing UAV mounted radar. This is due to both variable radio interference influencing the entire image, but mostly due to vibrations and moving parts close to the antennas (such as UAV landing gear). This leads us to altitude windows we could recommend the pilot to stay inside to keep the cross talk in a different image region than the target. Due to moving landing gear, or other small moving parts relatively close to the antennas, we can, in general, say that we should have the target at least 1 m down range from the cross talk, regardless of what ambiguity window we are in. We must also consider the approximate depth of the target to avoid having the target move into the next window. From this general rule, we can create regions of preferred altitude  $a$  for the pilot to stay inside.

$$a = [R_u(W - 1) + 1]R_uW - T, \quad (7)$$

and

$$W = \text{floor} \left( \frac{R_{alt}}{R_u} \right) + 1, \quad (8)$$

where  $R_u$  is the unambiguous range of the radar,  $W$  is the “ambiguity window” number,  $T$  is the expected length of the target, *floor* is a function that returns the greatest integer less

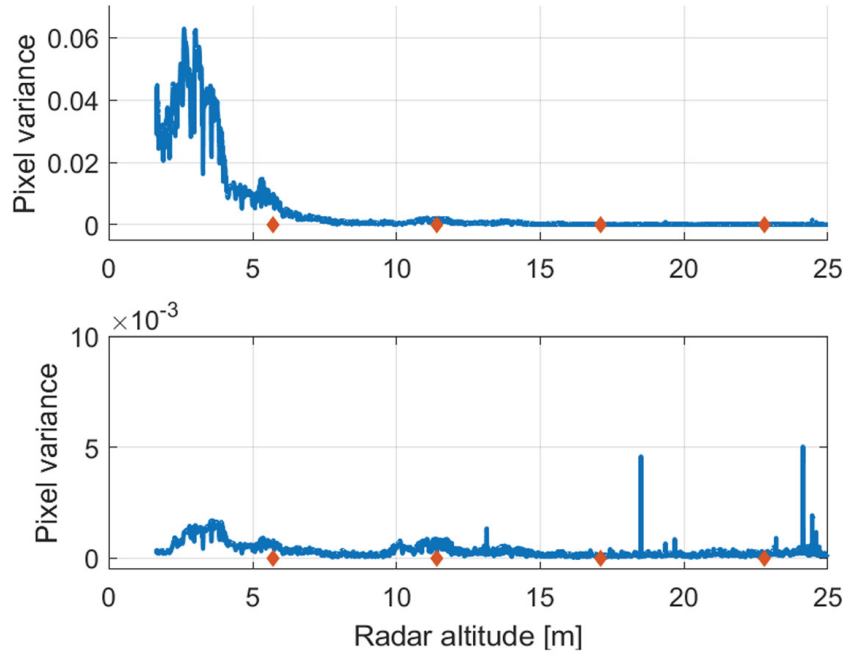


**Figure 10.** Pixel variance of the un-calibrated (top) and range calibrated (bottom) radar image. Ambiguity windows are marked with red diamonds.

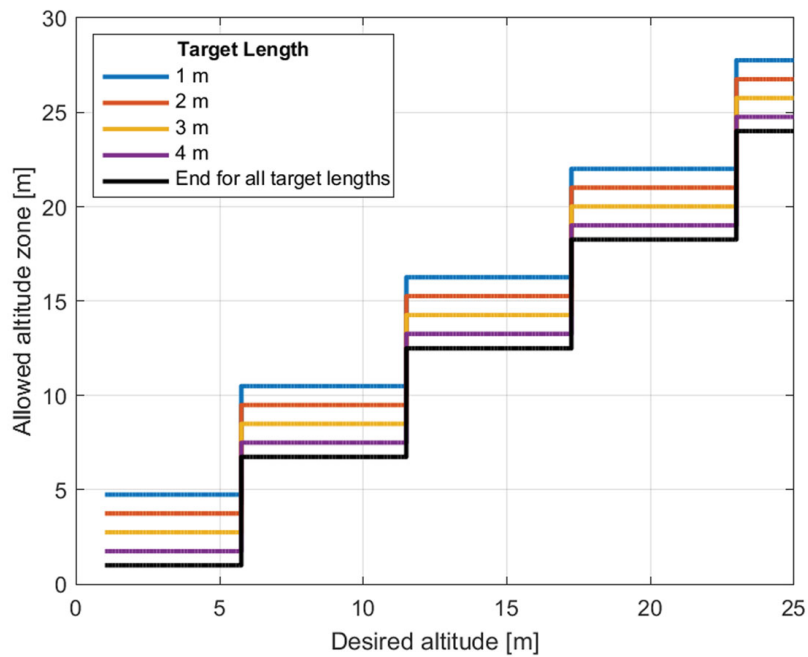


**Figure 11.** Chart of preferred zones of altitude given different target lengths. This is calculated for a radar system with 5.75 m unambiguous range.

than or equal to the input and  $R_{alt}$  is the approximate altitude the UAV is to fly in (e.g. 5, 10 or 15 m). This rule is visualized in Figure 11 for a radar system with 5.75 m unambiguous range and target lengths (i.e. snow depths) of 1,2,3 and 4 m. From this figure, we can see that the longer a target is, the shorter is the preferred range for the UAV to fly in.

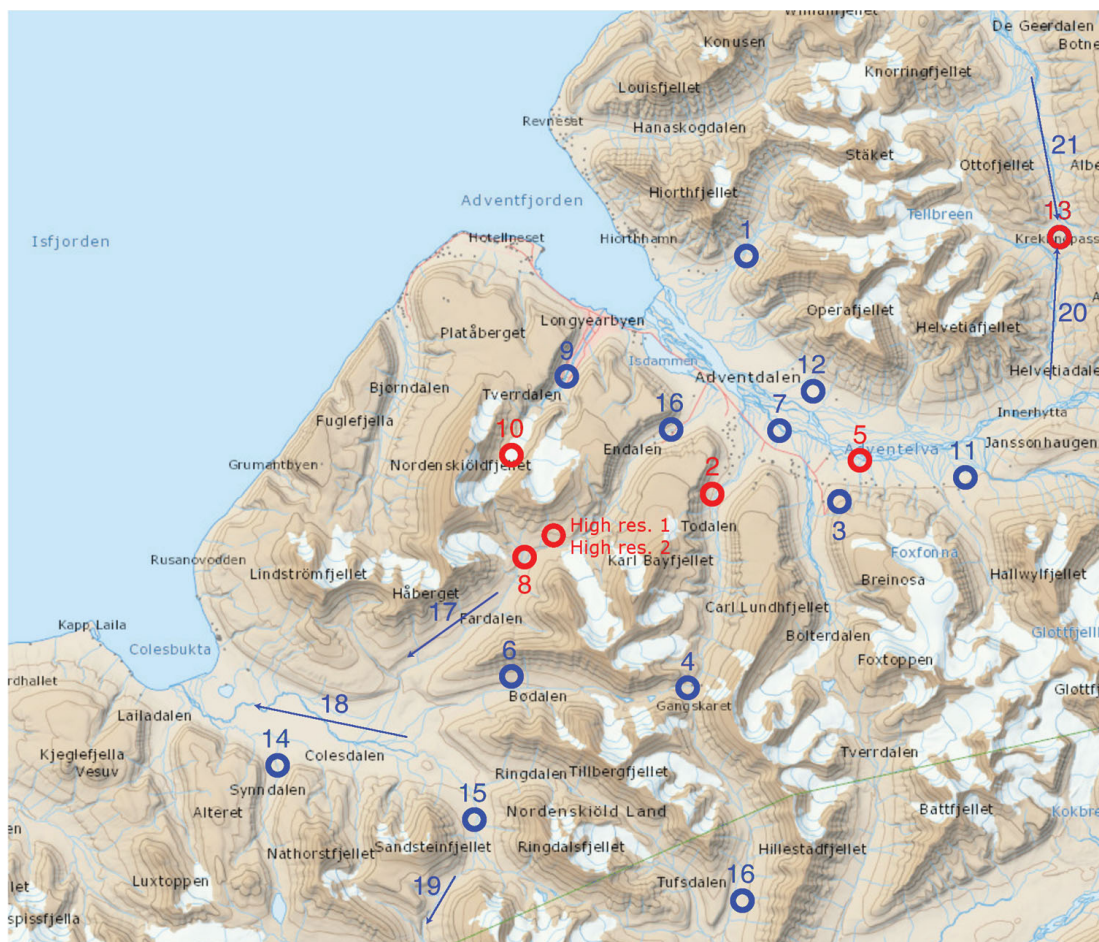


**Figure 12.** Map of SIOS field locations. Sites visited on the current campaign is marked in red.

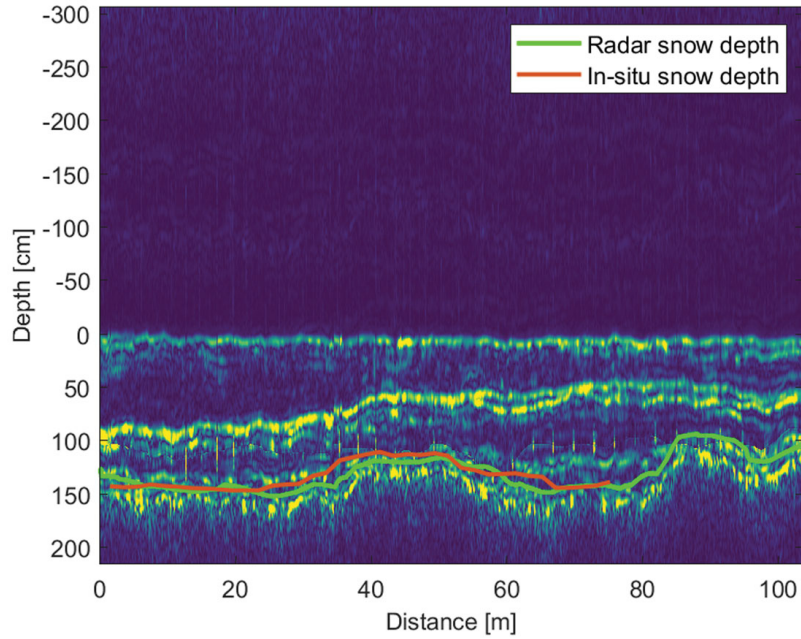
## 5. Field results

In this section, we present results from a field campaign conducted in 2019 on Svalbard. We make comparisons against both *in situ* measured depth as well as *in situ* stratigraphy.

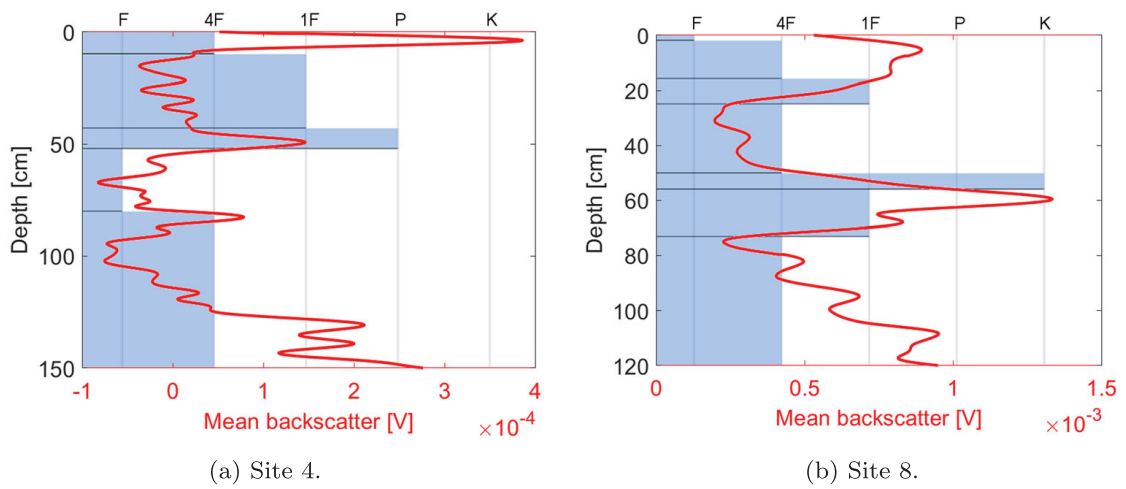
During March 2019 we conducted a 7-day campaign in the area around Longyearbyen – Svalbard. This campaign focused on snow depth measurements over approximately  $100\text{ m} \times 100\text{ m}$  grids. The grids were scanned with the UWibaSS mounted on the Cryo-copter FOX UAV and manually measured using the Snow-Hydro GPS snow depth probe,<sup>5</sup> and in “High res. 1” and “High res. 2” with standard avalanche probe and handheld GPS (see Figure 12). This field campaign was carried out as a part of the Svalbard integrated arctic earth observing system (SIOS) project to monitor snow cover on Svalbard.

21 field locations were defined to do recurring measurements over a 5 year period. Due to time limitations and avalanche safety restrictions though, only some of the sites were visited during the 2019 campaign and these are marked red in Figure 12. On each site, a  $100\text{ m} \times 100\text{ m}$  grid with 10 m spacing between transects was selected for snow depth survey using the UWibaSS mounted on UAV and also using GPS snow probe.

The UWibaSS data can be displayed as a 1D (A-scan) snow profile as seen in Figure 14 or as a 2D cross-section (B-scan) of the snowpack as seen in Figure 13. Additionally, the depth



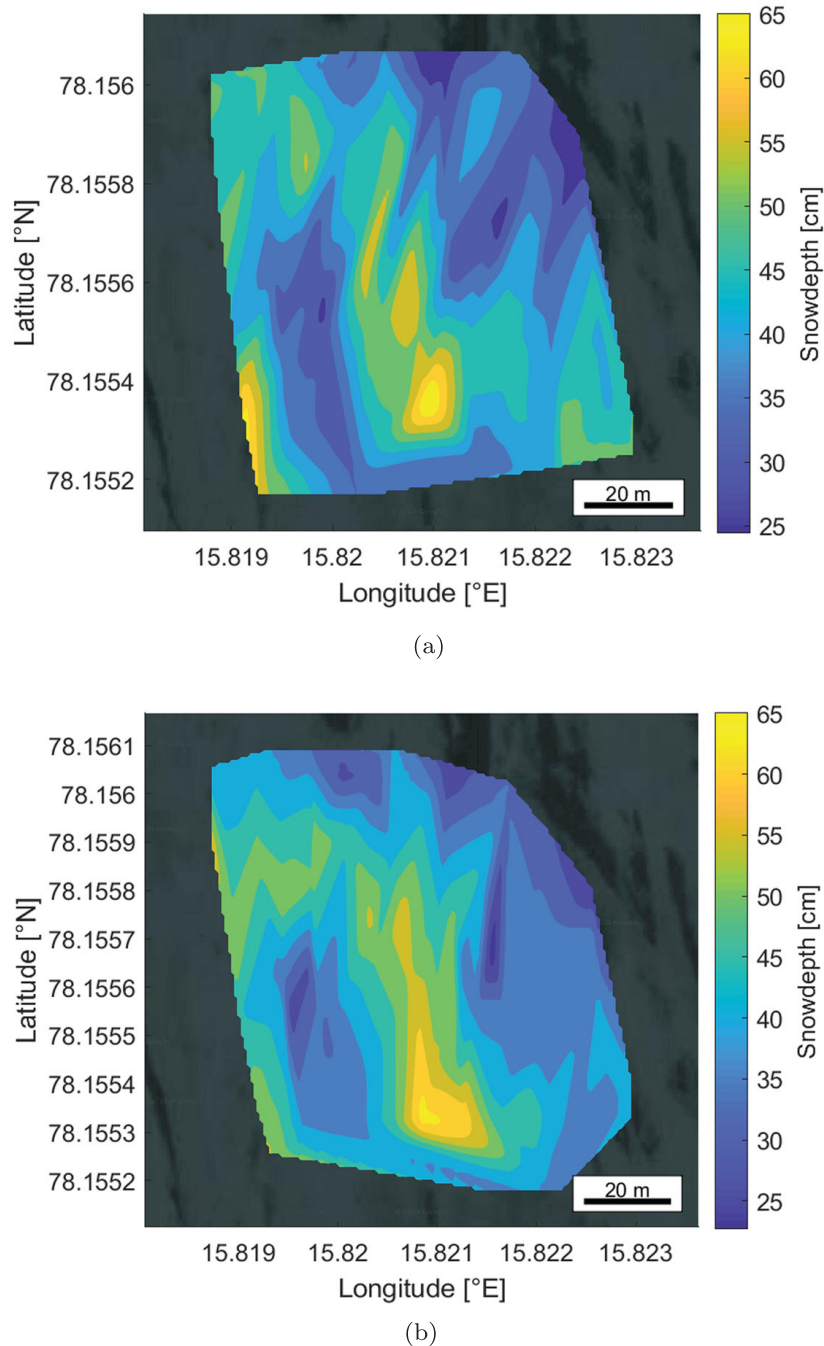
**Figure 13.** B-scan radar image from site “High res. 1”, with interpreted radar snow depth compared with *in situ* snow depth. The radar measurement is a 100 m transect with 38 manual measurements over nearly 80 m. All data points are geo-referenced.



**Figure 14.** A-scan radar responses in red (150 slow time averages), compared to *in situ* stratigraphy in blue, assessed using the “hand test” [43] shown with the top x-axis. (a) Site 4 and (b) Site 8.

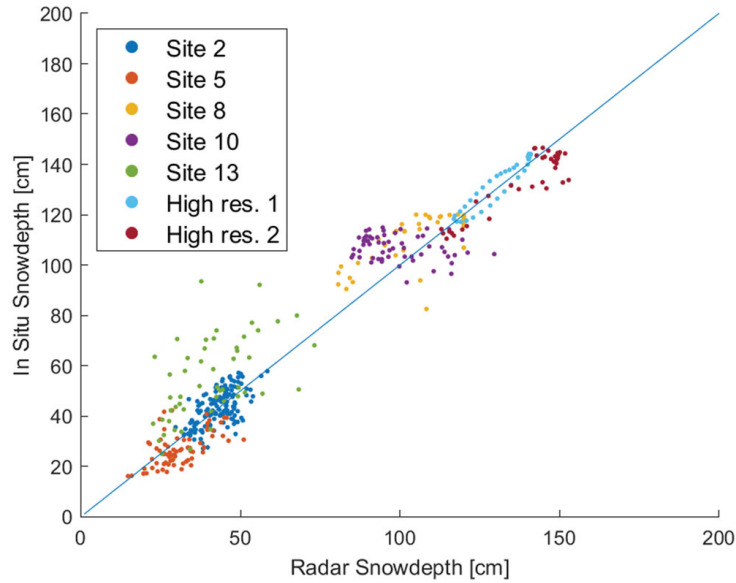
measurements obtained with the UWibaSS can be combined with the GPS data from the UAV to make snow depth maps that can be overlaid onto maps, as seen in Figure 15.

Figure 13 shows the B-scan radar image from a 100 m transect with nearly 80 m of *in situ* depth measurements. The data has been georeferenced and plotted together. The radar measurements were performed at approximately 8 m altitude above the snow cover. Hence, the original data before laser range correction had the snowpack overlapping two “ambiguity zones”. The crosstalk zone is noticeable as a thin line of noise at approximately 100 cm in Figure 13.



**Figure 15.** Georeferenced snow depth from site 2, measured with drone mounted radar (a) and GPS snow probe (b).  $C = 0.67 \pm 0.01$  and root-mean-square error (RMSE) = 5.9 cm. (a) Radar snow depth and (b) *In situ* snow depth.

Figure 14 shows *in situ* stratigraphy compared with the radar response from an area close to the snow pit. The *in situ* stratigraphy was collected using the “hand test” for assessing snow hardness [43]. The top peak in the radar response is a combination of the air-snow interface and internal variations at the top of the snowpack. The middle peaks correlate with the distinct internal layers in the snowpack. The bottom also gives a distinct response in the radar image, while the *in situ* profile does not mark that transition.



**Figure 16.** In-situ snow depth vs. radar snow depth for all sites. Spatial correlation:  $C = 0.97 \pm 0.01$  and RMSE = 10.6 cm.

In Figure 13, we can identify the top and bottom interfaces automatically or manually. This depth data are then referenced to the range vector that is calculated based on the propagation velocity for each medium. The depth data from each B-scan are then associated with a GPS coordinate and can be displayed as a contour map on top of existing maps. This can be useful for estimations of total snow volume or finding areas with varying snow cover.

Figure 15 shows a  $100\text{ m} \times 100\text{ m}$  grid of georeferenced depth measurements by the radar and compared to *in situ* depth. The depth estimations are interpolated into a surface and overlaid on a map where some correlation with the features in the surrounding image is seen (e.g. Rocky parts in the map correlates to areas with low snow depth). The depth measurements in Figure 15 are correlated with *in situ* depth in Figure 16 marked in blue.

Finally, Figure 16 shows combined spatial snow depth correlations for all sites visited, where each *in situ* depth measurement is correlated to its closest radar depth measurement based on the GPS positions of the GPS probe and UAV. In “High res.” 1 and 2 we used manual depth probes for the depth measurements, while in the other sites we used the GPS probe. The max depth for the GPS probe is 120 cm, hence, radar snow depth measurements were thresholded at 120 cm for the sites where the GPS probe was used. However, for the “High res.” 1 and 2 transects, a standard avalanche probe was used, and coincidentally the snow depth was up to 153 cm at those sites.

## 6. Discussion

One of the main challenges of snow measurements with radar is sufficient penetration depth. The latest iteration of the antennas for the UWibaSS is using different methods to obtain acceptable penetration depth for snow sensing tasks. More power is concentrated on a smaller footprint by increasing antenna directivity and transmitted power.



Additionally, by shifting the radar system bandwidth down from 0.95–6 GHz to 0.7–4.5 GHz, penetration depth in the snow has been increased further.

Furthermore, a range calibration procedure removes the influence of distance to the target. When the range variability is removed, density will mainly govern the amount of back-scattered power (for dry snow). Grain size and surface roughness also influence the returned power, however, for the frequency domain of the UWibaSS, we might be able to ignore those parameters for coarse density estimation. Figure 9 shows how the calibration procedure alters the image. Notice the weak returns at the start of the image become more clear, but at the expense of more noise.

Results from the Svalbard campaign further confirm that UWibaSS is a capable snow measurement system, and the improved antenna system significantly improved the platform stability as well as the dynamic range in the received data.

The antenna system should be upgraded to a 2 axis angle adjustment mechanism to further stabilize the antennas from UAV movement. However, stabilization in one axis significantly improved the overall stability of the antennas.

The UAV with antennas was tested in winds up to 15 m/s without any significant issues regarding flight or influence from the antennas in the wind. Additionally, the UWibaSS was tested at the maximum speed of the UAV, approximately 21 m/s, with no noticeable degradation due to vibration. However, with fewer measurements to average over for each position when the UAV speed increases, the noise level is expected to increase.

A comparison between the A-scan radar response and the *in situ* snow stratigraphy in Figure 14 shows an agreement regarding the layers contained inside the snowpack. One should note that the radar signal have strong reflections at the ground surface which is not considered in the *in situ* case. Additionally, the transition from air-to-snow also gives a strong response not taken into account in the *in situ* stratigraphy. Looking at Figure 13, the stratigraphy is dynamic even at sub 10 m distances. Hence, ideally, the radar measurement should be taken as close as possible to the *in situ* snow pit. In the case of Figure 14 the *in situ* profile was taken approximately 2 m from the radar transect.

Figure 15 shows good agreement between the radar and *in situ* depth mapping. As seen in Figure 16, similar spatial correlations were found for the remaining sites.

Comparing the radar and *in situ* depth yields a correlation coefficient of  $0.97 \pm 0.01$  and RMSE of 10.6 cm, which are amongst the highest reported correlations compared to other studies in the literature [6–8,11]. The correlation given by the depth measured by the GPS probe (e.g. Figure 15) compared to the high resolution transects (e.g. Figure 13) is significantly lower as seen in Figure 16. That leads us to believe that other factors such as GPS accuracy and the low resolution in the *in situ* measurements also influence the correlation coefficient. This is mainly due to the high variability of the snow depth caused by the dynamic terrain below, which is not captured by the low resolution *in situ* measurements. The RMSE is reduced to 5.8 cm if we only consider the sites where the manual snow probe was used (High res. 1 and 2). These measurements were also the deepest depth measurements with values up to 153 cm.

## 7. Conclusion

In this paper, we have presented improvements to the UWibaSS radar system. This includes new and improved antennas and signal processing techniques.

The improved directivity of the new Vivaldi array improves the ability to penetrate snow and to measure with a smaller antenna footprint at higher flight altitudes.

Using a calibration procedure to compensate for the altitude in the radar data allows for the extraction of other pieces of information from the back-scattered signal. Potentially, one could find a relation between back-scattered power and snow density. This will be investigated in future work.

A major challenge in the verification of such a system is the high variability in the snow-pack, which is detected by the radar system, but not always by the *in situ* measurements due to the coarse spacing of manual measurement points. This is evident when comparing the correlations gained from the high resolution transects with the more coarsely spaced measurements performed with the GPS probe.

The system could be used to accurately estimate total snow volume, mass or snow water equivalent (SWE) using local density measurements. Future work includes investigating methods to extract the dielectric constant from snow data in order to establish the snow water equivalent by radar only. Additionally, the radar system will be mounted on a fixed-wing UAV to extend area coverage. For this application, the method to perform measurements outside the unambiguous range will be useful.

## Notes

1. Visit the ILMsens website at <https://www.ilmens.com/products/m-explore/>
2. For more information about "Here+" RTK GPS visit: <http://ardupilot.org/copter/docs/common-here-plus-gps.html>
3. For more information about SF11 visit: <https://lightware.co.za/products/sf11-c-120-m>
4. For more information about CST visit: <https://www.3ds.com/products-services/simulia/products/cst-studio-suite/>
5. For more information about the GPS snow depth probe, visit: <http://www.snowhydro.com/products/column2.html>

## Disclosure statement

No potential conflict of interest was reported by the author(s).

## Funding

This work was supported by the Research Council of Norway under the project Svalbard Integrated Arctic Earth Observing System (SIOS) – Infrastructure development of the Norwegian node (Grant No. 269927); and the Centre for Integrated Remote Sensing and Forecasting for Arctic Operations (CIRFA) partners (Grant No. 237906); and NORCE Norwegian Research Centre (Grant No. 261786); Norges Forskningsråd.

## Notes on contributors

**Rolf Ole Rydeng Jenssen** received the B.Sc. degree in automation and the M.Sc. degree in applied physics and mathematics, with a focus on snow stratigraphy measurements with ultra-wideband radar, from the University of Tromsø-Arctic University of Norway, Tromsø, Norway, in 2014 and 2016, respectively. Since 2017, he has been a Ph.D. Fellow with the Centre for Integrated Remote Sensing and Forecasting for Arctic Operations (CIRFA), Tromsø, where he is involved in unmanned aerial vehicle remote sensing for Arctic applications such as monitoring of snow and sea ice conditions.

**Svein Jacobsen** (M'02–SM'07) was born in Norway in 1958. He received the B.Sc. and M.Sc. degrees and the Ph.D. degree in microwave sensing of the ocean surface from the University of Tromsø, Tromsø, Norway, in 1983, 1985, and 1988, respectively. From 1985 to 1986, he was a Researcher with Information Control Ltd., where he was involved in space-borne observation platforms for the earth-probing satellite ERS-1. From 1989 to 1992, he was a Research Scientist with the Norwegian Research Council for Science and Humanities, where he was involved in nonlinear mapping of the ocean surface by means of synthetic aperture imaging radar. From 2000 to 2001, he did a research sabbatical at the University of California at San Francisco, San Francisco, CA, USA, where he investigated the use of multiband microwave radiometry for temperature measurement in the human body. Since 2001, he has been a Professor of electrical engineering with the Department of Physics and Technology, University of Tromsø-The Arctic University of Norway, Tromsø. His current research interests include thermal medicine, development of active and passive microwave systems, applicators for diagnostic and therapeutic applications in the human body, development of miniature unmanned aerial vehicle-mounted ultra-wideband radars for various remote sensing applications including snowpack stratigraphy for hardness investigation and weak layer detection.

## ORCID

Rolf Ole R. Jenssen  <http://orcid.org/0000-0002-8271-5979>

## References

- [1] Dierking W. Mapping of different sea ice regimes using images from Sentinel-1 and ALOS synthetic aperture radar. *IEEE Trans Geosci Remote Sens.* 2010;48(3):1045–1058.
- [2] Mahoney A, Eicken H, Graves A. Landfast sea ice extent and variability in the Alaskan Arctic derived from SAR imagery. In: 2004 IEEE International Geoscience and Remote Sensing Symposium, 2004. IGARSS'04. Proceedings. Vol. 3. IEEE; 2004. p. 2146–2149.
- [3] Farrell SL, Kurtz N, Connor LN, et al. A first assessment of IceBridge snow and ice thickness data over Arctic sea ice. *IEEE Trans Geosci Remote Sens.* 2012;50(6):2098–2111.
- [4] Tiuri M, Sihvola A, Nyfors E, et al. The complex dielectric constant of snow at microwave frequencies. *IEEE J Oceanic Eng.* 1984;9(5):377–382.
- [5] Jenssen ROR, Eckerstorfer M, Jacobsen S. Drone-mounted ultrawideband radar for retrieval of snowpack properties. *IEEE Trans Instrum Meas.* 2020;69(1):221–230.
- [6] Marshall HP, Schneebeli M, Koh G. Snow stratigraphy measurements with high-frequency FMCW radar: comparison with snow micro-penetrometer. *Cold Reg Sci Technol.* 2007;47(1–2 Spec. Iss.):108–117.
- [7] Singh KK, Datt P, Sharma V, et al. Snow depth and snow layer interface estimation using ground penetrating radar. *Curr Sci.* 2011;100(10):1532–1539.
- [8] Yankielun N, Rosenthal W, Davis RE. Alpine snow depth measurements from aerial FMCW radar. *Cold Reg Sci Technol.* 2004;40(1–2):123–134.
- [9] Kim Y, Reck TJ, Alonso-Delpino M, et al. A Ku-band CMOS FMCW radar transceiver for snowpack remote sensing. *IEEE Trans Microw Theory Tech.* 2018;66(5):2480–2494.
- [10] Øyan MJ, Hamran SE, Hanssen L, et al. Ultrawideband gated step frequency ground-penetrating radar. *IEEE Trans Geosci Remote Sens.* 2012;50(1):212–220.
- [11] Yan JB, Gomez-Garcia Alvestegui D, McDaniel JW, et al. Ultrawideband FMCW radar for airborne measurements of snow over sea ice and land. *IEEE Trans Geosci Remote Sens.* 2017;55(2):834–843.
- [12] Kwok R, Panzer B, Leuschen C, et al. Airborne surveys of snow depth over Arctic sea ice. *J Geophys Res Oceans.* 2011;116(11):1–16.
- [13] Rodriguez-Morales F, Gogineni S, Leuschen CJ, et al. Advanced multifrequency radar instrumentation for polar research. *IEEE Trans Geosci Remote Sens.* 2014;52(5):2824–2842.

- [14] Tan A, Eccleston K, Platt I. The design of a UAV mounted snow depth radar results of measurements on Antarctic sea ice. 2017 IEEE Conference on Antenna Measurements & Applications (Cama), Tsukuba, Japan; 2017. p. 316–319.
- [15] Li CJ, Ling H. High-resolution, downward-looking radar imaging using a small consumer drone. In: 2016 IEEE International Symposium on Antennas and Propagation (APSURSI), Fajardo, Puerto Rico; Vol. 2; 2016. p. 2037–2038.
- [16] Li CJ, Ling H. Synthetic aperture radar imaging using a small consumer drone. IEEE International Symposium on Antennas and Propagation; Vancouver, Canada; Vol. 10(d); 2015. p. 4–5.
- [17] Tarchi D, Guglieri G, Vespe M. Mini-radar system for flying platforms. In: 4th IEEE International Workshop on Metrology for AeroSpace, MetroAeroSpace 2017 – Proceedings, Padua, Italy; 2017. p. 40–44.
- [18] Lort M, Aguasca A, López-Martínez C, et al. Initial evaluation of SAR capabilities in UAV multi-copter platforms. IEEE J Sel Top Appl Earth Obs Remote Sen. 2018;11(1):127–140.
- [19] Šipoš D, Peter P, Gleich D. On drone ground penetrating radar for landmine detection. In: 2017 First International Conference on Landmine: Detection, Clearance and Legislations (LDCL), Beirut, Lebanon; 2017. p. 7–10.
- [20] Yarleque MA, Alvarez S, Martinez HJ. FMCW GPR radar mounted in a mini-UAV for archaeological applications: First analytical and measurement results. In: 2017 International Conference on Electromagnetics in Advanced Applications (ICEAA), Verona, Italy; Vol. 9. IEEE; 2017. p. 1646–1648.
- [21] Fitter JF, McCallum AB, Leon JP. Development of an unmanned aircraft mounted software defined ground penetrating radar. Geotechnical and Geophysical Site Characterisation, Australian Geomechanics Society; Vol. 5; 2016. p. 957–962.
- [22] Burr R, Schartel M, Mayer W. Uav-Based Polarimetric Synthetic Aperture Radar for Mine Detection. IGARSS 2019–2019. IEEE International Geoscience and Remote Sensing Symposium, Yokohama, Japan; 2019. p. 9208–9211.
- [23] Rodriguez-Vaqueiro Y, Vazquez-Cabo J, Gonzalez-Valdes B. Array of antennas for a GPR system onboard a UAV. 2019 IEEE International Symposium on Antennas and Propagation and USNC-URSI Radio Science Meeting, APSURSI 2019 – Proceedings, Atlanta, GA, USA; 2019. p. 821–822.
- [24] Drinkwater MR, Crocker GB. Modelling changes in the dielectric and scattering properties of young snow-covered sea ice at GHz frequencies. J Glaciol. 1988;34(118):274–282.
- [25] Daniels D. Ground penetrating radar. Vol. 1. London, UK: The Institution of Engineering and Technology; 2013.
- [26] Nandan V, Geldsetzer T, Yackel JJ, et al. Multifrequency microwave backscatter from a highly saline snow cover on smooth first-year sea ice: first-order theoretical modeling. IEEE Trans Geosci Remote Sens. 2017;55(4):2177–2190.
- [27] Ulaby FT, Abdelrazik M, Stiles WH. Snowcover influence on backscattering from terrain. IEEE Trans Geosci Remote Sens. 1984;GE-22(2):126–133.
- [28] Drinkwater MR. LIMEX '87 ice surface characteristics: implications for C-band SAR backscatter signatures. IEEE Trans Geosci Remote Sens. 1989;27(5):501–513.
- [29] Hufford GA. A model for the complex permittivity of ice at frequencies below 1 THz. Int J Infrared Millimeter Waves. 1991;12(7):677–682.
- [30] Matzler C, Wegmuller U. Dielectric properties of freshwater ice at microwave frequencies. J Phys D Appl Phys. 1987;20(12):1623–1630.
- [31] Hallikainen MT, Ulaby FT, Abdelrazik M. Dielectric properties of snow in the 3–37 GHz range. IEEE Trans Antennas Propag. 1986;AP-34(11):1329–1340.
- [32] Tsang L, Kong JA. Scattering of electromagnetic waves from random media with multiple scattering included. J Math Phys. 1982;23(6):1213–1222.
- [33] Huining W, Pulliainen JT, Hallikainen MT. Effective permittivity of dry snow in the 18–90 GHz range. J Electromagn Waves Appl. 1999;13(10):1393–1394.
- [34] Mätzler C. Relation between grain size and correlation length of snow. American Geophysical Union Fall Meeting, San Francisco, California; Vol. 48; 2002. p. 1–4.
- [35] Onstott RG, Shuchman RA. SAR measurements of sea ice. SAR Marine User's Manual; Vol. 3; 2004. p. 81–115.

- [36] Richards MA. Fundamentals of radar signal processing. New York: McGraw-Hill Professional; 2015.
- [37] Jenssen ROR. Snow stratigraphy measurements with UWB radar; 2016. Available from: <http://hdl.handle.net/10037/11117>.
- [38] Kim SW, Choi DY. Implementation of rectangular slit-inserted ultra-wideband tapered slot antenna. SpringerPlus. 2016 Aug;5(1):1387.
- [39] Avdushin AS, Ashikhmin AV, Negrobov VV, et al. Vivaldi antenna with printed lens in aperture. Microw Opt Technol Lett. 2014 Feb;56(2):369–371.
- [40] Albanese D, Klein A. Pseudo-random code waveform design for CW radar. IEEE Trans Aerosp Electron Syst. 1979;AES-15:67–75.
- [41] Zhang H, Li L, Wu K. Software-defined six-port radar technique for precision range measurements. IEEE Sens J. 2008;8(10):1745–1751.
- [42] Haynes MS. Surface and subsurface radar equations for radar sounders. Annals of Glaciology. 2020;16:1–8.
- [43] Greene E, Birkeland K, Elder K. Observation guidelines for avalanche programs in the United States. Bozeman (MT): American Avalanche Association; 2016.



# /10

## Paper III

### **Measurement of Snow Water Equivalent Using Drone-Mounted Ultra Wide-Band Radar**

Rolf Ole Rydeng Jensen & Svein Ketil Jacobsen

In review.





# Measurement of Snow Water Equivalent Using Drone-Mounted Ultra Wide-Band Radar

Rolf Ole R. Jenssen, Svein K. Jacobsen, *Senior Member, IEEE*

**Abstract**—The use of unmanned aerial vehicle (UAV) mounted radar for obtaining snowpack parameters has seen considerable advances over recent years. However, a robust method of snow density estimation still needs work. In this paper, we present an improved scheme for measuring snow water equivalent (SWE) from a moving UAV, which is based on non-invasive snow density measurements from the same platform. Initial results show high repeatability for depth measurements up to 5.5 m, and good agreement with Monte Carlo simulations for statistical spread of snow density estimates. The paper also outlines needed system improvements for the system to increase accuracy and less spatial variability of a snow density estimator based on an F-K migration technique.

**Index Terms**—UAV, UWB radar, Snow Water Equivalent, Snow density

## I. INTRODUCTION

THERE is a vast variety of applications for drone-mounted radar including archaeological investigations, detection of buried mines [1], [2], soil moisture mapping [3], snow, ice and glacier measurements [4], [5] and mapping of civil infrastructure [6], [7]. With regards to snow, one application is snow water equivalent (SWE) measurements, of great interest for the hydropower industry and other fields in need of meteorological data.

This paper presents a refined technological approach to SWE measurements by using ultra wide-band (UWB) radar mounted on an autonomous flying unmanned aerial vehicle (UAV). The method involves estimating snow depth and density by using well-established F-K migration theory and the Dix equation for layered media in addition to altitude correction of the flying platform. The goal is to estimate the propagation velocity in the snow using air-launched UWB signals with considerable separation ( $\sim 5$ -10 meters) between the radar platform and medium of interest (snowpack).

Today, ground-based SWE surveys (manual or with ground penetrating radar (GPR)) are usually conducted by means of snowmobile, where avalanche safety and accessibility might reduce the survey area [8]–[10].

### A. Previous Work

The ground below the snowpack in mountainous and marshland areas often contains sparse scattering objects, potentially

R. O. R. Jenssen and S. K. Jacobsen are with the Department of Physics and Technology, UiT The Arctic University of Norway, 9019 Tromsø, Norway, also with NORCE Norwegian Research Centre, 9019 Tromsø, Norway, and also with the Centre for Integrated Remote Sensing and Forecasting for Arctic Operations (CIRFA), 9019 Tromsø, Norway. Troms, Norway e-mail: rolf-ole.r.jenssen@uit.no.

Manuscript received ....; revised ...

producing diffraction hyperbolas in a radar B-scan. These objects are usually rocks with a relative permittivity ( $\sim 4$ -7) different from snow. Migration methods applied on radar imagery, at the correct propagation velocity of the intermediate medium, cause the hyperbolas to collapse at their focal point. Previous studies using commercial GPR, mounted on a snowmobile, show that SWE can be estimated using F-K migration and manual velocity picking [8]. A similar method also demonstrates auto-focusing using the varimax norm to automatically pick the velocity [11], and similar results can be produced from offset antenna arrays [12]. Furthermore, Kirchhoff's time migration with a two-layered variable-depth velocity model was used to focus radar image GPR-data from a helicopter platform [5].

Other work show SWE estimation using manually measured snow depth, snow age, and snow class defined by the location [13]. Manual depth measurements at calibration locations can also be used to estimate SWE with radars [14].

Several studies take the concept a step forward and outline methods for automatic detection and segmentation of diffraction hyperbolas. This research includes novel image threshold methods and clustering [15], parabolic fitting [16], apex detection by fitting an analytical hyperbola function to the profile edges detected with a Canny filter [17], template matching algorithms [18], and a neural network approach [19].

## II. THEORY

This section covers the main method used for SWE estimation and the theory behind the different steps. We assume that the radar image is already pre-processed with both matched filtering and frequency-domain noise filtering. These basic pre-processing steps for the UWB radar data are described in more detail in [20] and [21].

### A. Altitude correction

As the UAV performs an airborne survey of an area, the aircraft's altitude will inevitably vary somewhat, at least on a medium to large spatial scale. The altitude variations depend on what sensors the UAV computer has available to feed into the autopilot. In our setup, we have a laser rangefinder [22] that measures relative altitude on a centimeter scale. Nevertheless, small deviations from the nominal readout altitude will distort the radar image. Hence, the radar data algorithms need some correction to "level out" these variations.

The method used in this work is to circularly shift the radar data in the fast-time direction according to the relative variations in height. The rectification is performed by combining the laser range data and the first surface pulse reflection

in the radar return. The combination of altitude information in these two signals reduces spurious deviations significantly and minimizes the influence of signal drop-out in the laser rangefinder.

Prior to migration, the sectioned data segment is expanded in fast-time according to the distance measured from the UAV to the snow surface. This method is explained in more detail in [21].

### B. Methods to estimate propagation velocity in the medium

There are several different methods to estimate the propagation velocity of a radar signal return from an object [23]. Ways of extracting the propagation velocity in snow exist, such as common mid-point (CMP) gathers [24]. Alternatively, by combining two way travel time (TWT) with meteorological models obtained from empirical studies, SWE can be estimated from quasi-analytical expressions [25]. This latter model generalizes the snowpack layer model for which the density depends on depth. The assumption might be acceptable for applications that only need coarse density estimations. However, the scheme needs modifications for each new climatic zone (maritime or continental climate) to be valid [25].

Nonetheless, this paper will focus on estimating the propagation velocity by analyzing diffraction hyperbolas in B-scan radar images. If diffraction hyperbolas are present in the radar image, there are generally two different procedures to extract the bulk propagation velocity information:

- Curve fitting attempting to draw a hyperbolic function in the image by optimizing fit with underlying data [15].
- Auto-focusing techniques using a migration algorithm and generate performance metrics to find the optimum value of the velocity [26].

As previously stated, hyperbolas contain information about the mean propagation velocity in the medium. Hence, if we know the parameters which mathematically describe the hyperbola, we can estimate the propagation velocity [27] by the simple relation between the hyperbola asymptotic constants  $a$  and  $b$ . Thus, the velocity  $v_{rms}$  can be calculated from [28]:

$$v_{rms} = 2\frac{b}{a}, \quad (1)$$

where  $a$  and  $b$  need to be in their correct units, namely seconds and meters, respectively.

Auto-focusing is performed by testing different propagation velocities in a migration process where we assess how well the image is focused in order to determine the mean propagation velocity (see example in Figure 4).

### C. Auto-focusing Metrics

Auto-focusing techniques are widely used in for example synthetic aperture radar (SAR) applications for phase error correction [29]–[31], and for GPR, usually to estimate the dielectric constant [26], [32]–[34]. Auto-focusing generally works by testing different propagation velocities  $v_t$  with a migration algorithm outputting a migrated image  $s(x, y)_{v_t}$  and choosing the best fitting velocity based on some performance metric.

Since the apex of the hyperbolas should have a maximum at the correct propagation velocity, we can look at the average image intensity AI to evaluate the focusing [26]. For a migrated radar image  $s(x, y)_{v_t}$  at test velocity  $v_t$ , this parameter can be stated as:

$$AI(v_t) = \frac{\sum_{i=1}^m \sum_{j=1}^n |s(x_i, y_j)_{v_t}|^k}{\left[ \sum_{i=1}^m \sum_{j=1}^n |s(x_i, y_j)_{v_t}| \right]^k}, \quad (2)$$

where  $k \in [2, 4]$ .

However, this metric is known to have poor performance for increasing signal to noise ratio (SNR) [35]. Thus, higher-order techniques that involve the variance of the migrated image [35] can be expressed by:

$$AH(v_t) = \frac{\sum_{i=1}^m \sum_{j=1}^n [|s(x_i, y_j)_{v_t}| - \hat{\mu}]^k}{(mn - 1)\hat{\sigma}^k} \quad (3)$$

where  $k \geq 1$ , and  $\hat{\mu}$  and  $\hat{\sigma}$  are the mean and variance of the migrated data, respectively.

As in [35], a  $k$  value of 10 was found to be optimal. AH will have a maximum at the best fitting propagation velocity representing the mean propagation velocity  $v_{rms}$  along the antenna-to-target trajectory.

### D. Dix equation

We emphasize that the best fit velocity  $v_{rms}$  represents the average velocity from the antennas to the hyperbola. Hence, to remove the influence of the air section to calculate the average propagation velocity  $v_s$  in the snow itself, Dix's equation for layered media can be used [36]:

$$v_s = \sqrt{\frac{v_{rms}^2 t_{tot} - v_{air}^2 t_{air}}{t_{tot} - t_{air}}}, \quad (4)$$

where  $t_{tot}$  is the total TWT in the medium,  $t_{air}$  is the TWT of the air layer and  $v_{air}$  is the approximate propagation velocity in the atmosphere (i.e. approximately 0.2997 m/ns).

### E. Estimation of Snow Parameters

Snow depth is usually measured by evaluating the TWT from the snow surface to the ground and calculating the distance traveled based on an estimate of the propagation velocity.

For lossless, homogeneous, isotropic materials, the relative propagation velocity in the snow  $v_s$  is related to the relative dielectric constant  $\epsilon_r$  by [27]:

$$\epsilon_r = \left(\frac{c}{v_s}\right)^2, \quad (5)$$

where  $c$  is the propagation velocity in free space. The depth  $d_s$  is then simply written as:

$$d_s = v_s \frac{t}{2}. \quad (6)$$

Equation (5) states that the relative dielectric constant is nonlinearly related to the propagation velocity. From this relation,

there are several different models for estimating density of the snow.

The relation between snow permittivity and density has been modeled both theoretically [37] and empirically [38]. Considering dry snow, a linear relationship is an acceptable approximation for snow densities below  $0.5 \text{ g cm}^{-3}$ , where the relation between the real part of the relative dielectric constant  $\epsilon_r'$  and snow density  $\rho_s$  can be modeled as [38]:

$$\rho_s = \frac{\epsilon_r' - 1}{2}. \quad (7)$$

SWE is the depth of water resulting from the mass of melted snow and typically expressed in millimeters of equivalent water [39]. The SWE is the product of the snow depth and the vertically-integrated snow density, and can be expressed as:

$$\text{SWE} = d_s \rho_s. \quad (8)$$

Furthermore, SWE is often used to estimate the total precipitation in a given location and the resulting water volume available for the melt season.

### III. MONTE CARLO SIMULATION OF FK-MIGRATION METHOD

The proposed method discussed above involves several steps using error-prone parameters. The parameters include altitude and position data from the UAV dataflash-log applied to calculate the distance and the altitude vectors. These vectors position the data in 2D-space and are essential inputs to the migration algorithm.

In this section we evaluate the uncertainty of the method by creating synthetic data sets of a single hyperbola in an otherwise homogeneous medium. The synthetic data is F-K migrated and combined with Equation (3) resulting in an estimate for  $v_{rms}$ . Further, using Equations (4) (giving  $v_s$ ), (5), and (7), we calculate the bulk dielectric constant  $\epsilon_r$  and density  $\rho_s$  of the snowpack.

The altitude and distance vectors are given random errors set to adequate values for our imaging system to make the simulations relevant for real data results. Specifically, the synthetic data parameters are given values similar to the field trials data in Section VI, with a fixed snow-depth of 2 m and an initial altitude (above the snow surface) of 7 m over a horizontal distance of 15 m. The mean propagation velocity is set to 0.29 m/ns resulting in a snow velocity of 0.258 m/ns after Dix equation analysis.

#### A. Laser altimeter error sources

The SF-11 rangefinder data-sheet [22] reports an accuracy of  $\pm 10$  cm. Additionally, the laser is not always pointing in nadir due to the attitude of the UAV, which is corrected through the attitude data (roll, pitch, yaw). However, given that the UAV often flies over uneven terrain, additional errors are expected.

The rangefinder error is assumed normally distributed in the Monte Carlo analysis, with a standard deviation of 15 cm deemed reasonable. The altitude error contributes twice to the erroneous estimations since it is part of two parameters in the

method. Firstly, prior to the focusing when the length of the fast-time vector is adjusted according to the altitude above the surface. Secondly, in the time parameter when Dix's equation is applied.

#### B. Distance error sources

The distance vector is calculated using the Haversine formula [40] on the filtered position data produced by the UAV autopilot. The position estimate is the output of the autopilot extended Kalman filter (EKF). The EKF estimates vehicle position, velocity, and angular orientation based on rate gyroscopes, accelerometer, compass (magnetometer), global positioning system (GPS), airspeed, and barometric pressure measurements. Concerning the method proposed in this paper, the error can be defined as the deviation from linear movement (constant horizontal velocity), as the absolute position is not relevant for the focusing procedure. In real data, the deviation from a perfectly linear equidistant distance vector (i.e., constant horizontal velocity) was approximately 0.037 m looking at real data sets from autonomous flights. Therefore, we choose a standard deviation slightly larger than this (0.045 m) as a conservative assumption for the error analysis.

The distance error is applied to the data by interpolating the synthetic data set along the distance axis according to the linear movement deviation producing non-equidistant sampling. As expected, the interpolation procedure causes some skewness in the hyperbola that influences the statistical results (see the next subsection).

#### C. Monte Carlo Simulation Results

An essential prerequisite of the autofocusing method under study is that it is unbiased to produce a close to correct estimate of the sought parameter (snow density or SWE) mean value.

The Anderson-Darling, Jarque-Bera, and Chi-square tests [41]–[43] all indicate that the results from the Monte Carlo simulations are normally distributed both in the bi-variate case and with the errors combined as in Figure 1. As seen in Figure 1, the velocity estimates are unbiased, with a standard deviation of 0.0031 m/ns.

Introducing Dix's equation in Figure 1b causes further uncertainties in the estimate since we use the erroneous altitude once more. However, the method is still unbiased with an increased standard deviation of 0.0147 m/ns. Since the estimation of  $\epsilon_r$  in Figure 1c involves squaring of the velocity estimates, the distribution (if assumed normal) is transformed to a Chi-Square distribution of order 1. However, if the standard deviation is significantly smaller than the mean, the Chi-square distribution can be approximated as normally distributed. Finally, the approximate linear relationship in Equation (7) is used to obtain the distribution in Figure 1d.

We now compare the Monte Carlo derived results with the theoretical approximate first two moments derived in Appendix A. Using  $\mu=0.234$  m/nsecs and  $\sigma=0.0147$  m/nsecs in Equations (18) and (19), we get  $\mu_c=1.639$  (1.6% deviation) and  $\sigma_c=0.205$  (5% deviation). Furthermore, using Equations (21) and (22), we obtain  $\mu_\rho=0.319$  g/cm<sup>3</sup> (2.6% deviation) and

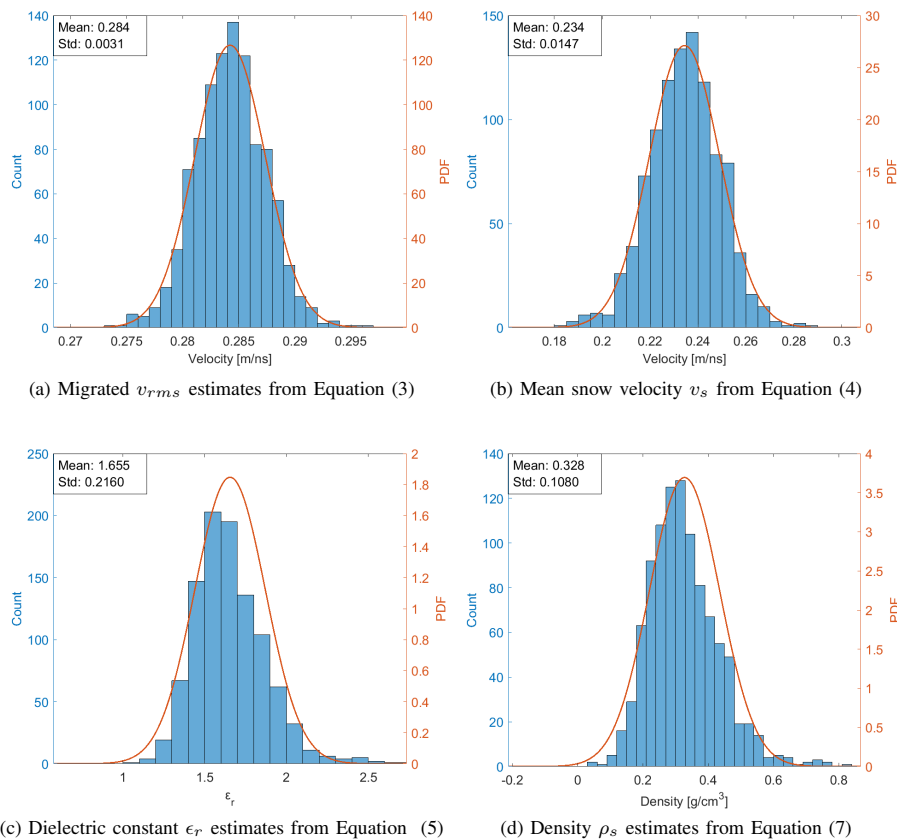


Fig. 1. Combined altitude and distance errors influence on estimators derived by Monte Carlo simulations.

$\sigma_\rho=0.103 \text{ g/cm}^3$  (4.6% deviation) all results compared to values in Figure 1c.

The Monte Carlo simulations emphasize the need for accurate positioning for the presented method as the relative spread of the density parameter is relatively large compared to the mean value ( $\sigma_\rho/\mu_\rho=0.33$ ). Nonetheless, using the average of several estimates to reduce the estimator spread could be a useful approach as the snow density spatial variability is expected to be much smaller than local variations in snow depth [44].

#### IV. RADAR SYSTEM

The ultra-wideband snow sounder (UWiBaSS) is a custom developed radar system for drone-mounted snow measurements. Papers [20], [21], [45] detail recent advances of the radar system. New developments include retrofitting the radio frequency (RF) operation band as well as digital modules with 3D printed casings coated in conductive paint to reduce weight while still offering electromagnetic interference (EMI) protection. Additionally, 500 MHz high-pass filters are added to the receiving (RX) channels to reduce low-frequency antenna cross-talk. Table I summarizes main features of the UWB-system whereas Figure 2 shows the UAV "Cryocopter FOX" during flight.

TABLE I  
UWiBaSS KEY CHARACTERISTICS.

Attribute	Value
Signal generation	UWB Pseudo noise
System bandwidth	3.8 GHz (0.7 to 4.5 GHz)
Range resolution	$\approx 5 \text{ cm}$
m-sequence clock frequency	12.8 GHz
Measurement rate	52 Hz (max 1 kHz)
MLBS order	9 (511 range bins)
Nominal output power	17.3 dBm
Unambiguous range in air	5.98 m
Average power consumption	8.1 to 9 W
Total Weight	$\approx 3 \text{ kg}$

#### V. PROCESSING FLOW

The basic pre-processing steps for the sampled radar data involve match filtering to correlate the received signal with the transmitted signal, high-pass filtering to remove low-frequency cross-talk between receiving (RX) and transmitting (TX) antennas, reference subtraction, and altitude correction involving rectification of the snow surface return. A detailed description can be found in [21].

The laser altimeter measures the distance to the snow surface. By locating the first interface reflection, the radar is capable of similar distance measurements. We have found that the best practice is to use a combination of both sensors in



Fig. 2. UWiBaSS mounted under the UAV Cryocopter FOX during flight.

case of laser signal drop out, which sometimes occurs, possibly when the laser altimeter beam strikes large snow crystals at an angle.

A distance-vector representing traveled distance over the snow surface is calculated using the position data collected from the UAV autopilot. Using the Haversine formula, we calculate the distance between each coordinate point to generate the distance vector. Due to the non-equidistant sampling of this vector, the radar data goes through a non-linear interpolation in the slow-time direction. This procedure interpolates the radar data into a domain with equidistant position samples in space, allowing us to fix the sampling interval  $dx$  instead of calculating a mean value for each segment.

Hyperbolas in the radar image are segmented manually using a simple "draw rectangle" function, creating a slow-time section of the image to focus within. Furthermore, fast-time data outside the rectangular window is set to zero. Although not implemented here, this step can be automated [15].

The method averages altimeter data within each short section. Further, we add zeros to the top of the radar image corresponding to the actual scanning platform altitude above the snow surface, effectively recreating the "real" radar scenario.

Figure 3 shows an example image of the processed radar data before the auto-focusing procedure.

#### A. Auto focusing

The autofocusing procedure involves performing F-K migration for a set of test velocities, where autofocusing metrics are calculated for each test velocity. In order to reduce the numerical calculation time, the search for the optimal velocity can be done in several different ways, such as first performing a low-resolution scan over a broad spread of velocities before performing a high-resolution scan over a much more narrow interval. For the present tests, we use a brute force linear vector in two steps. First a coarse search with step value of 0.01 m/ns to scan through and interval from 0.1 to 0.4 m/ns. Thereafter, a fine search is used with step value of 0.0005 m/ns to scan through an interval from 0.25 to 0.3 m/ns. Figure 5 shows the combined autofocusing result of the coarse and fine search.

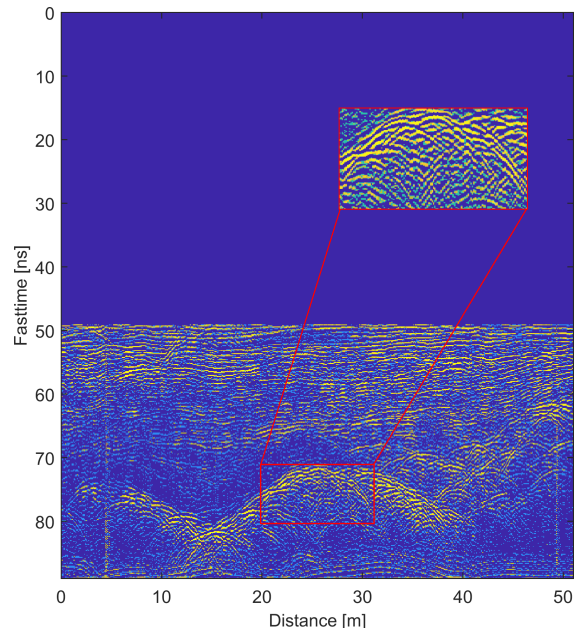


Fig. 3. Example radar image of hyperbola segmenting and altitude correction.

F-K migration is performed with the CREWES MatLab toolbox written by G. F. Margrave for the CREWES project (University of Calgary) [46], [47]. The F-K domain interpolation routine was modified with a convolution, omitting a for-loop in order to reduce the computational time. This modification improved the speed of the function by approximately 200 %.

After migration over all test velocities, we select the autofocusing metric's (see Equation (3)) maximal value, corresponding to a "best fit" propagation velocity. This velocity represents the average velocity from the radar antennas to the ground, and therefore, we need to remove the influence of the air section with Dix's equation. This estimation is performed for each manually selected section. The section length is typically in the range of 5-20 m containing one or more hyperbolas. Figure 4 shows an example of the auto focusing result for a segment gathered as in Figure 3.

## VI. FIELD TRIALS

Due to Covid-19, two major field campaigns were canceled in the winter of 2020. However, a 1-day campaign 10 km from UiT The Arctic University of Norway was carried out. The main goal of the campaign was to test the latest iteration of the radar system and preliminarily investigate methods to measure snow density.

A transect of approximately 200 m was flown autonomously in four passes to test the reproducibility of the method. A section of the transect showed several overlapping hyperbolas at the ground level (shown in Figure 3). These hyperbolas were assumed to be caused by reflections from rocks, as is well known from traditional GPR [27], but not necessarily given that the UWiBaSS would be able to detect hyperbolas from targets buried beneath several meters of snow while airborne.

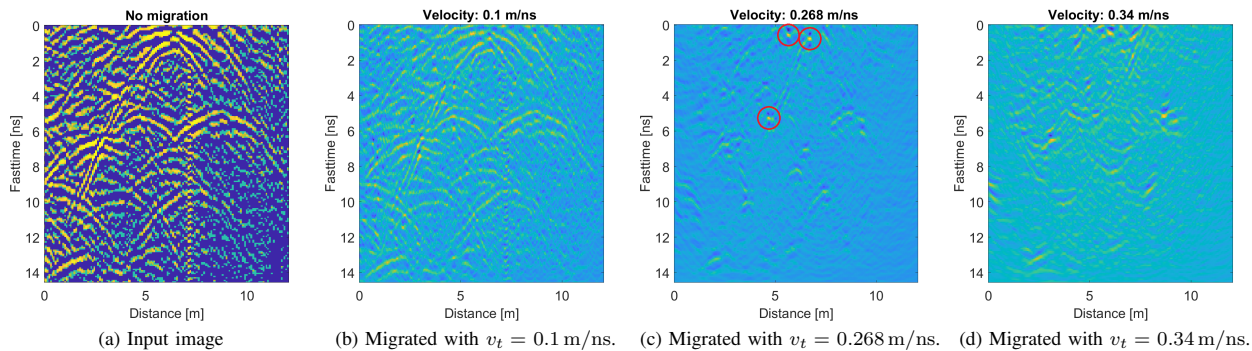


Fig. 4. Example of the auto-focusing procedure for an image segment, with input data (a), under-migrated data (b), migration result from auto focusing optimum value (c), over-migrated image (d).

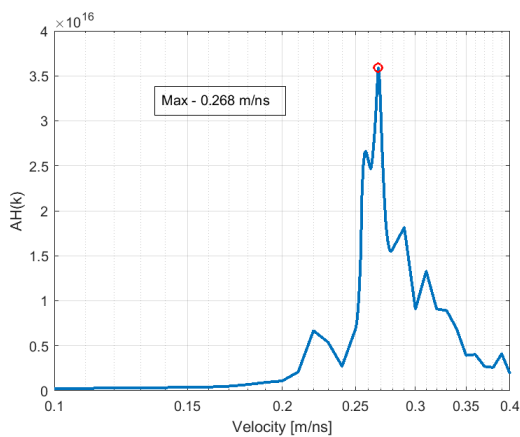


Fig. 5. Auto-focusing metric from Equation (3).

As shown in Figure 7 and 8, the snow depth in this transect varied from 1 m to almost 6 m. After the spring snowmelt, radar data images containing hyperbolas were confirmed to be from a rocky area as shown in Figure 9. Four passes over this rocky area of the transect were segmented into 40 smaller segments used to estimate the density.

For this data set, the returning signal from the snowpack was taken at the second period of the transmitted signal owing to the radar system having a 5.7 m unambiguous range, and the data collection was taken from approximately 7 m relative altitude, excluding snow depth. For more information on performing measurements outside the unambiguous range from UAV radar, see [21].

The *in situ* density for each noticeable layer was collected in a snow pit close to the transect. We found the mean density (weighted mean based on the thickness of each layer) to be  $0.327 \text{ g cm}^{-3}$ .

Figure 6 shows the distribution of density estimations from the autofocusing procedure. Figure 7 shows measured snow depth along the 200 m transect for four passes. Identification of the snow-ground interface is described in [21] where we obtain the TWT used in Equation (6). Snow depth is then calculated using TWT and the estimated propagation velocity

of the snow.

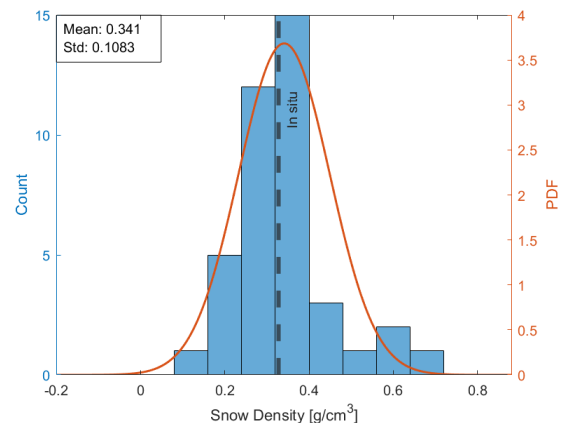


Fig. 6. Distribution of density estimates from 40 measurements. Mean *in situ* snow-profile density shown as dashed line.

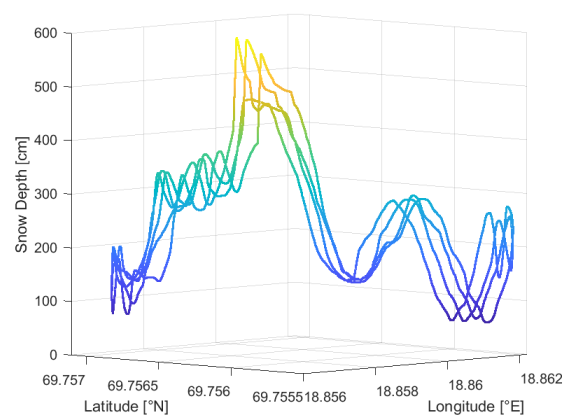


Fig. 7. Depth measurements along transect for four passes.

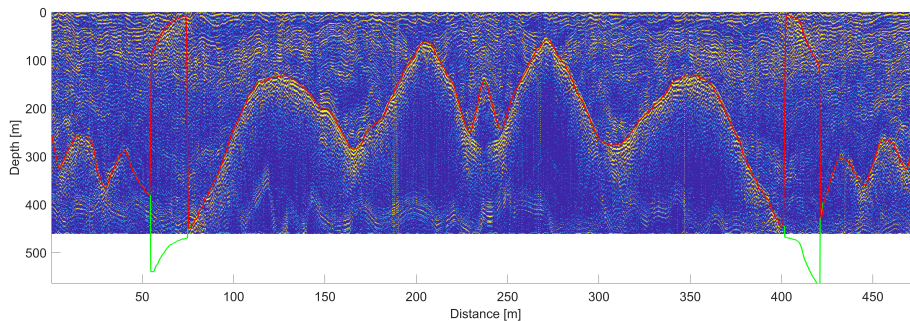


Fig. 8. B-scan radar image of one pass -back and forth- across the transect. Red line indicates snow-ground interface and green line indicates snow-ground interface detected in second ambiguity window (i.e., deeper than  $\approx 460$  cm for  $\epsilon_r = 1.68$ )

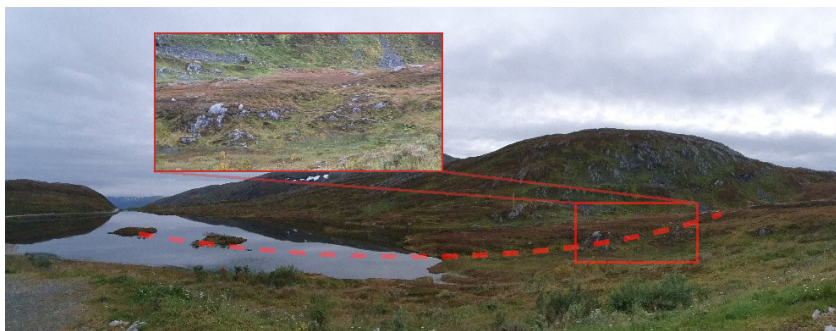


Fig. 9. Transect containing rocky parts after melt season. Dotted line indicate the transect. Cropped out section show the rocky area.

## VII. DISCUSSION

The accuracy of the method seems to depend heavily on the accuracy of the UAV GPS altimeter since the spatial sampling rate and correct position and altitude above snow are important for the F-K migration algorithm. Hence, real-time kinematic (RTK) GPS should be used for better distance calculations and data interpolation [48].

Ideally, several snow pits should have been dug along the transect. However, the project's time constraints limited the *in situ* collection to one full snowpit.

Taking the average of the altitude for each section most probably does not introduce significant errors, as the typical variation in altitude across the sections is on the order of a few cm. However, for robustness, modifying the code to create a variable altitude above the snow should be implemented in future work.

Comparing Figure 1d with Figure 6, we see that the statistical spread (standard deviation) is of the same order, which leads us to believe that the error assessments made to the scanning system prior to the Monte Carlo simulation were reasonable and that other contributing error sources are of minor importance in the campaign.

Of vital importance in determining the SWE is to which degree the snow depth measurements can be trusted. A comparison of depth measurements for several passes along the same transect gives a good indication of the repeatability of the depth measurements. This can be seen for four passes in Figure 7 and for two passes overlaid the radar B-scan in Figure 8.

Correlating the four transects results in the correlation matrix  $R$ :

$$R = \begin{pmatrix} 1.00 & 0.97 & 0.98 & 0.93 \\ 0.97 & 1.00 & 0.96 & 0.92 \\ 0.98 & 0.96 & 1.00 & 0.93 \\ 0.93 & 0.93 & 0.93 & 1.00 \end{pmatrix}. \quad (9)$$

Overall, the correlation is very high, with the lowest value of 0.92 between passes 2 and 4. The slight skewness between the depth measurements in Figure 7 appears to come from drift in the UAV positioning. The snow depth is measured beyond 5 m which is deeper than the 3 m depth probes we had available. However, *in situ* depth validation of the same radar system is presented in [21].

Notice in Figure 3 that the reconstructed radar pulse delay becomes almost 90 ns, resulting in a total distance from the antennas to the ground of approximately 10 to 14 m. With an unambiguous range of 5.9 m, this is accomplished by exploiting the lack of significant reflections in the air-section except for the cross-talk [21] and thus using the previous transmitted pulse for detection.

## VIII. CONCLUSION

In this paper, we present a non-invasive method to estimate snow density from a UAV, that could be further be used to estimate SWE. Density estimations from a limited field trial show good agreement with *in situ* snow density. However,

the sample base for both *in situ* and radar data is somewhat limited.

The standard deviation (0.1 from Figure 6) of the estimations are comparable to what is observed in previous papers [8], reporting a standard deviation of 0.07 from a snowmobile platform with a fixed antenna-to-snow air gap of approximately 50 cm.

Snow depth measurements show high repeatability but will likely also benefit from more accurate platform positioning.

Future work will include field campaigns with RTK ready UAV for improved position and altitude information, as well as high-resolution *in situ* density measurements using the SnowMicroPen (SMP) or similar devices.

Additionally, automatic image segmentation should be implemented to reduce the amount of manual labor to analyze the data sets.

Multi-thread programming should be implemented on the interpolation part of the F-K migration routine to improve speed, as this section of the code occupies approximately 95 % of the run time.

#### APPENDIX A

##### MAPPING OF SQUARED INVERSE GAUSSIAN VARIABLE

Consider a Gaussian variable  $X$  with standard deviation  $\sigma$  and mean value  $\mu$ . Then, defining

$$\chi = \frac{X - \mu}{\sigma}, \quad (10)$$

$\chi^2$  is centrally chi-squared distributed with one degree of freedom.

Knowing that  $E[\chi^2]=1$  and  $E[\chi^4]=2$  of a central chi-squared distribution, the first and second moments of  $X$  can be stated:

$$E[X^2] = \sigma^2 + \mu^2 \approx \mu^2 \quad (11)$$

$$\text{var}[X^2] = \sigma^4 + 4\sigma^2\mu^2 \approx 4\mu^2\sigma^2. \quad (12)$$

where the approximations are valid if  $\sigma \ll \mu$ ; that is a narrow probability distribution of  $X$ .

Mapping a Gaussian variable  $X$  with the following relation:  $w = RX^2$ , we get the probability density function (pdf) [49]:

$$p(w) = \frac{1}{2\sqrt{Rw}} \left[ \frac{1}{\sigma\sqrt{2\pi}} \exp\left(-\frac{(\sqrt{w/R} - \mu)^2}{2\sigma^2}\right) + \frac{1}{\sigma\sqrt{2\pi}} \exp\left(-\frac{(-\sqrt{w/R} - \mu)^2}{2\sigma^2}\right) \right]. \quad (13)$$

Notice that for situations where  $\sigma \ll \mu$ , the last term in Equation (13) can be neglected unless  $w$  and  $\mu$  are close to zero.

Then, Equation (13) can be stated:

$$p(w) \approx \frac{1}{2\sqrt{Rw}} \frac{1}{\sigma\sqrt{2\pi}} \exp\left(-\frac{(\sqrt{w/R} - \mu)^2}{2\sigma^2}\right). \quad (14)$$

Furthermore, Taylor series expanding the argument in the exponential function to second order around the central value

$w_0 = \mu^2 R$  of the distribution, and similarly approximating the denominator  $\sqrt{Rw} \approx \mu R$ , we get:

$$p(w) \approx \frac{1}{2\mu R\sigma} \frac{1}{\sqrt{2\pi}} \exp\left(-\frac{(w - \mu^2 R)^2}{8R^2\mu^2\sigma^2}\right). \quad (15)$$

We recognize Equation (15) as a Gaussian distribution with standard deviation  $\sigma' = 2\mu R\sigma$  and mean value  $\mu' = \mu^2 R$ , in accordance with the results obtained in Equations (11) and (12), if  $R = 1$ .

The permittivity  $\epsilon$  of snow is related to propagation velocity  $v$  through  $\epsilon = (c/v)^2$ , where  $c$  is the speed of light in air. In order to relate this mapping to Equation (15), define the reciprocal variable  $u = 1/w$ . Now, it can readily be shown that:

$$p(u) = \frac{1}{\sqrt{2\pi}\sigma'u^2} \exp\left(-\frac{(1/u - \mu')^2}{2\sigma'^2}\right). \quad (16)$$

Again, Taylor expanding  $u^2$  to zeroth order and Taylor expanding the argument of the exponential function to second order, both around  $u_0 = 1/\mu'$ , Equation (16) reduces to:

$$p(u) = \frac{1}{\sqrt{2\pi}(\sigma'/\mu'^2)} \exp\left(-\frac{(u - 1/\mu')^2}{2(\sigma'/\mu'^2)^2}\right). \quad (17)$$

From Equation (17), we see that  $u$  is also normally distributed with mean value  $\mu_u = 1/\mu'$  and standard deviation  $\sigma_u = \sigma'/\mu'^2$ .

Furthermore, the constant  $R$  can be identified as  $R = 1/c^2$  and  $X = v$ , leading the the final result that  $\epsilon$  is close to normally distributed with first and second moments:

$$\mu_\epsilon = \frac{c^2}{\mu^2} \quad (18)$$

$$\sigma_\epsilon = \frac{2c^2\sigma}{\mu^3}, \quad (19)$$

provided that  $\sigma \ll \mu$ .

According to [38], there exists a linear relation between the dielectric constant  $\epsilon$  and density  $\rho$  in dry snow:

$$\epsilon = 1 + 2\rho \quad (20)$$

This leads to the first and second moments of  $\rho$ :

$$\mu_\rho = \frac{1}{2}\mu_\epsilon - \frac{1}{2} \quad (21)$$

$$\sigma_\rho = \frac{1}{2}\sigma_\epsilon. \quad (22)$$

Hence, we get a constant change in mean value and spread in the probability distribution of  $1/2$  as expected from a linear transformation.

As an example, assume a statistical draw of  $v$  above from a Gaussian distribution. Figure 10 shows the histogram from 100,000 statistical realizations mapped by using  $\epsilon = (c/v)^2$  with first and second moments of snow velocity of 0.244 m/nsecs and 0.0127 m/nsecs, respectively.

Observe that the fit between the histogram and the theoretical approximate Gaussian distribution is not perfect as the assumption that  $\sigma_\epsilon \ll \mu_\epsilon$ , ( $0.16 \ll 1.51$ ) is not entirely fulfilled.



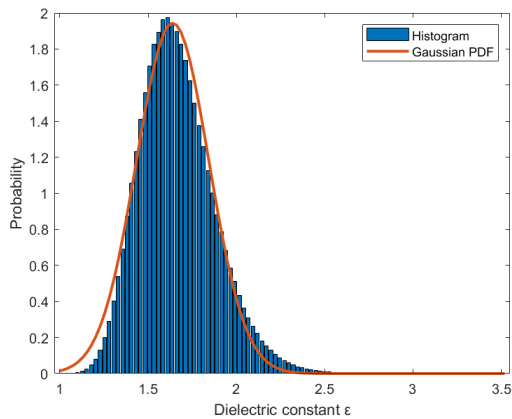


Fig. 10. Histogram of dielectric constant  $\epsilon$  from 100,000 realizations. Solid line: Gaussian approximation from Eq. (17). Mean value and standard deviation are,  $\mu_\epsilon=1.51$  and  $\sigma_\epsilon=0.16$ , respectively.

#### ACKNOWLEDGMENT

The authors would like to thank M. Eckerstorfer and A. Kjellstrup for collecting *in situ* data and operating the UAV during the field trials.

This work was supported by the Centre for Integrated Remote Sensing and Forecasting for Arctic Operations (CIRFA) partners (Grant No. 237906); and NORCE Norwegian Research Centre (Grant No. 261786); Research Council of Norway.

#### REFERENCES

- [1] M. R. P. Cerquera, J. D. Colorado Montaña, and I. Mondragón, "UAV for Landmine Detection Using SDR-Based GPR Technology," in *Robots Operating in Hazardous Environments*, 2016, no. tourism, p. 13. [Online]. Available: <https://www.intechopen.com/books/advanced-biometric-technologies/liveness-detection-in-biometrics>
- [2] D. Šipoš, P. Peter, and D. Gleich, "On drone ground penetrating radar for landmine detection," *2017 First International Conference on Landmine: Detection, Clearance and Legislations (LDCL)*, pp. 7–10, 2017.
- [3] K. Wu, G. A. Rodriguez, M. Zajc, E. Jacquemin, M. Clément, A. De Coster, and S. Lambot, "A new drone-borne GPR for soil moisture mapping," *Remote Sensing of Environment*, vol. 235, no. November, p. 111456, 2019. [Online]. Available: <https://doi.org/10.1016/j.rse.2019.111456>
- [4] A. E.-C. Tan, J. McCulloch, W. Rack, I. Platt, and I. Woodhead, "Radar Measurements of Snow Depth Over Sea Ice on an Unmanned Aerial Vehicle," *IEEE Transactions on Geoscience and Remote Sensing*, pp. 1–8, 2020.
- [5] A. Rutishauser, H. Maurer, and A. Bauder, "Helicopter-borne ground-penetrating radar investigations on temperate alpine glaciers: A comparison of different systems and their abilities for bedrock mapping," *Geophysics*, vol. 81, no. 1, pp. WA119–WA129, 2016.
- [6] W. W. Greenwood, J. P. Lynch, and D. Zekkos, "Applications of UAVs in Civil Infrastructure," *Journal of Infrastructure Systems*, vol. 25, no. 2, p. 04019002, 2019.
- [7] C. J. Li and H. Ling, "High-resolution, downward-looking radar imaging using a small consumer drone," in *2016 IEEE International Symposium on Antennas and Propagation (APSURSI)*, vol. 2, 2016, pp. 2037–2038.
- [8] W. S. Holbrook, S. N. Miller, and M. A. Provart, "Estimating snow water equivalent over long mountain transects using snowmobile-mounted ground-penetrating radar," *Geophysics*, vol. 81, no. 1, pp. WA183–WA193, 2016.
- [9] O. B. Knut Sand, "Application of Georadar for Snow Cover Surveying," *Hydrology Research*, vol. 29, pp. 361–370, 1998.
- [10] C. Derksen, P. Toose, A. Rees, L. Wang, M. English, A. Walker, and M. Sturm, "Development of a tundra-specific snow water equivalent retrieval algorithm for satellite passive microwave data," *Remote Sensing of Environment*, vol. 114, no. 8, pp. 1699–1709, 2010. [Online]. Available: <http://dx.doi.org/10.1016/j.rse.2010.02.019>
- [11] J. S. Clair and W. Steven Holbrook, "Measuring snow water equivalent from common-offset GPR records through migration velocity analysis," *Cryosphere*, vol. 11, no. 6, pp. 2997–3009, 2017.
- [12] D. Gustafsson, N. Sundström, and A. Lundberg, "Estimation of Snow Water Equivalent of Dry Snowpacks Using a Multi-Offset Ground Penetrating Radar System," in *69th EASTERN SNOW CONFERENCE, Frost Valley YMCA, Claryville, New York*, 2012, pp. 197–206.
- [13] O. Bruland, Å. Færevåg, I. Steinsland, G. E. Liston, and K. Sand, "Weather SDM: Estimating Snow density with high precision using Snow depth and local climate," *Hydrology Research*, vol. 46, no. 4, pp. 494–506, 2015.
- [14] R. W. Webb, "Using ground penetrating radar to assess the variability of snow water equivalent and melt in a mixed canopy forest, Northern Colorado," *Frontiers of Earth Science*, vol. 11, no. 3, pp. 482–495, 2017.
- [15] Q. Dou, L. Wei, D. R. Magee, and A. G. Cohn, "Real-Time Hyperbola Recognition and Fitting in GPR Data," *IEEE Transactions on Geoscience and Remote Sensing*, vol. 55, no. 1, pp. 51–62, 2017.
- [16] X. Zhou, H. Chen, and J. Li, "An Automatic GPR B-Scan Image Interpreting Model," *IEEE Transactions on Geoscience and Remote Sensing*, vol. 56, no. 6, pp. 3398–3412, 2018.
- [17] L. Mertens, R. Persico, L. Matera, and S. Lambot, "Automated Detection of Reflection Hyperbolas in Complex GPR Images with No A Priori Knowledge on the Medium," *IEEE Transactions on Geoscience and Remote Sensing*, vol. 54, no. 1, pp. 580–596, 2016.
- [18] F. Sagnard and J. P. Tarel, "Template-matching based detection of hyperbolas in ground-penetrating radargrams for buried utilities," *Journal of Geophysics and Engineering*, vol. 13, no. 4, pp. 491–504, 2016. [Online]. Available: <http://dx.doi.org/10.1088/1742-2132/13/4/491>
- [19] S. Birkenfeld, "Automatic detection of reflexion hyperbolas in GPR data with neural networks," *2010 World Automation Congress, WAC 2010*, 2010.
- [20] R. O. R. Jenssen, M. Eckerstorfer, and S. Jacobsen, "Drone-Mounted Ultrawideband Radar for Retrieval of Snowpack Properties," *IEEE Transactions on Instrumentation and Measurement*, vol. 69, no. 1, pp. 221–230, 2020.
- [21] R. O. R. Jenssen and S. Jacobsen, "Drone-mounted UWB snow radar: technical improvements and field results," *Journal of Electromagnetic Waves and Applications*, vol. 34, no. 14, pp. 1930–1954, 2020.
- [22] Lightware, "SF11 Laser altimeter Datasheet," pp. 1–20, 2018.
- [23] S. SERKAN and V. BORECKY, "Estimation Methods for Obtaining GPR Signal Velocity," in *ACSEE 2015*, no. October, 2015, pp. 43–47.
- [24] H. Liu, K. Takahashi, and M. Sato, "Measurement of dielectric permittivity and thickness of snow and ice on a brackish lagoon using GPR," *IEEE Journal of Selected Topics in Applied Earth Observations and Remote Sensing*, vol. 7, no. 3, pp. 820–827, 2014.
- [25] A. Lundberg, C. Richardson-Näslund, and C. Andersson, "Snow density variations: Consequences for ground-penetrating radar," *Hydrological Processes*, vol. 20, no. 7, pp. 1483–1495, 2006.
- [26] X. Wei and Y. Zhang, "Autofocusing techniques for GPR data from RC bridge decks," *IEEE Journal of Selected Topics in Applied Earth Observations and Remote Sensing*, vol. 7, no. 12, pp. 4860–4868, 2014.
- [27] D. Daniels, *Ground Penetrating Radar (2nd Edition)*. Institution of Engineering and Technology, 2013.
- [28] A. M. Alani and F. Tosti, "GPR applications in structural detailing of a major tunnel using different frequency antenna systems," *Construction and Building Materials*, vol. 158, pp. 1111–1122, 2018. [Online]. Available: <https://doi.org/10.1016/j.conbuildmat.2017.09.100>
- [29] Y. Zhao, S. Gao, Z. Zhang, J. He, and W. Yu, "An extended target autofocus algorithm for high resolution SAR imaging," *IET Conference Publications*, vol. 2017, no. CP728, pp. 1–5, 2017.
- [30] D. E. Wahl, P. H. Eichel, D. C. Ghiglia, and C. V. Jakowatz, "Phase Gradient Autofocus—A Robust Tool for High Resolution SAR Phase Correction," *IEEE Transactions on Aerospace and Electronic Systems*, vol. 30, no. 3, pp. 827–835, 1994.
- [31] R. L. Morrison, M. N. Do, and D. C. Munson, "SAR image autofocus by sharpness optimization: A theoretical study," *IEEE Transactions on Image Processing*, vol. 16, no. 9, pp. 2309–2321, 2007.
- [32] X. Wei and Y. Zhang, "Interference Removal for Autofocusing of GPR Data from RC Bridge Decks," *IEEE Journal of Selected Topics in Applied Earth Observations and Remote Sensing*, vol. 8, no. 3, pp. 1145–1151, 2015.

- [33] L. Qu, Y. Ge, and T. Yang, "Sparsity-based SFCW-GPR autofocusing imaging method under EM wave velocity uncertainty," *Electronics Letters*, vol. 53, no. 8, pp. 568–570, 2017.
- [34] H. Jung and K. Kim, "Iteration Strategy for Autofocusing Metric Evaluation in GPR Imaging," in *ISAP 2018 - 2018 International Symposium on Antennas and Propagation*, 2019, pp. 24–25.
- [35] X. Wei, "Gpr Data Processing for Reinforced Concrete Bridge Decks," Ph.D. dissertation, Georgia Institute of Technology, 2014.
- [36] C. H. Dix, "Seismic velocities from surface measurements," *Geophysics*, vol. 20, no. 1, pp. 68–86, 1955.
- [37] L. Tsang and J. A. Kong, "Scattering of electromagnetic waves from random media with multiple scattering included," *Journal of Mathematical Physics*, vol. 23, no. 6, pp. 1213–1222, 1982.
- [38] M. Tiuri, A. Sihvola, E. Nyfors, and M. Hallikaiken, "The complex dielectric constant of snow at microwave frequencies," *IEEE Journal of Oceanic Engineering*, vol. 9, no. 5, pp. 377–382, 1984.
- [39] C. Fierz, R. Armstrong, Y. Durand, P. Etchevers, E. Greene, M. McClung, D. K. Nishimura, P. Satyawali, and S. Sokratov, "The International Classification for Seasonal Snow on the Ground Prepared by the ICSI-UCCS-IACS Working Group on Snow Classification," *IHP-VII Technical Documents in Hydrology N° 83, IACS Contribution N° 1*, p. 90p, 2009. [Online]. Available: <http://www.unesco.org/water/ihp>
- [40] V. Hegde, T. S. Aswathi, and R. Sidharth, "Student residential distance calculation using Haversine formulation and visualization through GoogleMap for admission analysis," *2016 IEEE International Conference on Computational Intelligence and Computing Research, ICCIC 2016*, 2017.
- [41] T. W. Anderson and D. A. Darling, "A Test of Goodness of Fit," *Journal of the American Statistical Association*, vol. 49, no. 268, pp. 765–769, 1954.
- [42] C. M. Jarque and A. K. Bera, "A Test for Normality of Observations and Regression Residuals," *International Statistical Review / Revue Internationale de Statistique*, vol. 55, no. 2, p. 163, 1987.
- [43] Matlab, "Statistics and Machine Learning Toolbox," 2020. [Online]. Available: <https://se.mathworks.com/help/stats/index.html>
- [44] J. I. López-Moreno, S. R. Fassnacht, J. T. Heath, K. N. Musselman, J. Revuelto, J. Latron, E. Morán-Tejeda, and T. Jonas, "Small scale spatial variability of snow density and depth over complex alpine terrain: Implications for estimating snow water equivalent," *Advances in Water Resources*, vol. 55, pp. 40–52, 2013.
- [45] R. O. R. Jenssen, M. Eckerstorfer, S. K. Jacobsen, and R. Storvold, "Drone-Mounted UWB Radar System for Measuring Snowpack Properties: Technical Implementation, Specifications and Initial Results," *International Snow Science Workshop*, no. October, pp. 673–676, 2018.
- [46] G. F. Margrave, "CREWES MatLab toolbox," Calgary, 2020.
- [47] —, "Numerical Methods of Exploration Seismology," Calgary, 2003.
- [48] R. B. Langley, "Rtk Gps," *GPS World*, pp. 70–75, 1998.
- [49] G. R. Cooper and C. D. McGilllem, *Probabilistic Methods of Signal and System Analysis*. The Oxford Series in Electrical and Computer Engineering, 1988.



**Rolf Ole Rydeng Jenssen** received a BSc degree in automation and an MSc degree in applied physics and mathematics from the Arctic University of Norway (UiT) in 2014 and 2016, respectively. His MSc work focused on snow stratigraphy measurements with UWB radar. Since 2017, Jenssen works as a Ph.D. fellow at CIRFA (Centre for Integrated Remote Sensing and Forecasting for Arctic Operations) in Tromsø, Norway, where he focusses on UAV remote sensing for Arctic applications such as monitoring of snow and sea ice conditions.



**Svein Jacobsen** (M'02–SM'07) was born in Lofoten, Norway, in 1958. He received the B.Sc. and M.Sc. degrees from the University of Tromsø, Norway, in 1983 and 1985, respectively, and the Ph.D. degree on microwave sensing of the ocean surface, also from the same university, in 1988. From 1985–1986 he worked as a Researcher with Information Control Ltd. on space-borne observation platforms for the earth-probing satellite ERS-1. From 1989–1992, he was engaged as a Research Scientist for the Norwegian Research Council for Science and Humanities, working on non-linear mapping of the ocean surface by means of synthetic aperture imaging radar (SAR). During 2000–2001, he did a research sabbatical at the University of California, San Francisco, where he investigated the use of multiband microwave radiometry for temperature measurement in the human body. His research interests within thermal medicine included development of active and passive microwave systems and applicators for diagnostic and therapeutic applications in the human body. From 2001 he is a Professor of electrical engineering with the Department of Physics and Technology, UiT – The Arctic University of Norway, Tromsø, Norway. His current research interests include development of miniature UAV mounted UWB radars for various remote sensing applications including snowpack stratigraphy for hardness investigation and weak layer detection.

# / 11

## Discussion and Conclusion

The papers presented in Chapters 8-10 cover topics related to the potential of unmanned aerial vehicle (UAV) mounted radar sensing of snow. Section 11.1 briefly summarizes the conclusions of the three papers and discusses contributions to state of the art technology and methods. Section 11.2 discusses and presents future work and ideas.

### 11.1 Research Conclusions

Recent advances in ultra wide-band (UWB) technology have allowed development of small and lightweight radar systems that are suitable as a UAV payload. Such systems typically go through several design iterations based on experiences made in field trials. Paper I proposes the radar sensing concept, technical implementation and presents the first field results. The initial results show a high correlation with *in situ* snow depth and serve as a proof of concept. Paper I recommends investigating the possibility of estimating other snow parameters such as density. Additionally, development of faster algorithms for radar data acquisition and further improvements on the design of the receiving and transmitting antennas are recommended. Paper I highlights design considerations for the radar sensing task and describes the technical implementation of the prototype as well as the UAV platform itself. At the time of submission of Paper I, ground-penetrating radar systems with the strict weight and compatibility requirements for UAV mounting, while still having the bandwidth to resolve

complex snow stratigraphy and penetration through deep, dense, and wet snow down to the ground, to the best of our knowledge, had not been published in the literature.

Using UAV mounted snow radar to estimate bulk snow volumes with the aid of grid flying is a central application aimed at the hydropower industry and environmental science. Paper II presents improvements made to the ultra-wideband snow sounder (UWiBASS) since Paper I, including post-processing methods to correct for the variable relative altitude of the UAV where a shifting procedure is used to correct for an un-even altitude. Additionally, the radar equation for flat surfaces is directly applied to the sampled data (in terms of power). Paper II further confirms the systems ability to measure snow depth on a large scale with a significantly larger dataset compared to Paper I. Paper II also discusses measurements outside the unambiguous range of the waveform, where the UWiBASS indicates the capability of measuring snow depth up to approximately 30 m above the snow.

In Paper II, we observe that two shorter transects where *in situ* snow depth is taken at approximately ten times higher resolution (high res. 1 and 2) compared to the grid surveys, show significantly higher correlations suggesting that the *in situ* measurements taken in the grid surveys are too sparse to detect snow depth variations on the same scale as the UWiBASS. This is not surprising as the UWiBASS produces approximately 100 times more depth estimates along the same grid.

To improve the comparison between airborne and ground truth measurements and validate the method further, the UWiBASS should be flown in the same transect as a sled mounted ground penetrating radar (GPR). This test was planned to be executed in a field campaign in collaboration with Statkraft<sup>1</sup> and Varicon<sup>2</sup> during the winter of 2020; however, the Covid-19 pandemic caused that campaign to be canceled.

Paper II further validates the UWiBASS as a snow sensing device, and the methods presented expands the state of the art in terms of non-invasive snow surveys.

Estimating snow water equivalent (SWE) non-invasively has several applications for a number of industries and research fields. The missing piece of the puzzle is to estimate snow density reliably and remotely. Paper III proposes an improved scheme for SWE estimation by calculating snow density and depth from the same radar dataset. The method is evaluated through Monte Carlo

1. Visit Statkraft at: <https://www.statkraft.no/>

2. Visit Varicon at: <https://varicon.no/>

simulation, and initial field trial results are presented with a similar statistical spread as in the simulation. Finally, Paper III proposes improvements to the method, most notably improvements to the positioning of the UAV using real-time kinematic (RTK) global positioning system (GPS).

### 11.1.1 Contributions to State of the Art

The field of drone-mounted snow radar has seen considerable development since I started working on this radar system in 2016. Using the latest technology, several startups have been created referencing my work in their applications to various funds (e.g., Innovation Norway), such as the ski radar developer Thinkoutside<sup>3</sup>. In comparison to what is found in the literature (or commercially available) from 2016 up to the present, I would consider the UWIBASS as particularly well-integrated and validated. The work is cited by several groups working on similar challenges where Paper I is acknowledged as the first implementation and test of a drone-mounted snow radar.

To fully develop a product usually takes a team of people, and hence the UWIBASS did not make it out of the prototype stage during this project. However, efforts will be made to apply snow measurements into a commercial service that can be licensed to, e.g., the hydropower industry.

## 11.2 Future Work

Future work includes developing a similar radar system as the UWIBASS to be integrated into a fixed-wing UAV to improve area coverage. This version is especially central to the application of snow measurements over large areas such as snow cover on sea ice or alpine regions. The development includes the design of aerodynamic and lightweight antennas that do not protrude significantly from the bottom of the UAV fuselage. Additionally, the antennas need high directivity and possibly higher output power. On a fixed-wing, the receiving (RX) and transmitting (TX) antennas have the opportunity to be mounted with larger separation (e.g., on the wings), reducing the crosstalk and opening up for higher TX power.

A goal of the UWIBASS is to measure snow depth and ice thickness from the same platform. The concept proposed to accomplish this task is to integrate a second radar system with the UWIBASS that operates in the VHF/UHF frequency range. Hence, this low-frequency radar could detect the ice-water

3. Visit Thinkoutside at: <https://www.thinkoutside.no/>

interface, while the current UWIBASS measures the air-snow and snow-ice interface. One of the major challenges with such a system is, again, in the antenna design, where low weight and high directivity are central design parameters. The initial proposal is to use a software-defined radio (SDR) for signal generation and reception, yielding high flexibility regarding bandwidth and waveform [102]. SDR systems have recently become available in small form factors even down to the size of business cards. Take, for example, the Ettus USRP-b205mini with a frequency cover ranging from 70 MHz to 6 GHz, making it possible to modulate different signals depending on ice conditions. The SDR makes the implemented system re-configurable by the user in the field<sup>4</sup>. It should be noted that the real-time bandwidth of such a sensor is in the order of tens of MHz (in this case 56 MHz). Hence, stepping of the carrier frequency is needed to cover a larger bandwidth, at the expense of measurement rate (IRF/s).

The general idea is to fuse the two highlighted methods shown in Figure 11.1 on an airborne platform.

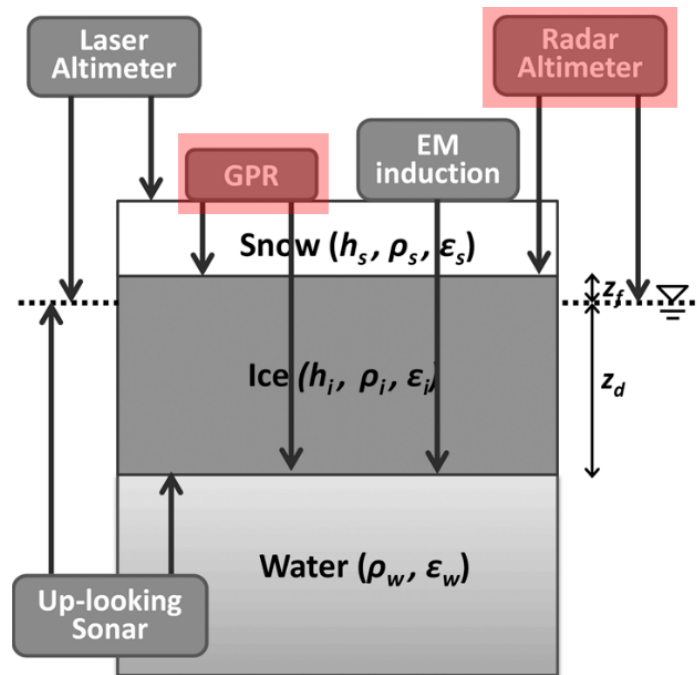


**Figure 11.1:** Schematic diagram illustrating various ice thickness measurement techniques [64].

The antenna development in this project utilized several state-of-the-art meth-

4. For more information about SDR visit: <https://www.ettus.com/>

ods to reduce the physical size of the antennas. However this field still sees great advances with the use of meta-materials [16,43,58,125] and large current radiator (LCR) antennas [26] to reduce size and increase directivity.

As previously discussed, directional antennas are important to reduce the antenna footprint, and Vivaldi antennas have several desirable characteristics, especially with applications where weight and directivity are central parameters. In [81] a 162 MHz to 1.121 GHz Vivaldi antenna is presented. Contrary to convention, this antenna performs well ( $S_{11} < -10$  dB across bandwidth) even though the antenna width and length is on the order of a quarter free-space wavelength at the lowest frequency of operation. However, this design sacrifices directivity to obtain these results.

We are currently working on a method to achieve single antenna operation with the pseudo-noise signal generator. This work involves leakage cancellation using analog delay and phase shifters matched to the total radio frequency (RF) path. This cancellation method could also be realized with analog-to-digital converter (ADC), digital signal processing and digital-to-analog converter (DAC), implemented with field-programmable gate array (FPGA) technology given the speed of current chip solutions is further developed.

Investigations into SDR based radar should result in a highly configurable radar system. A single antenna design will, in most cases, have issues with efficient radiation at the full range of commercial SDR (i.e., approximately 6 GHz). However, designing a system allowing to change antennas in the field quickly could facilitate high-resolution multi-media measurements.

A copy of the UWIBASS is currently at NORCE Grimstad, where it is tested as a detection system for rot in wooden utility poles. Initial tests of this application is shown in Appendix A.3. Further efforts into designing a portable tomographic radar system for this application will be investigated.







# Miscellaneous Experiments

In addition to the experiments and field campaigns described in this thesis, several additional experiments have been conducted during this project where the results have not fulfilled the degree of novelty needed for a publication. Some of these ideas might meet the requirements for novelty, but need a project of their own to collect the needed data. Nevertheless, one could argue the results are interesting. This section briefly presents the results from these experiments.

## A.1 Sea Ice Measurements with UAV Mounted Radar

As ice forms, brine is rejected from the growing ice sheet and accumulates in grooves inside the ice sheet. Thus, as the salt concentration in the brine increases, the freezing point is decreased low enough to stop the freezing of the brine. Over time these brine inclusions erode downwards, creating brine drainage channels. Hence, as the ice ages, the brine concentration (i.e., salinity) drops [113].

During the coordinated arctic acoustic thermometry experiment (CAATEX) field campaign (see Section 6.6), several transects of snow depth and ice thickness were taken in addition to sparse ice cores where salinity, weight, etc. were

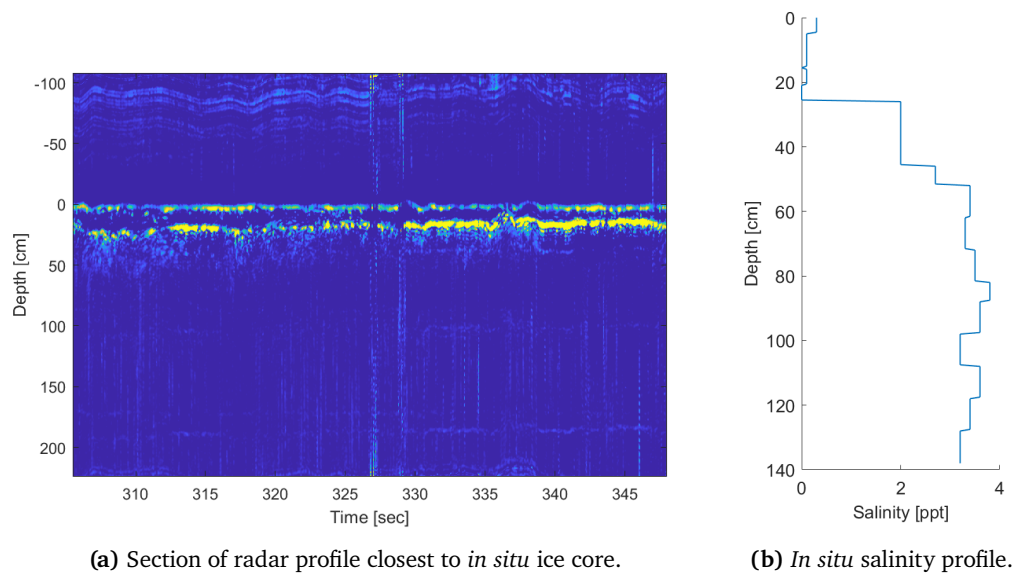
collected.

The ultra-wideband snow sounder (UWiBASS) was flown along the same transects measuring snow thickness while investigating the performance of the radar system on sea ice.

It was found that the UWiBASS was not able to measure the full ice thickness in that current configuration. This is clear from theory [79], and such parameters usually require ground-coupled systems operating at a lower center frequency [38]. Additionally, the snow depth varied between 0 and 10 cm throughout the campaign forming a weak basis for a snow-on-sea-ice dataset.

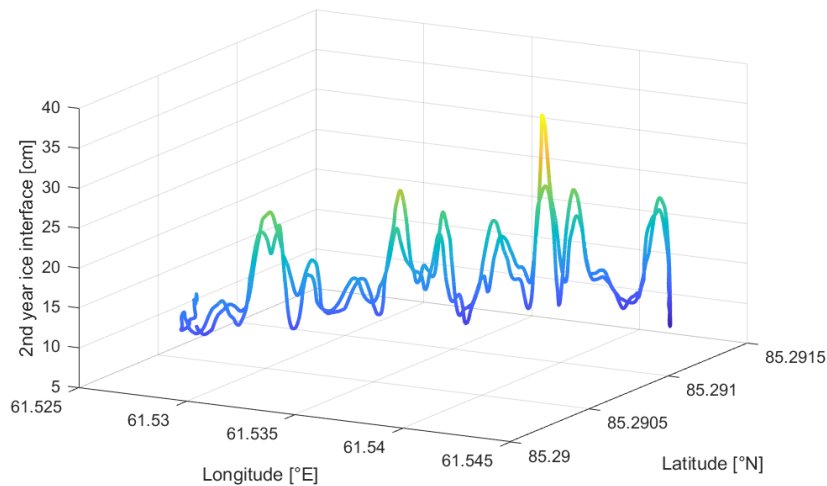
Nonetheless, if the ice was second-year ice (or older), the layer of old (low salinity) ice could be measured with high repeatability and good correlation with *in situ* ice cores.

Figure A.1 shows a profile taken at 88 °N compared to the *in situ* salinity profile, where the detected interface at approximately 20 cm corresponds to the sharp increase in salinity from the ice core. This increase in salinity corresponds to the interface between first-year and multi-year ice.



**Figure A.1:** Example result comparing detection of the second interface in radar image to the spike in salinity at approximately 20 cm.

Figure A.2 show two passes along a 200 m transect where the depth of the same interface as in Figure A.1a is measured, illustrating that the interface is measured with high repeatability.



**Figure A.2:** Example result demonstrating the repeatability of the ice-interface measurements.

## A.2 Freshwater Ice Measurements

Freshwater ice has significantly higher penetration depth than sea ice [39, 79]. This is clear looking at the radar image taken at a freshwater lake in Bardu - Norway. This dataset was collected during a short field campaign (see Section 6.4) aimed at testing the radar system in the field. Figure A.4 shows a transect flying across the lake towards a small peninsula. As we pass over the peninsula, we can see the ice thickness decreasing and the ground (or ice-covered ground) coming into the image. The applications for such measurements are many, including safety assessment of freshwater lakes for people or vehicles, as well as other studies involving freshwater ice. However, a more extensive field campaign with sufficient *in situ* measurements is needed for a publication.

Recent studies confirm that this application is feasible using drone mounted frequency modulated continuous wave (FMCW) radar [88].

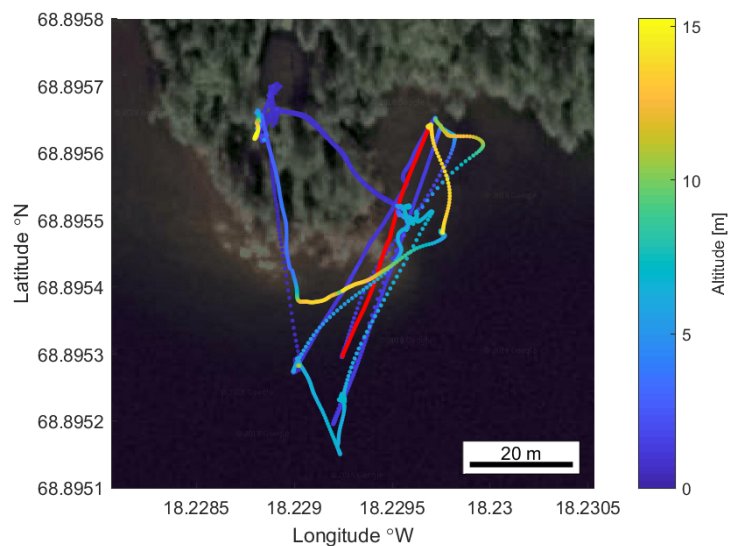


**Figure A.3:** GPS position of the unmanned aerial vehicle (UAV) where colors represent altitude and the transect in question is marked in red.

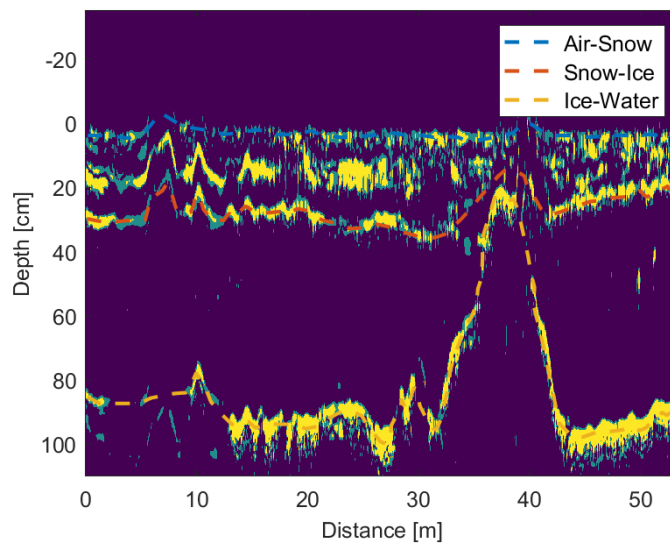


**Figure A.4:** Snow and ice thickness along transect (marked in red in Figure A.3), passing over peninsula at approximately 35 to 42 m.

## A.3 Rot in Wood Detection

Electromagnetic Aquametry is a widespread method involving the measurement of water in solids and liquids using time or frequency-domain methods [57]. In this preliminary study, the backscattered amplitude is evaluated in the time-domain utilizing the increased relative permittivity of wet wood.

This experiment involved looking at the possibility to detect rot in wood with UWB radar due to the need for a non-destructive method to detect rot in utility poles. When the wood starts to rot, the decayed wood is usually wetter than adjacent sound wood [114]. Hence, these experiments focus on detecting differences in moisture in a block of wood.

### A.3.1 Test rig

The test rig consisted of layers of dry wood pieces where the middle layer could be swapped between dry and slightly wet wood. This block of wood was placed on top of a cardboard box to separate it from the floor. Above the wood sample, the radar was mounted on a tripod facing down at the wood sample.



**Figure A.5:** Wood block, where the two darker pieces of wood were switched between wet and dry wood.

### A.3.2 Results

During the test, the interchangeable "core" was swapped between wet and dry and moved to different positions in the wood-block.

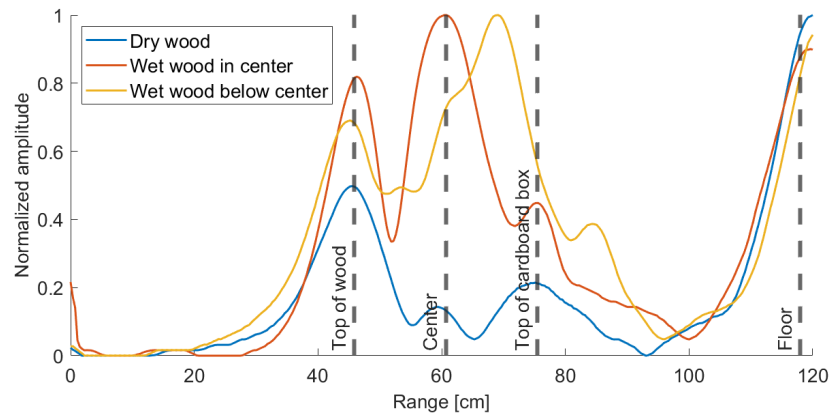


**Figure A.6:** A-scans of dry wood (blue), wood with wet center (red), and wood with wet core below center (yellow).

Figure A.6 clearly shows that the radar can detect and locate high moisture sections of wood. The measurements containing wet wood generally have higher backscatter from the entire wood-block, possibly due to secondary reflections from the wet core. If this work is to be investigated further, I would recommend testing circular tomographic radar imaging methods to locate and image the rot [1]. I would also recommend investigating methods to estimate the permittivity and loss factor from, e.g., resonant methods finding the shift in resonant frequency and quality factor (Q-factor) [90]. From the permittivity and loss factor, material density and moisture content can potentially be calculated [57].

## A.4 Differentiating Ice Types

The Microscale interaction of oil with sea ice for detection and environmental risk management in sustainable operations (MOSIDEO) project in Hamburg (presented in Section 6.1) did not produce the intended results with regards to the UWIBASS. The goal was to detect oil under sea ice; however, the ice in the basin was very wet, and the radar waves could not penetrate the wet ice.

Nevertheless, some interesting results did come from this experiment. The radar detected differences in backscattered energy from two different ice types, namely columnar and granular ice. The HSVA basin had both ice types

separated by a wall in the center of the basin. Figure A.7 shows the difference in backscattered energy from the two halves of the basin. This result agrees well with ice scattering theory, where granular ice is expected to return higher backscatter than columnar ice due to higher surface roughness [79]. This effect should also be valid for the nadir-pointing radar as the antennas used during the experiment had  $70^\circ$  half power beam width (HPBW) resulting in high backscatter in the sidelobes for granular ice.

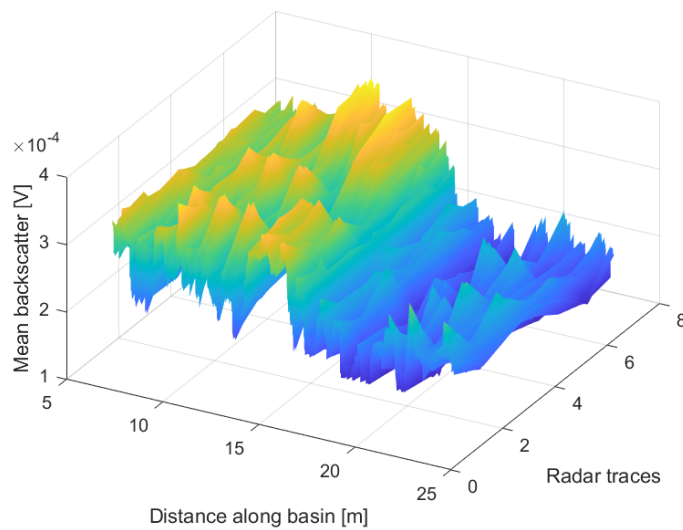


**Figure A.7:** Surface plot of mean backscattered energy across the HSV A basin, where the two ice types can be identified; granular to the left and columnar to the right.





# Bibliography

- [1] A. M. Alani and F. Tosti. GPR applications in structural detailing of a major tunnel using different frequency antenna systems. *Construction and Building Materials*, 158:1111–1122, 2018.
- [2] A. J. Albrecht and J. E. Gaffney. Software Function, Source Lines of Code, and Development Effort Prediction: A Software Science Validation. *IEEE Transactions on Software Engineering*, SE-9(6):639–648, 1983.
- [3] E. Arnold, F. Rodriguez-Morales, J. Paden, C. Leuschen, S. Keshmiri, S. Yan, M. Ewing, R. Hale, A. Mahmood, A. Blevins, A. Mishra, T. Karidi, B. Miller, and J. Sonntag. HF/VHF radar sounding of ice from manned and unmanned airborne platforms. *Geosciences (Switzerland)*, 8(5):1–22, 2018.
- [4] A. S. Avdushin, A. V. Ashikhmin, V. V. Negrobov, Y. G. Pasternak, and S. M. Fedorov. Vivaldi antenna with printed lens in aperture. *Microwave and Optical Technology Letters*, 56(2):369–371, 2 2014.
- [5] S. Birkenfeld. Automatic detection of reflexion hyperbolas in GPR data with neural networks. *2010 World Automation Congress, WAC 2010*, 2010.
- [6] J. H. Bradford, D. F. Dickins, and P. J. Brandvik. Assessing the potential to detect oil spills in and under snow using airborne ground-penetrating radar. *Geophysics*, 75(2), 2010.
- [7] R. D. Brown and P. W. Mote. The response of Northern Hemisphere snow cover to a changing climate. *Journal of Climate*, 22(8):2124–2145, 2009.
- [8] O. Bruland, Å. Færevåg, I. Steinsland, G. E. Liston, and K. Sand. Weather SDM: Estimating Snow density with high precision using Snow depth and local climate. *Hydrology Research*, 46(4):494–506, 2015.
- [9] R. Burr, M. Schartel, W. Mayer, T. Walter, and C. Waldschmidt. Uav-Based

- Polarimetric Synthetic Aperture Radar for Mine Detection. *IGARSS 2019 - 2019 IEEE International Geoscience and Remote Sensing Symposium*, pages 9208–9211, 2019.
- [10] M. R. P. Cerquera, J. D. Colorado Montaña, I. Mondragón, J. D. C. Montaña, and I. Mondragón. UAV for Landmine Detection Using SDR-Based GPR Technology. In *Robots Operating in Hazardous Environments*, page 13. Intech Open, Bogotá, 2016.
- [11] M. Chandra and T. J. Tanzi. Conception GPR pour drone : propagation. *Comptes Rendus Physique*, 19(1-2):72–84, 2018.
- [12] J. S. Clair and W. Steven Holbrook. Measuring snow water equivalent from common-offset GPR records through migration velocity analysis. *Cryosphere*, 11(6):2997–3009, 2017.
- [13] L. Crocco and V. Ferrara. A review on ground penetrating radar technology for the detection of buried or trapped victims. *2014 International Conference on Collaboration Technologies and Systems, CTS 2014*, pages 535–540, 2014.
- [14] D. Daniels. *Ground Penetrating Radar (2nd Edition)*. Institution of Engineering and Technology, 2013.
- [15] C. H. Dix. Seismic velocities from surface measurements. *Geophysics*, 20(1):68–86, 1955.
- [16] Y. Dong and T. Itoh. Metamaterial-Based Antennas. *Proceedings of the IEEE*, 100(7):2271–2285, 2012.
- [17] Q. Dou, L. Wei, D. R. Magee, and A. G. Cohn. Real-Time Hyperbola Recognition and Fitting in GPR Data. *IEEE Transactions on Geoscience and Remote Sensing*, 55(1):51–62, 2017.
- [18] M. R. Drinkwater. LIMEX '87 ice surface characteristics: Implications for C-band SAR backscatter signatures. *IEEE Transactions on Geoscience and Remote Sensing*, 27(5):501–513, 1989.
- [19] M. Durand, G. Charles, E. Kim, N. Molotch, P. Thomas H., R. Mark, S. Melody, and V. Carrie. *NASA SnowEx Science Plan: Assessing Approaches for Measuring Water in Earth's Seasonal Snow*. National Aeronautics and Space Administration, 1.6 edition, 2017.
- [20] K. Eder, C. Reidler, C. Mayer, and M. Leopold. Crevasse detection in alpine

- areas using ground penetrating radar as a component for a mountain guide system. *The International Archives of the Photogrammetry, Remote Sensing and Spatial Information Sciences*, 37:837–842, 2008.
- [21] H. Eicken, H. Fischer, and P. Lemke. Effects of the snow cover on Antarctic sea ice and potential modulation of its response to climate change. *Annals of Glaciology*, 21:369–376, 1995.
- [22] D. Ellerbrugh and H. Boyne. Snow Stratigraphy and Water Equivalence. *Journal of Glaciology*, 26(94):225–233, 1980.
- [23] M. A. Elmansouri and D. S. Filipovic. Low-dispersion spiral antennas. *IEEE Transactions on Antennas and Propagation*, 60(12):5522–5530, 2012.
- [24] C. Fierz, R. Armstrong, Y. Durand, P. Etchevers, E. Greene, M. McClung, D. K. Nishimura, P. Satyawali, and S. Sokratov. *The International Classification for Seasonal Snow on the Ground*. IACS, UNESCO, Paris, 2009.
- [25] J. F. Fitter, A. B. McCallum, and J. P. Leon. Development of an Unmanned Aircraft Mounted Software Defined Ground Penetrating Radar. *Geotechnical and Geophysical Site Characterisation*, 5:957–962, 2016.
- [26] P. Galajda, M. Pecovsky, M. Sokol, M. Kmec, and D. Kocur. Recent advances in ASIC development for enhanced performance m-sequence UWB systems. *Sensors (Switzerland)*, 20(17):1–23, 2020.
- [27] S. Gogineni, J. B. Yan, D. Gomez, F. Rodriguez-Morales, J. Paden, and C. Leuschen. Ultra-wideband radars for remote sensing of snow and ice. *2013 IEEE MTT-S International Microwave and RF Conference, IMaRC 2013*, pages 1–4, 2013.
- [28] J. T. González-Partida, P. Almorox-González, M. Burgos-García, and B. P. Dorta-Naranjo. SAR system for UAV operation with motion error compensation beyond the resolution cell. *Sensors*, 8(5):3384–3405, 2008.
- [29] D. Goodman and S. Piro. *GPR Remote Sensing in Archaeology*. Springer, New York, 2013.
- [30] H. Gubler and M. Hiller. The use of microwave FMCW radar in snow and avalanche research. *Cold Regions Science and Technology*, 9(2):109–119, 1984.
- [31] D. Gustafsson, N. Sundström, and A. Lundberg. Estimation of Snow Water Equivalent of Dry Snowpacks Using a Multi-Offset Ground Pen-

- etrating Radar System. In *69th Eastern Snow Conference, Frost Valley*, pages 197–206, Claryville, New York, 2012.
- [32] Z. Hajnal and I. T. Sereda. Maximum uncertainty of interval velocity estimates. *Geophysics*, 46(11):1543–1547, 1981.
- [33] M. T. Hallikainen, F. T. Ulaby, and M. Abdelrazik. Dielectric properties of snow in the 3 to 37 GHz range. *IEEE Transactions on Antennas and Propagation*, AP-34(11):1329–1340, 1986.
- [34] J. Hasted. Liquid water: Dielectric properties. In *The Physics and Physical Chemistry of Water*, pages 255–309. Springer, 1972.
- [35] R. Herrmann. *M-sequence based ultra-wideband radar and its application to crack detection in salt mines*. PhD thesis, Ilmenau University of Technology, 2011.
- [36] W. S. Holbrook, S. N. Miller, and M. A. Provar. Estimating snow water equivalent over long mountain transects using snowmobile-mounted ground-penetrating radar. *Geophysics*, 81(1):WA183–WA193, 2016.
- [37] J. Holmgren, M. Sturm, N. E. Yankielun, and G. Koh. Extensive measurements of snow depth using FM-CW radar. *Cold Regions Science and Technology*, 27(1):17–30, 1998.
- [38] B. Holt, P. Kanagaratnam, S. P. Gogineni, V. C. Ramasami, A. Mahoney, and V. Lytle. Sea ice thickness measurements by ultrawideband penetrating radar: First results. *Cold Regions Science and Technology*, 55(1):33–46, 2009.
- [39] G. A. Hufford. A model for the complex permittivity of ice at frequencies below 1 THz. *International Journal of Infrared and Millimeter Waves*, 12(7):677–682, 1991.
- [40] W. Huining, J. T. Pulliainen, and M. T. Hallikainen. Effective permittivity of dry snow in the 18 to 90 GHz range. *Journal of Electromagnetic Waves and Applications*, 13(10):1393–1394, 1999.
- [41] IEEE Standards Association. *IEEE Standard Definitions of Terms for Antennas*, volume 2013. IEEE, 2014.
- [42] IPCC. Climate Change 2014. *Climate Change 2014: Synthesis Report*, 1(October):1–169, 2014.

- [43] M. T. Islam, M. T. Islam, M. Samsuzzaman, H. Arshad, and H. Rmili. Metamaterial Loaded Nine High Gain Vivaldi Antennas Array for Microwave Breast Imaging Application. *IEEE Access*, 8:227678–227689, 2020.
- [44] S. Jazayeri, A. Saghafi, S. Esmaeili, and C. P. Tsokos. Automatic object detection using dynamic time warping on ground penetrating radar signals. *Expert Systems with Applications*, 122:102–107, 2019.
- [45] R. O. R. Jenssen. *Snow Stratigraphy Measurements With UWB Radar*. Department of Physics and Technology, UiT Norges Arktiske Universitet, MSc thesis, 2016.
- [46] R. O. R. Jenssen, M. Eckerstorfer, and S. Jacobsen. Drone-Mounted Ultra-wideband Radar for Retrieval of Snowpack Properties. *IEEE Transactions on Instrumentation and Measurement*, 69(1):221–230, 2020.
- [47] R. O. R. Jenssen and S. Jacobsen. Drone-mounted UWB snow radar: technical improvements and field results. *Journal of Electromagnetic Waves and Applications*, 34(14):1930–1954, 2020.
- [48] R. C. Johnson. *Antenna engineering handbook*. McGraw-Hill Professional, 1993.
- [49] H. M. Jol. *Ground Penetrating Radar: Theory and Applications*. Elsevier, 2008.
- [50] P. Kanagaratnam, T. Markus, V. Lytie, B. Heavey, P. Jansen, G. Prescott, and S. P. Gogineni. Ultrawideband radar measurements of thickness of snow over sea ice. *IEEE Transactions on Geoscience and Remote Sensing*, 45(9):2715–2724, 2007.
- [51] T. R. Karl, P. Y. Groisman, R. W. Knight, R. Richard, T. R. Karl, P. Y. Groisman, and R. W. Knight. Recent Variations of Snow Cover and Snowfall in North America and Their Relation to Precipitation and Temperature Variations. *Journal of Climate*, 6(7):1327–1344, 1993.
- [52] T. Kawamura, K. I. Ohshima, T. Takizawa, and S. Ushio. Physical, structural, and isotopic characteristics and growth processes of fast sea ice in Lützow-Holm Bay, Antarctica. *Journal of Geophysical Research: Oceans*, 102(96):3345–3355, 1997.
- [53] B. E. Keevil and R. Ramseier. Behavior of oil spilled under floating ice. In *Conference on prevention and control of oil pollution*, pages 497–501. American Petroleum Institute, 1975.

- [54] S.-W. Kim and D.-Y. Choi. Implementation of rectangular slit-inserted ultra-wideband tapered slot antenna. *SpringerPlus*, 5(1):1387, 8 2016.
- [55] Y. Kim, T. J. Reck, M. Alonso-Delpino, T. H. Painter, H. P. Marshall, E. H. Bair, J. Dozier, G. Chattopadhyay, K. N. Liou, M. C. F. Chang, and A. Tang. A Ku -Band CMOS FMCW Radar Transceiver for Snowpack Remote Sensing. *IEEE Transactions on Microwave Theory and Techniques*, 66(5):2480–2494, 2018.
- [56] O. B. Knut Sand, K. Sand, and O. Bruland. Application of Georadar for snow cover surveying. *Nordic Hydrology*, 29(4-5):361–370, 1998.
- [57] K. Kupfer. *Electromagnetic Aquametry*. Springer, 2005.
- [58] N. Kurniawati, D. Novita Nurmala Putri, and Y. Kurnia Ningsih. Random Forest Regression for Predicting Metamaterial Antenna Parameters. In *2nd International Conference on Industrial Electrical and Electronics (ICIEE)*, pages 174–178, 2020.
- [59] R. Kwok, B. Panzer, C. Leuschen, S. Pang, T. Markus, B. Holt, and S. Gogineni. Airborne surveys of snow depth over Arctic sea ice. *Journal of Geophysical Research: Oceans*, 116(11):1–16, 2011.
- [60] V. Kyovtorov, I. Georgiev, S. Margenov, D. Stoychev, F. Oliveri, and D. Tarchi. New antenna design approach – 3D polymer printing and metallization. experimental test at 14–18 GHz. *AEU - International Journal of Electronics and Communications*, 73:119–128, 2017.
- [61] C. J. Li and H. Ling. Synthetic Aperture Radar Imaging Using a Small Consumer Drone. *IEEE International Symposium on Antennas and Propagation, Vancouver, Canada*, 10(d):4–5, 2015.
- [62] C. J. Li and H. Ling. High-resolution, downward-looking radar imaging using a small consumer drone. In *2016 IEEE International Symposium on Antennas and Propagation (APSURSI)*, volume 2, pages 2037–2038, 2016.
- [63] G. E. Liston and C. A. Hiemstra. A simple data assimilation system for complex snow distributions (SnowAssim). *Journal of Hydrometeorology*, 9(5):989–1004, 2008.
- [64] H. Liu, K. Takahashi, and M. Sato. Measurement of dielectric permittivity and thickness of snow and ice on a brackish lagoon using GPR. *IEEE Journal of Selected Topics in Applied Earth Observations and Remote Sensing*, 7(3):820–827, 2014.

- [65] M. Lort, A. Aguiasca, C. López-Martínez, and T. M. Marín. Initial evaluation of SAR capabilities in UAV multicopter platforms. *IEEE Journal of Selected Topics in Applied Earth Observations and Remote Sensing*, 11(1):127–140, 2018.
- [66] A. Lundberg, N. Granlund, and D. Gustafsson. Towards automated 'ground truth' snow measurements—a review of operational and new measurement methods for Sweden, Norway, and Finland. *Hydrological Processes*, 24(14):1955–1970, 2010.
- [67] A. Lundberg, C. Richardson-Näslund, and C. Andersson. Snow density variations: Consequences for ground-penetrating radar. *Hydrological Processes*, 20(7):1483–1495, 2006.
- [68] A. Lundberg and H. Thunehed. Snow wetness influence on impulse radar snow surveys theoretical and laboratory study. *Nordic Hydrology*, 31(2):89–106, 2000.
- [69] B. Majumdar, S. Chakraborty, D. Baer, K. P. Esselle, and M. Heimlich. Additive Manufacturing of a Dual-Ridged Horn Antenna. *Progress In Electromagnetics Research Letters*, 59(March):109–114, 2016.
- [70] H. P. Marshall and G. Koh. FMCW radars for snow research. *Cold Regions Science and Technology*, 52(2):118–131, 2008.
- [71] H. P. Marshall, M. Schneebeli, and G. Koh. Snow stratigraphy measurements with high-frequency FMCW radar: Comparison with snow micro-penetrator. *Cold Regions Science and Technology*, 47(1-2 SPEC. ISS.):108–117, 2007.
- [72] C. Mätzler. Relation between grain size and correlation length of snow. *American Geophysical Union Fall Meeting*, 48:1–4, 2002.
- [73] C. Matzler and U. Wegmüller. Dielectric properties of freshwater ice at microwave frequencies. *Journal of Physics D: Applied Physics*, 20(12):1623–1630, 1987.
- [74] G. A. Maykut and N. Untersteiner. Some results from a time-dependent thermodynamic model of sea ice. *Journal of Geophysical Research*, 76(6):1550–1575, 1971.
- [75] L. Mertens, R. Persico, L. Matera, and S. Lambot. Automated Detection of Reflection Hyperbolas in Complex GPR Images with No A Priori Knowledge on the Medium. *IEEE Transactions on Geoscience and Remote*

*Sensing*, 54(1):580–596, 2016.

- [76] V. Midtbøen, K. G. Kjelgard, and T. S. Lande. 3D printed horn antenna with PCB microstrip feed for UWB radar applications. In *IEEE MTT-S International Microwave Workshop Series on Advanced Materials and Processes for RF and THz Applications (IMWS-AMP)*, volume September, Pavia, Italy, 2017.
- [77] J. C. Moore, P. Maijala, S. E. Hjelt, A. Pälli, A. Sinisalo, H. Salminen, J. Saarikko, and E. Virtanen. GPR investigations of glaciers and sea ice in the scandinavian arctic. *Proceedings of an international symposium on advanced technology in environmental and natural resources*, pages 1–9, 1998.
- [78] A. W. Nolin. Recent advances in remote sensing of seasonal snow. *Journal of Glaciology*, 56(200):1141–1150, 2010.
- [79] R. G. Onstott and R. A. Shuchman. SAR Measurements of Sea Ice. In *SAR Marine User's Manual*, pages 81–115. General Dynamics, 2004.
- [80] M. J. Øyan, S. E. Hamran, L. Hanssen, T. Berger, and D. Plettemeier. Ultrawideband gated step frequency ground-penetrating radar. *IEEE Transactions on Geoscience and Remote Sensing*, 50(1):212–220, 2012.
- [81] B. Panzer. *Development of an Electrically Small Vivaldi Antenna: The CReSIS Aerial Vivaldi (CAV-A)*. PhD thesis, University of Kansas, 2004.
- [82] B. Panzer, D. Gomez-Garcia, C. Leuschen, J. Paden, F. Rodriguez-Morales, A. Patel, T. Markus, B. Holt, and P. Gogineni. An ultra-wideband, microwave radar for measuring snow thickness on sea ice and mapping near-surface internal layers in polar firn. *Journal of Glaciology*, 59(214):244–254, 2013.
- [83] C. Petrich, M. O'sadnick, C. Brekke, M. Myrnes, S. Maus, M. L. Salomon, S. Woelk, T. Grydeland, R. O. Jenssen, H. Eicken, M. Oggier, L. Ferro-Famil, L. Harkati, O. Rebane, and N. Reimer. MOSIDEO/CIRFA tank experiments on behavior and detection of oil in ice. In *Proceedings of the International Conference on Port and Ocean Engineering under Arctic Conditions, POAC*, volume 2019-June, Delft, The Netherlands, 2019.
- [84] A. A. Pfaffhuber, J. L. Lieser, and C. Haas. Snow thickness profiling on Antarctic sea ice with GPR—Rapid and accurate measurements with the potential to upscale needles to a haystack. *Geophysical Research Letters*, 44(15):7836–7844, 2017.



- [85] C. Pielmeier and M. Schneebeili. Developments in the stratigraphy of snow. *Surveys in Geophysics*, 24(5-6):389–416, 2003.
- [86] M. Pieraccini, G. Luzi, and C. Atzeni. Terrain mapping by ground-based interferometric radar. *IEEE Transactions on Geoscience and Remote Sensing*, 39(10):2176–2181, 2001.
- [87] R. Pirazzini, L. Leppänen, G. Picard, J. I. Lopez-Moreno, C. Marty, G. Macelloni, A. Kontu, A. von Lerber, C. M. Tanis, M. Schneebeili, P. de Rosnay, and A. N. Arslan. European in-situ snow measurements: Practices and purposes. *Sensors (Switzerland)*, 18(7), 2018.
- [88] P. Pomerleau, A. Royer, A. Langlois, P. Cliche, B. Courtemanche, J. B. Madore, G. Picard, and E. Lefebvre. Low cost and compact FMCW 24 GHz radar applications for snowpack and ice thickness measurements. *Sensors (Switzerland)*, 20(14):1–29, 2020.
- [89] D. Pozar. *Microwave Engineering*. Wiley, 2012.
- [90] J. Reistad. *A compact portable resonance probe system for in situ measurements of snow conditions*. UiT Norges Arktiske Universitet, Department of Physics and Technology, MSc thesis, 2018.
- [91] M. A. Richards. *Fundamentals of Radar Signal Processing*. McGraw-Hill Professional, 2015.
- [92] F. Rodriguez-Morales, S. Gogineni, C. J. Leuschen, J. D. Paden, J. Li, C. C. Lewis, B. Panzer, D. Gomez-Garcia Alvestegui, A. Patel, K. Byers, R. Crowe, K. Player, R. D. Hale, E. J. Arnold, L. Smith, C. M. Gifford, D. Braaten, and C. Panton. Advanced multifrequency radar instrumentation for polar Research. *IEEE Transactions on Geoscience and Remote Sensing*, 52(5):2824–2842, 2014.
- [93] Y. Rodriguez-Vaqueiro, J. Vazquez-Cabo, B. Gonzalez-Valdes, A. Pino, Y. Alvarez, M. Garcia-Fernandez, F. Las-Heras, and A. Arboleya. Array of antennas for a GPR system onboard a UAV. *2019 IEEE International Symposium on Antennas and Propagation and USNC-URSI Radio Science Meeting, APSURSI 2019 - Proceedings*, pages 821–822, 2019.
- [94] M. Rückamp and N. Blindow. King George Island ice cap geometry updated with airborne GPR measurements. *Earth System Science Data*, 4(1):23–30, 2012.
- [95] A. Rutishauser, H. Maurer, and A. Bauder. Helicopter-borne ground-

- penetrating radar investigations on temperate alpine glaciers: A comparison of different systems and their abilities for bedrock mapping. *Geophysics*, 81(1):WA119–WA129, 2016.
- [96] N. Rutter, H.-P. Marshall, K. Tape, R. Essery, and J. King. Impact of spatial averaging on radar reflectivity at internal snowpack layer boundaries. *Journal of Glaciology*, pages 1–10, 2016.
- [97] J. Sachs, R. Herrmann, M. Kmec, M. Helbig, and K. Schilling. Recent Advances and Applications of M-Sequence based Ultra-Wideband Sensors. *2007 IEEE International Conference on Ultra-Wideband*, 2007.
- [98] F. Sagnard and J. P. Tarel. Template-matching based detection of hyperbolas in ground-penetrating radargrams for buried utilities. *Journal of Geophysics and Engineering*, 13(4):491–504, 2016.
- [99] U. Schwarz, F. Thiel, F. Seifert, R. Stephan, and M. Hein. Ultra-wideband antennas for combined magnetic resonance imaging and UWB radar applications. In *IEEE MTT-S International Microwave Symposium Digest*, pages 1433–1436, 2009.
- [100] K. K. Singh, P. Datt, V. Sharma, A. Ganju, V. D. Mishra, A. Parashar, and R. Chauhan. Snow depth and snow layer interface estimation using Ground Penetrating Radar. *Current Science*, 100(10):1532–1539, 2011.
- [101] D. Šipoš, P. Peter, and D. Gleich. On drone ground penetrating radar for landmine detection. *2017 First International Conference on Landmine: Detection, Clearance and Legislations (LDCL)*, pages 7–10, 2017.
- [102] S. Sundaresan, C. Anjana, T. Zacharia, and R. Gandhiraj. Real time implementation of FMCW radar for target detection using GNU radio and USRP. *2015 International Conference on Communication and Signal Processing, ICCSP 2015*, pages 1530–1534, 2015.
- [103] K. Takahashi, J. Igel, H. Preetz, and S. Kuro. Basics and Application of Ground-Penetrating Radar as a Tool for Monitoring Irrigation Process. *Problems, Perspectives and Challenges of Agricultural Water Management*, 2012.
- [104] A. Tan, K. Eccleston, I. Platt, I. Woodhead, W. Rack, and J. McCulloch. The Design of a UAV Mounted Snow Depth Radar Results of Measurements on Antarctic Sea Ice. *2017 IEEE Conference on Antenna Measurements & Applications (Cama)*, pages 316–319, 2017.

- [105] A. E.-C. Tan, J. McCulloch, W. Rack, I. Platt, and I. Woodhead. Radar Measurements of Snow Depth Over Sea Ice on an Unmanned Aerial Vehicle. *IEEE Transactions on Geoscience and Remote Sensing*, pages 1–8, 2020.
- [106] D. Tarchi, G. Guglieri, M. Vespe, C. Gioia, F. Sermi, and V. Kyovtorov. Mini-radar system for flying platforms. *4th IEEE International Workshop on Metrology for AeroSpace, MetroAeroSpace 2017 - Proceedings*, pages 40–44, 2017.
- [107] J. D. Taylor. *Ultrawideband Radar Applications and Design*. CRC Press, 2012.
- [108] M. Tiuri, A. Sihvola, E. Nyfors, and M. Hallikaiken. The complex dielectric constant of snow at microwave frequencies. *IEEE Journal of Oceanic Engineering*, 9(5):377–382, 1984.
- [109] L. Tsang and J. A. Kong. Scattering of electromagnetic waves from random media with multiple scattering included. *Journal of Mathematical Physics*, 23(6):1213–1222, 1982.
- [110] F. T. Ulaby, M. Abdelrazik, and W. H. Stiles. Snowcover Influence on Backscattering from Terrain. *IEEE Transactions on Geoscience and Remote Sensing*, GE-22(2):126–133, 1984.
- [111] F. T. Ulaby, R. K. Moore, and A. K. Fung. *Microwave Remote Sensing Active and Passive-Volume II: Radar Remote Sensing and Surface Scattering and Emission Theory*. Addison-Wesley Publishing Company, 1982.
- [112] F. T. Ulaby, W. H. Stiles, L. F. Dellwig, and B. C. Hanson. Experiments on the Radar Backscatter of Snow. *IEEE Transactions on Geoscience Electronics*, 15(4):185–189, 1977.
- [113] P. Wadhams. How does Arctic sea ice form and decay?, 2003.
- [114] H. Watson. *Wood pole maintenance*, volume 4-6. Bureau of Reclamation, Denver, CO, 1992.
- [115] R. W. Webb. Using ground penetrating radar to assess the variability of snow water equivalent and melt in a mixed canopy forest, Northern Colorado. *Frontiers of Earth Science*, 11(3):482–495, 2017.
- [116] X. Wei. *Gpr Data Processing for Reinforced Concrete Bridge Decks*. PhD thesis, Georgia Institute of Technology, 2014.

- [117] X. Wei and Y. Zhang. Autofocusing techniques for GPR data from RC bridge decks. *IEEE Journal of Selected Topics in Applied Earth Observations and Remote Sensing*, 7(12):4860–4868, 2014.
- [118] P. F. Worcester and M. S. Ballard. Ocean acoustics in the changing Arctic. *Physics Today*, 73(12):44–49, 2020.
- [119] K. Wu, G. A. Rodriguez, M. Zajc, E. Jacquemin, M. Clément, A. De Coster, and S. Lambot. A new drone-borne GPR for soil moisture mapping. *Remote Sensing of Environment*, 235(November):111456, 2019.
- [120] J. B. Yan, D. Gomez-Garcia Alvestegui, J. W. McDaniel, Y. Li, S. Gogineni, F. Rodriguez-Morales, J. Brozena, and C. J. Leuschen. Ultrawideband FMCW radar for airborne measurements of snow over sea ice and land. *IEEE Transactions on Geoscience and Remote Sensing*, 55(2):834–843, 2017.
- [121] N. Yankielun, W. Rosenthal, and R. E. Davis. Alpine snow depth measurements from aerial FMCW radar. *Cold Regions Science and Technology*, 40(1-2):123–134, 2004.
- [122] M. A. Yarleque, S. Alvarez, and H. J. Martinez. FMCW GPR radar mounted in a mini-UAV for archaeological applications: First analytical and measurement results. In *2017 International Conference on Electromagnetics in Advanced Applications (ICEAA)*, pages 1646–1648. IEEE, 9 2017.
- [123] T. M. Zaboronkova, N. A. Dugin, and E. N. Myasnikov. Microwave horn antenna made of a graphene-containing carbon composite material. *2015 9th European Conference on Antennas and Propagation, EuCAP 2015*, pages 8–9, 2015.
- [124] J. Zhao, B. Cheng, T. Vihma, Q. Yang, F. Hui, B. Zhao, G. Hao, H. Shen, and L. Zhang. Observation and thermodynamic modeling of the influence of snow cover on landfast sea ice thickness in Prydz Bay, East Antarctica. *Cold Regions Science and Technology*, 168(December 2018):102869, 2019.
- [125] B. Zhou and T. J. Cui. Directivity Enhancement to Vivaldi Antennas Using Compactly Anisotropic Zero-Index Metamaterials. *IEEE Antennas and Wireless Propagation Letters*, 10:326–329, 2011.
- [126] X. Zhou, H. Chen, and J. Li. An Automatic GPR B-Scan Image Interpreting Model. *IEEE Transactions on Geoscience and Remote Sensing*, 56(6):3398–3412, 2018.



